ÉRTEKEZÉS

a

DOKTORI (Ph. D)

fokozat megszerzéséhez

KÉMIÁBÓL

DRAVECZ GABRIELLA

Fázisegyensúlyok vizsgálata az X_2O-Li_2O-Nb_2O_5 (X = Na, Rb, Cs) hármas rendszerekben, $LiNbO_3$ egykristály növesztése és vizsgálata

TÉMAVEZETŐ:

Lassányiné dr. Polgár Katalin (Magyar Tudományos Akadémia, Szilárdtestfizikai és Optikai Kutatóintézet)

Prof. Michel Ferriol (Paul Verlaine Egyetem, Metz)

Prof. Orbán Miklós (Eötvös Loránd Tudományegyetem)

EÖTVÖS LORÁND
TUDOMÁNYEGYETEM
TERMÉSZETTUDOMÁNYI KAR
PROGRAM: Analitikai, kolloid-és
környezetkémia, elektrokémia
PROGRAMVEZETŐ: Dr. Záray Gyula,
D. Sc, egyetemi tanár

PAUL VERLAINE UNIVERSITY OF
METZ

KÉMIAI TANSZÉK, Saint-Avold

Budapest, 2008

DISSERTATION
for the obtention of the degree of
DOCTOR OF PHYLOSOPHY
in
CHEMISTRY
by
GABRIELLA DRAVECZ

Study of the phase equilibria in the ternary systems X_2O-Li_2O-Nb_2O_5 (X = Na, Rb, Cs), single crystal growth and characterization of $LiNbO_3$

SUPERVISORS:
Lassányiné dr. Polgár Katalin (Research Institute for Solid State Physics and Optics)
Prof. Michel Ferriol (Paul Verlaine University of Metz)
Prof. Orbán Miklós (University of Eötvös Lóránd)

EÖTVÖS LÓRÁND UNIVERSITY
FACULTY OF SCIENCE
(Budapest, Hungary)
PROGRAM: Analitical Chemistry, Colloid- and Environmental Chemistry, Electrochemistry
PROGRAM LEADER: Prof. Gyula Záray

PAUL VERLAINE UNIVERSITY OF METZ

DEPARTMENT: Chemistry, Saint-Avold

Budapest, 2008

Foreword

The present work is the result of a tri-lateral research among the Eötvös Lóránd University, the Research Institute for Solid State Physics and Optics of the Hungarian Academy of Sciences, both in Budapest, and the University Paul Verlaine (Metz, France). There has been a more than 10 year's cooperation between the Optical, Photonic Materials and Systems laboratory of the University of Metz and the Crystal Technology Department of the Research Institute for Solid State Physics and Optics of the Hungarian Academy of Sciences (former Research Laboratory for Crystal Physics).

This cooperation has not only been restricted to joint research work and the exchange of samples and researchers, publication of common papers (20), but also included the exchange of PhD students and the bilateral supervision.

I've joined the group in September 2004 as a shared Ph.D student of the University Eötvös Lóránd and the University of Metz. With an Eiffel Doctorat "co-tutelle" scholarship I've spent 15 months in Saint Avold (France) and another 15 months in Budapest.

Based on the results of the previous investigations concerning the phase relations of the K_2O - Li_2O - Nb_2O_5 ternary system near the existence region of lithium niobate the common research was extended to the investigation of the potential use of other alkali oxides (instead of K_2O), namely Na_2O, Rb_2O and Cs_2O as solvent components in the growth of stoichiometric lithium niobate. The methods I've got acquainted with and the results we obtained in this period are summarized in my thesis.

Contents

Background and objectives

Lithium (meta-) niobate ($LiNbO_3$, LN) does not occur in nature, the first report on its preparation and ferroelectric properties was given by Matthias and Remeika in 1949 [1]. The versatility of $LiNbO_3$ arises from the unique combination of piezoelectric, pyroelectric, electro-optical and nonlinear optical properties enabling it to be used in a wide range of applications. Most basic experiments on acoustic wave propagation, electro-optic light modulation, optical second harmonic generation, and parametric oscillation were performed between 1965 and 1967. Lithium niobate was also the first material found to exhibit photorefractivity — an effect where the trapping of photogenerated charge carriers induces reversible changes in the refractive indices — which can be used for holographic image processing and information storage. Lithium niobate can be used in surface acoustic wave filters, optical frequency converters and optical parametric amplifiers based on single domain bulk crystals, periodical structures or waveguides.

Single crystals of good quality and uniform composition can be grown from the congruent melt that corresponds to the $[Li] / [Nb] \approx 0.945$ ratio. For this composition the liquid and the solid phases in equilibrium have the same concentration of each component. Consequently, using this starting composition in crystal growth, the segregation coefficients for both Li_2O and Nb_2O_5 are equal to 1. Congruent lithium niobate (cLN) crystals can be grown easily and this is the composition used in most applications [2, 3, 4]. The drawback of the cLN crystal is its high Li-deficiency leading to a large concentration of intrinsic defects. This results in a low optical damage threshold seriously limiting applications in electro-optics and non-linear optics requiring high energy laser radiation. It was found [5] that crystals grown under appropriate conditions from K_2O containing mixtures have lower intrinsic defect concentrations. Using similar procedures better optical parameters and a higher optical damage threshold can be achieved making the crystals more suitable for use in electro-optics and non-linear optics (Q-switching and frequency converters) [5, 6].

Later it was recognised that potassium itself does not enter the crystals grown in this way and lithium niobate crystals with the ratio near to [Li]/[Nb] ~ 1 (stoichiometric lithium niobate, sLN) can be grown. By now several other methods have also been developed for the preparation of sLN single crystals and the composition closest to 50 mol% Li_2O can be achieved by the high temperature top seeded solution growth (HTTSSG) method using a K_2O - Li_2O - Nb_2O_5 ternary mixture [7]. Such a solution is especially convenient for the growth of sLN crystals, since it significantly lowers the crystallization temperature determining the stoichiometry of the crystal [8, 9, 10].

The increasing need of high quality stoichiometric single crystals in the applications made it evident to look for other alkali metal oxides beyond potassium oxide in the hope that they can give us an easier growth process, lower crystallization temperatures or better yield of stoichiometric lithium niobate single crystals. For this end phase relations in the X_2O - Li_2O - Nb_2O_5 (X = Na, Rb or Cs) ternary systems were investigated, some of the corresponding phase diagrams were constructed, new phases were identified, growth processes were carried out and the crystals were characterized by spectroscopic methods.

The first chapter of my thesis reviews the $LiNbO_3$ crystal structure, phase diagram, crystal growth and characterization methods published in the literature. The experimental methods are described in the second chapter while chapter 3 contains a detailed presentation of the results. The work performed is summarized in chapter 4, and the new scientific results are listed in chapter 5.

1. Physics and chemistry of crystalline $LiNbO_3$

The first chapter summarizes basic knowledge about $LiNbO_3$ crystals. The crystallographic structure and the physical properties will be reviewed. The phase diagrams of the Li_2O - Nb_2O_5 binary and the K_2O - Li_2O - Nb_2O_5 ternary systems will be presented. Different crystal growth methods will be demonstrated with their advantages and disadvantages. The difficulties of the composition determination of the $LiNbO_3$ single crystal and suitable methods for an exact high precision composition calibration will be given.

1.1. The $LiNbO_3$ crystal structure

$LiNbO_3$ is an ionic material with partially covalent character. The structure of $LiNbO_3$ at room temperature belongs to the rhombohedral (trigonal) space group R3c, the corresponding point group is 3m. This form is stable up to the ferroelectric phase transition around 1200°C, where a transition to the nonpolar point group $\bar{3}m$ occurs (space group R$\bar{3}$c) (Fig. 1.1.). The unit cell parameters are given in Table 1.1.

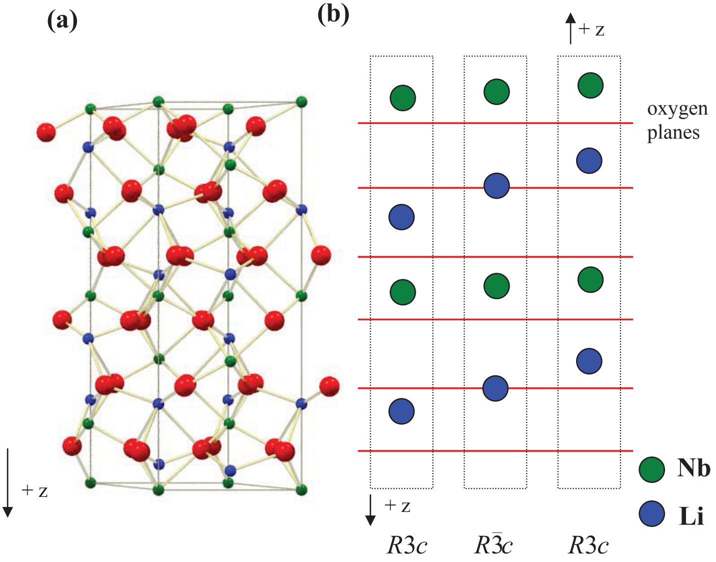

Figure 1.1. (a) Three dimensional model of the $LiNbO_3$ structure (red circles are oxide ions, blue ones are lithium ions and the green are niobium ions), (b) the displacement of cations relative to the oxygen planes for the two possible directions of polarization in the ferroelectric state [1]

Table 1.1. Unit cell parameters and density of $LiNbO_3$ in the hexagonal [4, 11, 12] representation

Point group: 3m

Space group: R3c

Parameters for hexagonal axes

	Congruent crystal	Stoichiometric crystal
a_H [Å]	5.15052(6)	5.14739(8)
c_H [Å]	13.86496(3)	13.85614(9)
d [g/cm^3]	4.648(5)	4.635(5)

number of formula units: 6 per unit cell

For describing the $LiNbO_3$ crystal symmetry two representations are used: the rhombohedral and the hexagonal. For the description of the physical properties an orthogonal representation is often used. The relations of these three representations are illustrated in Fig. 1.2.

In the rhombohedral setting the three axes are equal in length. The interaxial angles are also identical and are 55.87° for $LiNbO_3$ [13]. Each of the triad axes is a body diagonal of a rhombohedron. The axes of the rhombohedron form an angle of about 33° with the triad axes. Hexagonal axes are chosen perpendicular to the mirror planes (Fig. 1.2 b). According to the conventions, these hexagonal axes have to be chosen in such a way that the rhombohedron is in the obverse position. This obverse position is indicated in Fig. 1.2 (a) by dashed lines. The interrelation between the rhombohedral and the hexagonal axes imposes strict limitations on the possible indices of faces in the hexagonal system.

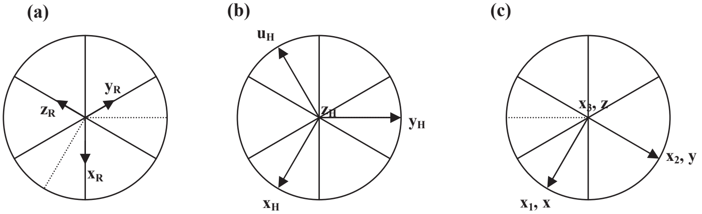

Figure 1.2. Choices of axes in point group 3m (a – rhombohedral, b – hexagonal, c – orthogonal). For case (a) only projections are shown

For most physical applications the orthogonal setting (Fig. 1.2 c) is preferred, with all axes orthogonal, but with different length. Tensor components of physical properties, such as elastic moduli, piezoelectric coefficients, dielectric constants, and others, are given with respect to these axes. In the present work the hexagonal and the orthogonal representations are used.

The frame of the crystal structure (Fig. 1.1) consists of oxygen octahedra sharing faces with each other and empiled along the polar z-axis. The space created by the oxide ions is occupied by the cations in alternating sequence and every third site is empty.

In the paraelectric state the Nb ion is in the centre of the oxygen octahedra while the Li ion is situated in the plane of the oxide ions. In the ferroelectric phase at 295 K the Nb ion is displaced by 0.277 Å and the Li ion by 0.675 Å in the same direction from their symmetrical positions. These displacements along the polar axis are the origin of the spontaneous polarization. An opposite displacement reverses the direction of spontaneous polarization [13, 14, 15] as shown in Fig. 1.1 b.

In ideal stoichiometric $LiNbO_3$ the Li sites are occupied by Li^+ and the Nb sites are occupied by Nb^{5+}. The presence of excess Nb^{5+} in congruent crystals leads to the formation of anti-site (Nb_{Li}) defets in the lattice Several models of instrinsic defects have been proposed in the literature to describe the congruent $LiNbO_3$ crystal. The Li vacancy model [16] assumes that the Nb sublattice is completely filled, extra Nb^{5+} ions enter Li sites forming anti-site defects. The charge neutrality is achieved by empty Li sites whose number is four times that of antisite Nb defects.

The Nb vacancy model [17] assumes Nb vacancies at the Nb site act as charge compensators for Li defficiency. Four vacant Nb sites are needed to compensate the charge of five Nb on antisites.

Abdi et al. [18] assumed that both Li and Nb vacancies can coexist to some extent, and that their ratio is determined by the crystal composition.

In both congruent and stoichiometric case the O positions are supposed to be completely filled.

1.2. Phase relations in the Li_2O - Nb_2O_5 binary system

The first phase diagram of the system Li_2O – Nb_2O_5 was published by Reisman and Holtzberg [19] describing two incongruently and two congruently melting compounds: lithium meta-niobate ($LiNbO_3$, melting point 1253 °C) and lithium ortho-niobate (Li_3NbO_4, melting point 1408 °C). Lerner et al. [16] made a substantial improvement, showing that $LiNbO_3$ has a fairly large solid solubility range, and the maximum melting temperature does not occur at the stoichiometric composition but between 48 and 49 mol% Li_2O. The congruent composition is reported to be between 48.35 and 48.60 mol% Li_2O [16, 20, 21, 22, 23, 24] depending on the purity of the starting materials, growth conditions, measuring methods and also on the direction of the crystal growth [21, 22]. In the homogeneity range (~ 47 – 50 mol% Li_2O [16]) the physical parameters are sensitively changing (e. g. lattice constant, density, ferroelectric Curie temperature, refractive index, phase matching temperature of the 2nd harmonic generation, the position of the ultraviolet absorption edge, position and shape of the OH^- vibration spectrum). Several calibration methods use these variations for the precise determination of the compositions of the crystals as will be shown later. A slight shift in the composition causes a large change in the physical parameters in this composition range; therefore the exact knowledge of the Li_2O content of the crystal is very important.

The clearest representation of the phase diagram was given by Svaasand et al. [25] shown in Fig. 1.3.

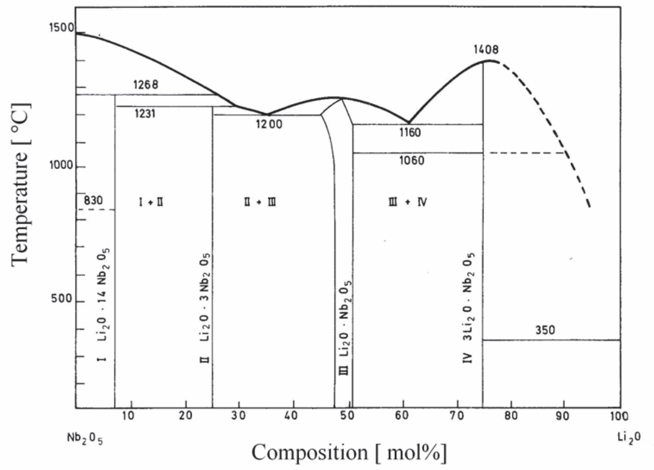

Figure 1.3. Phase diagram of the system Li_2O – Nb_2O_5 (Svaasand et al. [25])

While the congruent LN crystal can be grown easily with uniform composition, its high Li-deficiency limits the technical application in electro-optics and non-linear optics because the high number of intrinsic defects sensitizes the crystal against high energy laser radiation.

1.3. Phase relations in the K_2O - Li_2O - Nb_2O_5 ternary system

The investigations of the K_2O - Li_2O - Nb_2O_5 ternary system started in the 1960's. Potassium lithium niobate ($K_3Li_2Nb_5O_{15}$, KLN) with good non-linear optical and electrooptical properties was grown from this system [26, 27]. A new interest was given to the subject when the composition of lithium niobate (LN) grown from K_2O containing starting material was found to have better properties (sharper NMR and EPR lines) than those grown from congruent melt [28]. Based on these first results in-depth investigations of the ternary oxide system were started. It was established that lithium niobate bulk crystals with the compositions closest to stoichiometric can be grown from this system (Polgár et al. [9]). Within the confines of the lithium niobate existence field the phase boundaries of the stoichiometric lithium niobate existence field were determined as shown in Fig. 1.4.

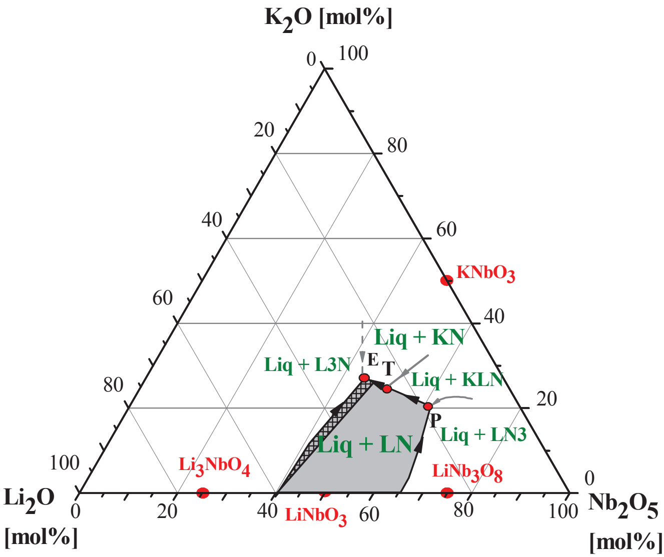

Figure 1.4. View of the polythermal projection of $LiNbO_3$ (LN) crystallization field in the K_2O - Li_2O - Nb_2O_5 ternary system where the grey region shows the crystallization region of $LiNbO_3$ while the area marked with squares corresponds to the crystallization region of stoichiometric $LiNbO_3$ phase [9], (KN = $KNbO_3$, L3N = Li_3NbO_4, KLN = $K_{6-x-y}Li_{4+x}Nb_{10+x}O_{30}$ ternary solid solution, where x = 0,51-0,55 and LN3 = $LiNb_3O_8$ phases, E is the ternary eutectic point, P is the peritectic point and T is the quasi-peritectic point of the system)

The $LiNbO_3$ liquidus surface is limited by four monovariant lines: Liq. + Li_3NbO_4 + $LiNbO_3$, Liq. + $KNbO_3$ + $LiNbO_3$, Liq. + KLN + $LiNbO_3$ and Liq. + $LiNb_3O_8$ + $LiNbO_3$. The ternary eutectic reaction [8] occurs at 997 °C: Liq. ↔ <β–Li_3NbO_4> + <$KNbO_3$> + <$LiNbO_3$>. The composition of the eutectic liquid (E) is 45.0 ± 1.5 mol% Nb_2O_5, 26.0 ± 1.5 mol% K_2O and 29.0 ± 1.5 mol% Li_2O. A quasi-peritectic reaction (Liq. + <KLN solid solution> ↔ <$KNbO_3$> + <$LiNbO_3$>) has also been identified at a temperature of about 1050 - 1055 °C. The quasi-peritectic liquid (T) has a composition roughly equal to: 49 mol% Nb_2O_5, 25.5 mol% K_2O and 25.5 mol% Li_2O.

Phase relations in the analogous X_2O - Li_2O - Nb_2O_5 (where X = Na, Rb or Cs) ternary systems have not been investigated yet. The first results will be reported for X = Na and Rb and the complete phase diagram at room temperature will be given for X = Cs in the present thesis.

1.4. Crystal growth processes

Congruent $LiNbO_3$ single crystals are generally grown by the Czochralski method even on the industrial scale. High purity materials are melted in a crucible and are solidified with the same composition on a crystal seed.

Several attempts have been undertaken to prepare crystals with stoichiometric ([Li]/[Nb]~1, sLN) composition. These crystals are expected to have less lattice defects and therefore better properties for high energy laser applications.

The preparation of stoichiometric samples from congruent single crystalline wafers or fibres was successful using the vapour transport equilibration (VTE) method where previously grown congruent samples were annealed in the vapour of Li-rich $LiNbO_3$ powder. The lithium enrichment of the crystal occurs via the vapour phase by diffusion. For thin samples this method yielded compositions rather close to the stoichiometric (49.95 mol% Li_2O [23]); the drawback is that for thicker crystals, extremely long diffusion times have to be used [23, 29].

Czochralski growth starting from stoichiometric and other off-congruent melts did not give satisfactory results, since the composition of the growing crystals was shifting along the growth axis as the growth proceeded.

The HTTSSG (High Temperature Top Seeded Solution Growth) method is a suitable method for growing sLN crystals up to 50 mol% Li_2O content. The method allows to decrease the crystallization temperature because the components of the desired substance are dissolved in a solvent (sometimes referred as “flux”), which is a molten salt. Choosing the right solvent is very important for the HTTSSG technique. The main selection criteria for the solvent are: the solvent should not react with the crystal material, should not enter the lattice as a dopant, should significantly lower the crystallization temperature and the temperature dependence of solubility of the solute in the flux should be positive and significant.

The K_2O - $LiNbO_3$ system has proved to be an ideal solvent system since K_2O does not enter the lattice whereas it significantly lowers the crystallization temperature [7, 30, 31]. It was established that the key parameter which determines the composition of the growing crystal is the growth temperature [31]. A lower temperature threshold for crystallization has been found to be at about 1114°C. The values of similar thresholds for possible new solvents clearly limit their choice for the growth of stoichiometric $LiNbO_3$ single crystals. From this it also follows that the Li-rich self-fluxes can never result in a Li/Nb ratio as close to 1 as the K^+ containing flux does, since according to the binary Li_2O - Nb_2O_5 phase diagram the temperature limit of growth in that system is at 1160 ^oC (see Fig. 1.4).

Kitamura et al. [32] improved the HTTSSG and invented a continuous filling double crucible method. They used a Li_2O-rich self-flux. During the growth a powder which has the same composition and amount as that of the pulled crystal is continuously refilled to the solution. Since the material pulled out is immediately recharged, the composition of the flux is kept constant and a crystal with uniform composition can be grown.

The Li_2O content in their starting mixture was 58 mol%, so the maximum attainable Li_2O content of the crystal by this method is 49.79 mol% limited by the phase relations in the Li_2O - Nb_2O_5 binary system.

Most of the methods applied for growing stoichiometric crystals produce stoichiometric or *nearly* stoichiometric $LiNbO_3$ with a real Li_2O content between ≈ 49.5 and 50.0 mol% in the crystal.

1.4.1. High temperature top seeded solution growth (HTTSSG) method

The starting materials (the solvent and the solute) are mixed and melted in a crucible and kept at high temperature for homogenization. An oriented crystal seed (with the same composition as that of the crystal to be grown) is brought into connection with the surface of the mixture. After reaching thermal equilibrium between the seed and the solution close to the saturation temperature, with the slow lowering of the temperature the crystal begins to grow on the seed with corresponding orientation. During the procedure the seed is rotated and pulled (fig. 1.5). The temperature programme of the growth is chosen in a way that the diameter of the crystal increases continuously from the few mm diameter of the seed crystal to the maximal size required and maintains this constant diameter till the end of the growth. If the crystal reaches the expected length, it is detached from the flux.

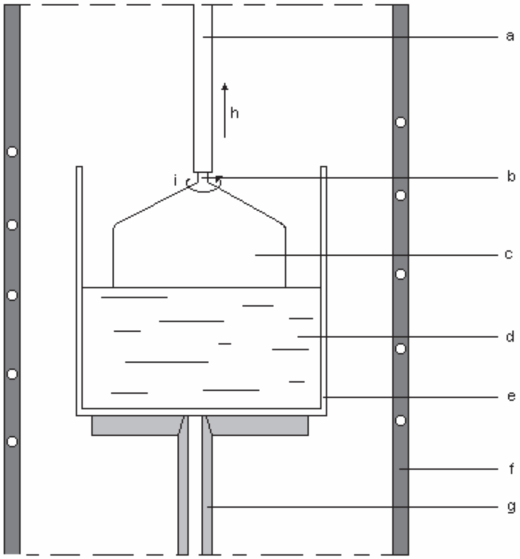

Figure 1.5.: Scheme of the HTTSSG equipment

a - pulling bar, b - seed, c – single crystal, d - flux, e - crucible, f – heating wire, g – crucible holder, h – direction of pulling, i – direction of rotation

At first sight the technical setup is very similar to that of the Czochralski growth but there are significant differences. In HTTSSG the temperature of the growing interface is diminishing during the crystal growth insuring the maintenance of the saturation conditions while in Czochralski method the temperature of the growing interface is constantly at the melting point. The typical pulling rate for HTTSSG is slow (0.1 – 10 mm/day) so the growth process can last several weeks which is at least ten times more than a Czochralski run. This implies that the requirements against the long term stability of the equipment are rather high which applies for the pulling rate, the rotation speed, and in particular the temperature.

Finding the good solvent is also crucial for the HTTSSG technique.

1.5. Crystal composition and characterization methods

As shown on the phase diagram (Fig. 1.3) $LiNbO_3$ has a homogeneity range between 47.5 – and 50 mol% Li_2O content at room temperature (see Fig. 1.3). The real composition can be expressed by the [Li] / [Nb] ratio. The determination of the main components (~ 50 mol%) with the application-required 0.01 mol% precision is not possible by quantitative chemical analysis. For atomic absorption spectroscopy (AAS) the accuracy of the measured Li_2O content is not better than 1-2 mol%.

Since several physical properties (e. g. Curie point, birefringence, phase-matching temperature for second harmonic generation, etc.) of lithium niobate are sensitive to the composition they can be used for the high precision determination of the crystal composition. A summary of calibration methods based on well-measurable physical properties is given in a review paper [33].

The determination of the interrelation between Curie temperature and melt stoichiometry was performed by Bergman et al. [34]. This temperature is shifting by 150 °C between 46 and 50 mol% Li content. Later on, Carruthers et al. [35] related the Curie point to the crystal composition. Polycrystalline samples were prepared and the Curie points of these samples have been compared to the single crystals pulled out from melts. With this method calibration between the Curie temperature and the crystal composition (Li content or [Li] / [Nb] ratio) can be done. The absolute accuracy of the Curie temperature measurement was estimated to be 0.3 and 0.6 °C (0.01 mol%) for single crystals and powders, respectively.

The phase matching temperature of the optical second harmonic generation sensitively depends on the crystal composition [36] and thus can be used for the characterization of the composition. The phase matching temperature can be measured with an accuracy usually better than 1 K yielding a theoretical sensitivity of better than 0.01 mol% for the composition determination.

The position of the fundamental absorption edge is also very sensitive to the composition of $LiNbO_3$ [37, 38]. Although the relationship is not linear, the measurement of the UV absorption edge is a very convenient way for characterizing the crystal composition. The position of the band edge was defined as the wavelength where the absorption coefficient is 20 cm^{-1}. This non-destructive, fast and simple method can be applied at room temperature for the wide range between sub-congruent and stoichiometric compositions with a very high accuracy (a relative accuracy of better than 0.01 mol%, see calibration curve in Fig. 1.6).

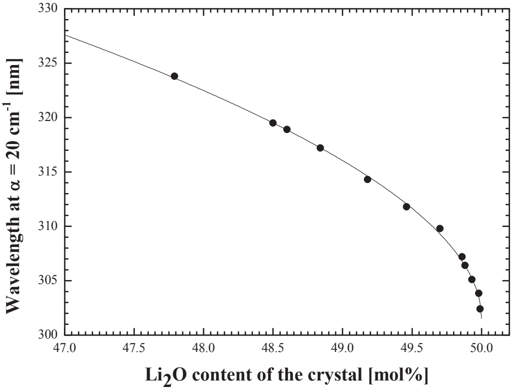

Figure 1.6. Calibration curve between the crystal composition and the UV absorption edge position [38], Li_2O content of the samples was determined by using calibration based on the phase matching temperature of the optical second harmonic generation.

Another spectroscopic method which can be used for composition determination is OH^- vibrational spectroscopy. OH^- ions are always present in air-grown $LiNbO_3$ crystals [39], their vibrations can be easily measured by infrared (IR) spectroscopy. The peak intensities and positions in the IR spectrum are sensitive to the composition of the crystal. In congruent $LiNbO_3$ the absorption band of the OH^- stretching mode peaking at ≈ 3485 cm^{-1} has a full width at half maximum (FWHM) of about 30 cm^{-1} due to several overlapping components. In nearly stoichiometric $LiNbO_3$ crystals only two relatively sharp band components appear at about 3465 and 3480 cm^{-1} [7] (Fig. 1.7). These phenomena are of structural origin [40].

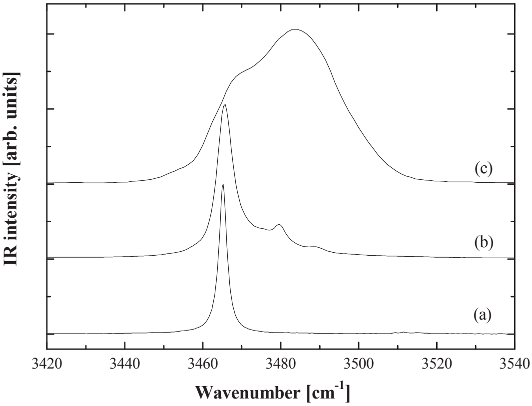

Figure 1.7. Typical IR spectrum of stoichiometric: [Li_2O] = 50.0 mol% (a), nearly stoichiometric: [Li_2O] = 49.7 mol% (b) and congruent: [Li_2O] = 48.7 mol% (c) $LiNbO_3$ [7]

The main band observed at 3465 cm^{-1} is characteristic of the perfect stoichiometric $LiNbO_3$ crystal, while the satellite band at about 3480 cm^{-1} is related to intrinsic defects still present due to incomplete stoichiometry. The satellite band at 3480 cm^{-1} completely disappears in the spectrum of the stoichiometric crystal and only a sharp peak at 3465 cm^{-1} can be observed with an FWHM of at about 2-3 cm^{-1}. It has been observed that the intensity ratio $R = I_{3480} / I_{3465}$ of the two components changes with the Li_2O content in the $\approx 49.5 - 50.0$ mol% range [33], therefore R may be used for the estimation of the crystal composition. Up to now, however, no such calibration has been performed due to the shape of the OH^- band, which depends slightly on the impurities and the time passed since the crystal was grown.

The third spectroscopic method used for composition calibration during my PhD work was the Raman scattering technique. With this method the vibrational modes of the chemical bonds can be studied. For the 3m symmetry ($LiNbO_3$) the vibrational modes can be divided into three kinds of groups marked with A_1, A_2 and E. In the Raman spectrum of $LiNbO_3$ four A_1 and nine E modes can be found (the five A_2 modes are Raman inactive). These modes are characteristic of the Li and the Nb vibrations interacting with the oxygen cage. The displacement patterns corresponding to different modes were investigated by Caciuc et al. [41]. They found that the A_1(TO1) transverse optical mode corresponds to the movements of the Nb ions while the A_1(TO2) mode reflects mainly the Li movement. The Nb and Li vibrations in the E modes are confined to the *(xy)* plane, while those in the A modes to the *(z)* direction. These modes are sensitive to the stoichiometry of the $LiNbO_3$ crystals, resulting in the shift and broadening of some Raman bands, which can be used for composition determination. For an accurate determination of the composition generally the FWHM of the E-mode at 156 cm^{-1} was chosen [18, 42-49] because it shows weak directional dispersion and does not overlap with other bands (Fig. 1.8).

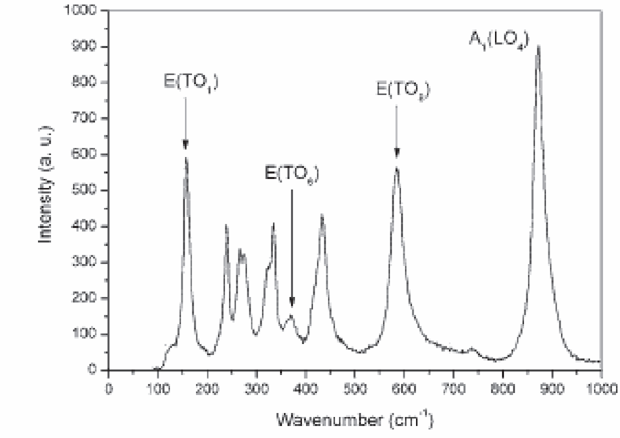

Figure 1.8. E(TO) and A_1(LO) modes of a congruent lithium niobate crystal in the Raman spectra excited by He-Ne laser (633 nm) in z(xx)z polarization [50]

There are several calibrations for the composition determination in the literature using FWHM values of the E(TO1) mode [18, 42-49]. Fig. 1.9 summarizes these calibration lines corresponding to the different measurements in the near stoichiometric range.

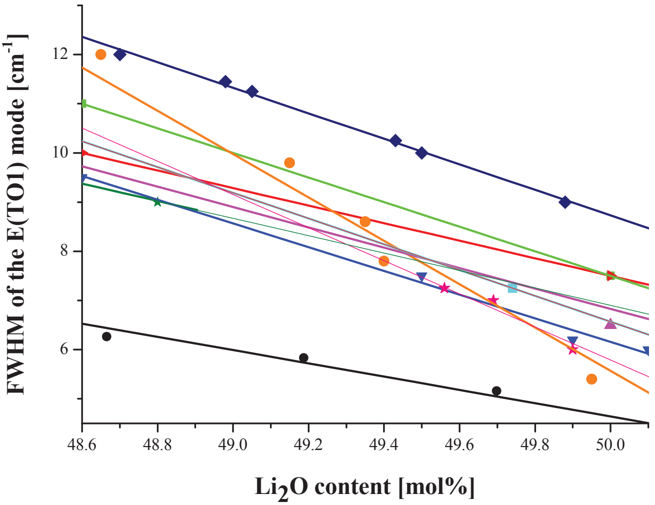

	Reference	**Orientation**	**Laser**
●	Bernabé [42]	Z(X+Y,X+Y)Z	Ar (488 nm)
▼	Malovichko [43]		
▶	Sidorov [44]	Y(ZX)Z	Ar (514.5 nm)
■	Sidorov [44]	Y(ZY)Z	Ar (514.5 nm)
★	Savova [45]		Ar (488, 514.5 nm)
●	Zhang [46]	Z(YX)Z	He-Ne (633 nm)
■	Ridah [47]	X(ZY)Z	Ar (514.5 nm)
▲	Schlarb [48]	Z(YZ)X	Ar
★	Fontana [49]		Ar (514.5 nm)
◆	Abdi [18]		He-Ne (633 nm)

Figure 1.9. Calibration lines for composition determination using FWHM of the E(TO1) Raman mode taken from the literature

It can clearly be seen that they are quite different. The FWHM values depend on the polarization and the wavelength of the exciting laser as well. Spectra measured on the same sample with the same exciting laser but in different polarization may give different FWHM values for the E(TO1) mode as it was shown by Sidorov et al. [44]. Comparing the results obtained from Ref. [43] and Ref. [46] we can see that crystals with the same composition and with the same orientation but excited by different lasers

(He-Ne and Ar) provide different FWHM values. The results can be influenced by other factors as well, like the spectrometer resolution [42] and the quality of the sample surface [51].

It can be concluded that a universal calibration cannot be done by Raman measurements without any correction. A calibration based on the FWHM of the E(TO1) Raman mode can only be used locally, assuring identical circumstances for all studied samples.

2. Experimental methods and instruments

In the second part of the thesis the experimental work will be shown. The used basic materials and their treatment for the different experiments and the methods and instruments for this work will be presented in detail. The process for combining these methods for gaining more accurate information will be described.

2.1. Solid state reactions, thermoanalytical investigations and phase characterization

In order to understand the role of the alkali metal oxide solvents in the growth of sLN crystals several methods have been combined. Series of X_2O - Li_2O - Nb_2O_5 (X = Na, Rb, and Cs) polycrystalline samples were prepared by solid state reaction for thermal analytical, x-ray powder diffraction and crystal growth investigations.

The raw materials used were Na_2CO_3 (Merck, analytical grade), K_2CO_3 (Merck, analytical grade), Rb_2CO_3 (99,9 % (Johnson-Matthey), Cs_2CO_3 (Merck, extra pure), Li_2CO_3 (Merck, Suprapur) and Nb_2O_5 (Starck, LN grade). The sample preparation was carried out in a high temperature electric furnace. In all cases the starting materials were dried (200 °C for 12 hours), weighed with 0.1 mg precision, mixed and reacted in solid phase (800 °C for 3 hours) then cooled to room temperature and reground. The release of the whole amount of CO_2 was controlled by weighing. The samples used for thermal analyses and for crystal growth were prepared by a second reaction step: melted at 1200°C or sintered just below the melting temperature (1100 ^oC), respectively. The constituent phases were assessed by X-ray phase analysis with a Philips PW 1710 diffractometer using Cu K_α radiation in the 2Θ range of 0-80^o for the measurements described in chapter 3.1.1. For the results in chapter 3.1.2. an INEL MPD CPS 120 diffractometer was used.

DSC measurements were used to determine the phase transition temperatures of X_2O - Li_2O - Nb_2O_5 (X = Na, Rb or Cs) polycrystalline samples in the composition range of [X] = 10-16 mol% and [Li]/[Nb] = 1. The DSC curves were recorded with a PL Thermal Sciences 1500 differential scanning calorimeter in Ar atmosphere with Al_2O_3 as the reference material. The calibration of the system was done by using 6N pure standard metals (In, Sn, Pb, Zn, Al, Ag, Au, Si). The calorimeter was heated up to 1370^{o}C at a rate of 10^{o}C/min and then cooled down at the same rate to 300^{o}C.

For the determination of the phase transition temperatures the heating part of the curves was taken into account in order to eliminate the mistakes from supercooling.

The compositions of the polycrystalline samples are represented in a ternary diagram shown in Fig. 2.1.

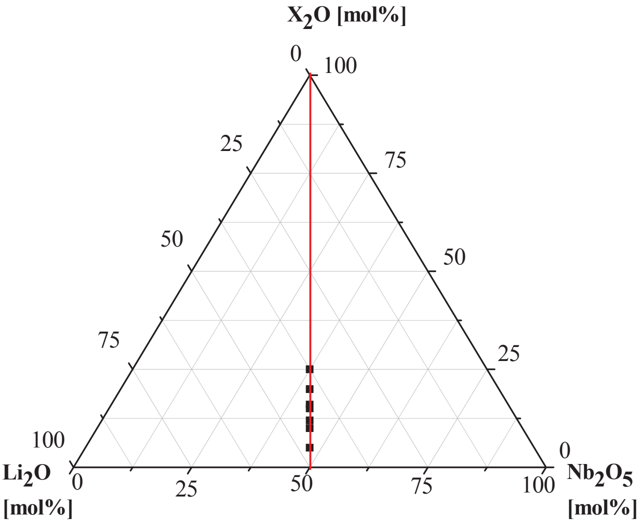

Figure 2.1. Representation of the selected compositions of the polycrystalline samples along the [Li] / [Nb] = 1 line (where X is a selected alkali metal ion)

From the measured phase transition temperatures a vertical cut of the ternary phase diagram can be constructed (Fig. 2.2) and the most suitable composition for crystal growth can be chosen.

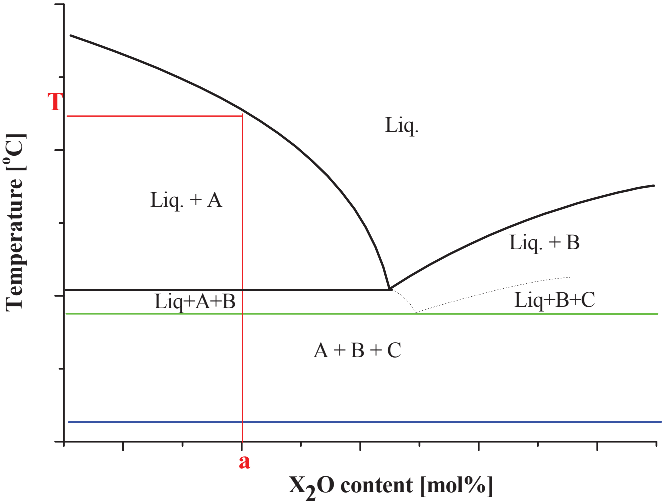

Figure 2.2. Typical vertical section of the ternary phase diagram along the $LiNbO_3$-X_2O join constructed from DTA and X-ray results (where the horizontal lines correspond to an eutectic (green line) and a subsolidus (blue line) reaction, *A*, *B* and *C* are the identified phases (A = the phase to be crystallized, Liq. = liquid phase), **a** is the selected starting composition for crystal growth and T is the crystallization temperature)

Crystal growth experiments were carried out from a selected flux composition (**a** in Fig. 2.2). The growth process was conducted further than the single *A* phase crystallization limit (in our case *A* = $LiNbO_3$ phase). This way the maximum amount of the $LiNbO_3$ phase was pulled out and the composition of the liquidus phase boundary could be determined. New phases appeared at the bottom of the LN crystals which were assessed by X-ray diffraction analysis. The separation of the consecutively crystallizing phases, their qualitative and quantitative analysis yielded data on the evolution of the monovariant lines.

2.2. Crystal growth and refinement of the phase diagram

Crystal growth was done by the HTTSSG method from fluxes along the line in the ternary diagram joining to the $LiNbO_3$-X_2O join of the X_2O – Li_2O – Nb_2O_5 (X = Na, Cs or Rb) ternary systems from the starting composition of X_2O = 10 mol% and $[Li_2O] / [Nb_2O_5]=1$.

For the growth experiments <00.1> oriented $LiNbO_3$ seeds were used. The crystals were pulled at rates of 0.3-0.5 mm/h and rotated with 8-10 rpm (rotation / minute).

If it is assumed that the system shows no solid solubility for the X ion (it does not enter into the LN lattice) the compositional changes which occur during the solidification may be simply traced. In a first approximation, assuming a stoichiometric composition for the crystallized solid phase, the actual alkali oxide concentration of the liquid can be calculated from the pulled amount of the crystal. The real solid composition (the Li_2O content) of the pure LN crystals can be determined by ultraviolet/visible (UV/Vis) spectroscopic measurements. In the previous studies K_2O based fluxes proved to be ideal solvents [7] therefore a similar behaviour was expected also for the other alkali ions.

The crystallization temperature of the lithium niobate crystal at a given composition can be deduced from the DTA measurements of the polycrystalline samples with the same composition as the actual flux from which the crystal is growing. The composition of different parts of the crystals was determined from slices cut perpendicular to the growth axes of the pulled-out $LiNbO_3$ crystals.

The knowledge of these two sets of data lets us determine the corresponding liquidus and solidus points (tie-lines) (Fig. 2.3).

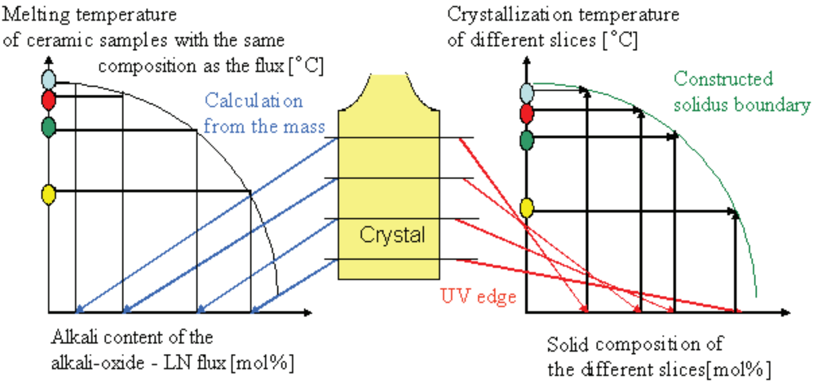

Figure 2.3. Method of refinement of the phase diagram using the combination of crystal growth, DSC and spectroscopic experiments

If the flux enters the crystal lattice the composition of the liquid and the solid phase in equilibrium must be followed by chemical analysis. Therefore the actual Na, Rb and Cs content of the crystals was analyzed by a Varian SpectrAA-20 atomic absorption spectrometer.

2.3. Spectroscopy

The Li_2O content of different parts of the $LiNbO_3$ crystals was determined by a calibration based on the UV absorption edge position which was measured by a two-beam Jasco V-550 UV/VIS spectrometer with a best resolution of 0.05 nm. Reflection correction had to be used before the evaluation of the spectra because of the high refractive index of the crystal. With this correction the error caused by the multiple reflected light beams can be avoided. The correction used is described in detail in Ref. [38].

The IR spectra were recorded at room temperature by a Bruker IFS 66v/S FTIR spectrometer in the 400-7000 cm^{-1} wavenumber region with a resolution of 0.5 cm^{-1}.

Raman measurements were carried out by a Renishaw RM1000 confocal micro-Raman spectrometer using 633 nm He-Ne laser excitation (with a spectral resolution of about 3 cm^{-1}) for the investigations described in chapter 3.3.2.1. Other Raman spectra (chapter 3.3.2.2. and 3.3.2.3.) were measured by a Labram spectrometer (Jobin-Yvon) using 633 nm He-Ne and 514.5 nm Ar-ion laser sources.

3. Results

The third chapter specifies the information gained from the different experiments. First the results on X_2O - Li_2O - Nb_2O_5 (X = Na, Rb, Cs) polycrystalline samples will be shown, their thermoanalytical properties and their constituent phases at room temperature. The ternary phase diagram of the Cs_2O - Li_2O - Nb_2O_5 system will be discussed. Crystal growth results, photos of the crystals, their composition and the refinement of the phase relations will also be presented. For the determination of the Li_2O content two vibrational spectroscopic methods will be presented: IR spectroscopy of OH^- vibrations and Raman spectroscopy.

3.1. Phase identification and phase diagram determined on polycrystalline samples

3.1.1. Thermal analysis and X-ray phase identification in the X_2O - Li_2O - Nb_2O_5 ternary systems

The composition of the samples was chosen along the [Li] / [Nb] = 1 line so we can directly use the gained thermal analytical information for choosing the starting melt compositions for the growth of stoichiometric $LiNbO_3$ crystals from these ternary systems.

DSC curves and X-ray diffraction patterns for all X_2O - Li_2O - Nb_2O_5 systems are shown in Figs. 3.1 and 3.2.1-3, respectively. Similarly to the previously investigated K_2O - Li_2O - Nb_2O_5 system X-ray assessment reveals LN as the major phase. L3N and the alkali niobate phases are present as minor constituents.

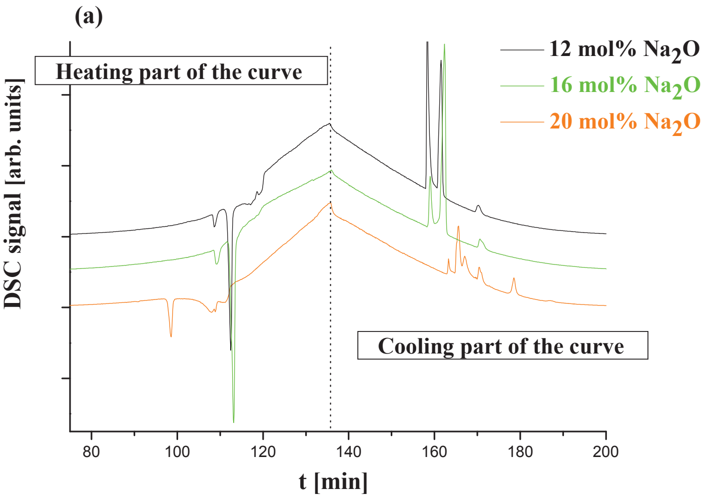

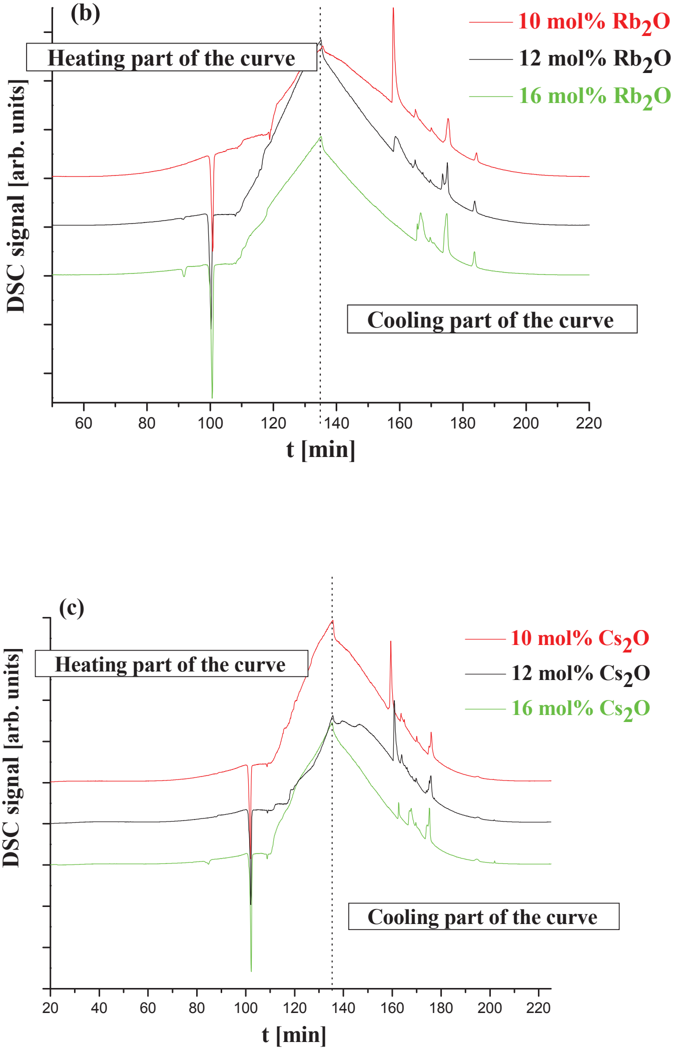

Figure 3.1. Thermal analytical (DSC) curves of the X_2O - Li_2O - Nb_2O_5 samples with [Li]/[Nb] = 1, (X = Na (a), Rb (b), Cs (c))

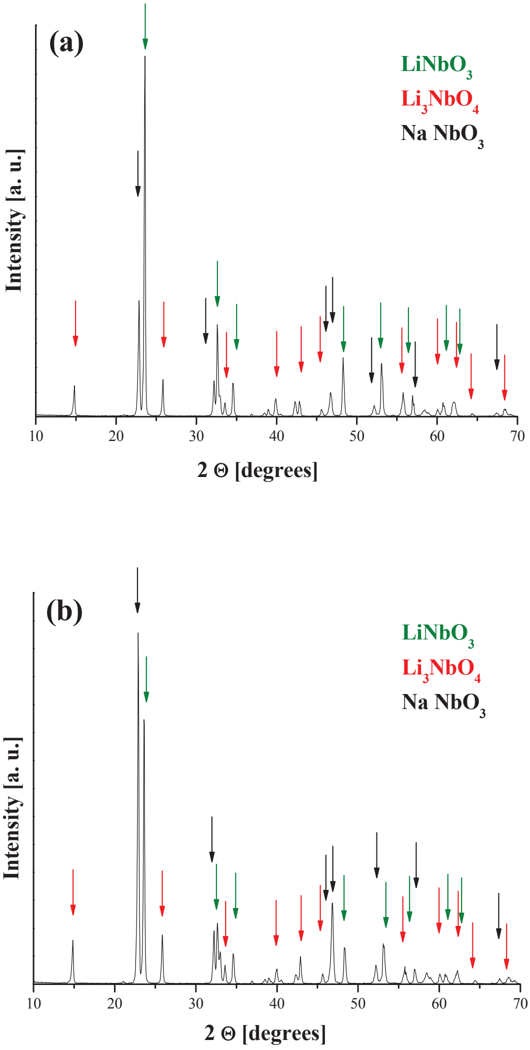

Figure 3.2.1. X-ray diffractograms of the Na_2O - Li_2O - Nb_2O_5 samples with [Li]/[Nb] = 1, (a) 12 mol% Na_2O content, (b) 16 mol% Na_2O content

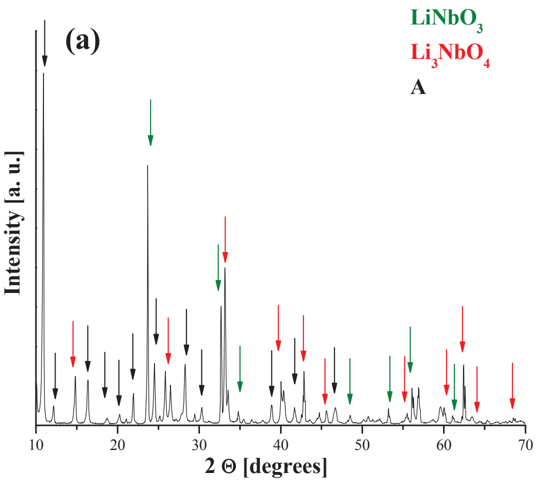

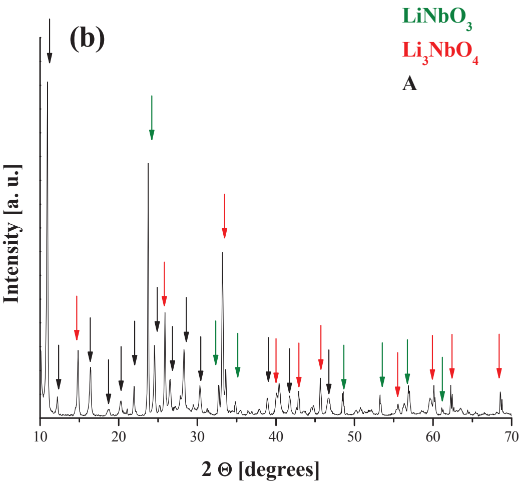

Figure 3.2.2. X-ray diffractograms of the Rb_2O - Li_2O - Nb_2O_5 samples with [Li]/[Nb] = 1, (a) 12 mol% Rb_2O content, (b) 16 mol% Rb_2O content. Unidentified Rb – Nb - (Li) oxide phases were marked with *A*.

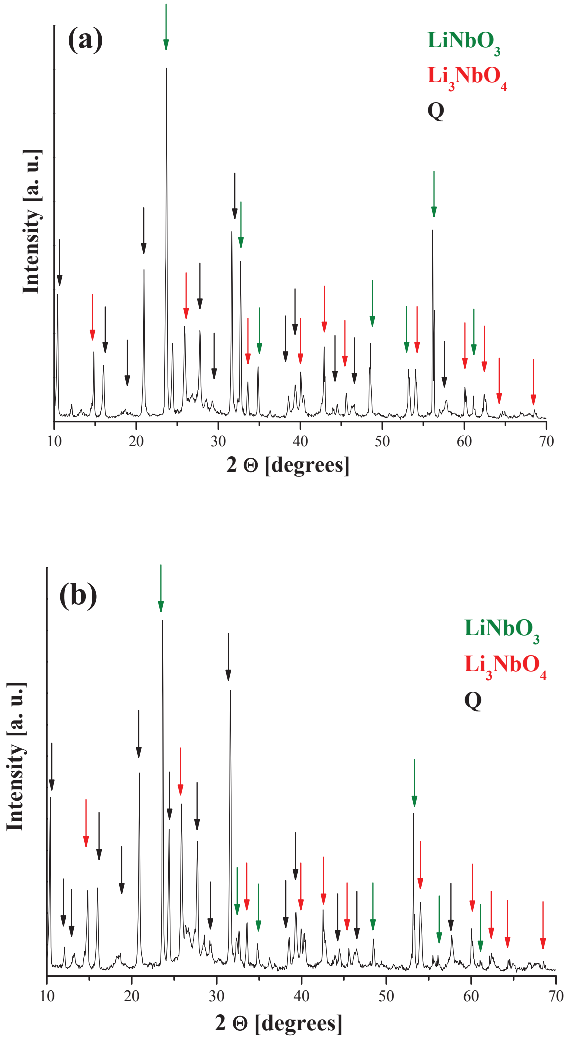

Figure 3.2.3. X-ray diffractograms of the Cs_2O - Li_2O - Nb_2O_5 samples with [Li]/[Nb] = 1, (a) 12 mol% Cs_2O content, (b) 16 mol% Cs_2O content. Unidentified Cs – Nb - (Li) oxide phases were marked with *Q*.

Table 3.1. Sample compositions, the observed phases at room temperature and the results of DSC analysis from samples with [Li]/[Nb] = 1. T1 and T2 denote the temperatures of the starting Liquid → LN single- and Liquid → LN + L3N two phase crystallization processes, respectively. T3 stands for the ternary eutectic reaction Liquid → LN + L3N + alkali-niobate, and T4 is attributed to the LN + alkali-niobate → L3N + Q quasi-peritectoid reaction. (LN = lithium niobate, L3N = lithium (-orto) niobate, KLN = potassium lithium niobate, A, Q = unidentified Li_2O- Nb_2O_5- X_2O mixture).

Sample	Composition [mol%]			Observed phases by X-ray diffraction at room temperature			Observed phase transition temperatures from DSC analysis [°C]			
	Li_2O	Nb_2O_5	X_2O	Main phases	Residual phases		T1	T2	T3	T4
K-10	**45**	**45**	**10**	**LN**	**L3N**	**$KNbO_3$**	**1164**	**1053**	**994**	**965**
K-12	**44**	**44**	**12**	**LN**	**L3N**	**$KNbO_3$**	**1141**	**1056**	**996**	**965**
K-16	**42**	**42**	**16**	**LN**	**L3N**	**$KNbO_3$**	**1070**	**1059**	**997**	**967**
K-20	**40**	**40**	**20**	**L3N**	**KLN**	**$KNbO_3$**			**996**	**969**
Na-12	44	44	12	LN	L3N	$NaNbO_3$	1169	1142	1099	1064
Na-16	42	42	16	LN	L3N	$NaNbO_3$	1160	1140	1100	1065
Na-20	40	40	20	LN	L3N	$NaNbO_3$			1090	1063
Rb-10	45	45	10	LN	L3N	A	1187	1062	981	907
Rb-12	44	44	12	LN	L3N	A	1163	1062	981	898
Rb-16	42	42	16	LN	L3N	A		1061	982	897
Cs-10	45	45	10	LN	L3N	Q	1186	1065	994	857
Cs-12	44	44	12	LN	L3N	Q	1163	1063	993	854
Cs-16	42	42	16	LN	L3N	Q		1064	995	854

The results of the DSC measurements (the thermal reactions detected) and the RT XRD phase analyses are summarized in Table 3.1. Previous measurements in the K_2O containing system are included for comparison (bold) with the actual results.

The highest-temperature peak (T1) depends on the alkali metal oxide content of the samples and was identified as the crystallization temperature of the LN phase. The temperatures of the other peaks were characteristic of the given alkali metal oxide (X). These peaks were assigned to invariant reactions, as in the K_2O - Li_2O - Nb_2O_5 system (T2: two-phase crystallization processes of Liquid → LN + L3N or Liquid → LN + alkali niobate, T3: ternary eutectic reaction of Liquid → LN + L3N + alkali-niobate, and T4: quasi-peritectoid reaction.

For the same alkali metal content the crystallization temperature of $LiNbO_3$ single phase (T1) was the highest using fluxes with Na_2O. Although Rb_2O and Cs_2O based fluxes result in almost the same crystallization temperature, they are still somewhat higher than that of the K_2O containing flux (Fig. 3.3). The temperatures of the invariant reactions were also higher for Na_2O containing samples than those of K_2O, Rb_2O and Cs_2O.

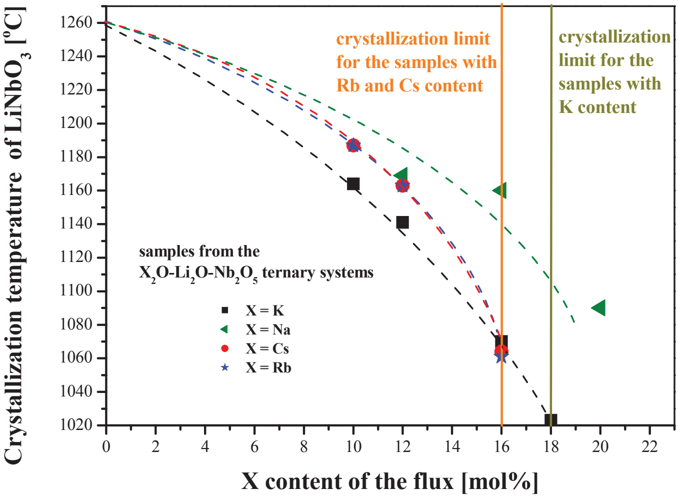

Figure 3.3. Crystallization temperatures of the samples from the X_2O - Li_2O - Nb_2O_5 systems (X = Na, Rb, Cs) compared with the crystallization temperatures of samples from the K_2O - Li_2O - Nb_2O_5 system along the Li / Nb=1 isopleth

The ternary liquid composition corresponding to the limit of the $LiNbO_3$ liquidus surface (i.e. starting of the co-crystallization processes of the LN + L3N phases) can be estimated from our measurements to be near 16 mol% X_2O for the systems with Rb_2O and Cs_2O and with [Li]/[Nb] = 1 ratio (for the K_2O - Li_2O - Nb_2O_5 system this value is 18 mol% [31]).

3.1.2. Phase diagram of the $Cs_2O – Li_2O – Nb_2O_5$ ternary system

According to the thermal analytical results detailed above – beside K_2O –Rb_2O and Cs_2O have a chance to be suitable for the growth of sLN with low crystallization temperature and high yield.

The ionic radius of Cs is the largest among all examined alkali ions so from a stereo chemical point of view it might be the best candidate for a solvent constituent. This is why the $Cs_2O – Li_2O – Nb_2O_5$ ternary system was selected as a first candidate for a detailed thermal analytical investigation [52].

Four isopleths were selected for investigation: the first (a) corresponds to the composition of [Li] / [Nb] = 1 (between 5-25 mol% Cs_2O), the second (b) to the 50 mol% Nb_2O_5 line (between 10-50 mol% Cs_2O), and the last two to the 10 mol% (c) and 20 mol% (d) Cs_2O content (between 35 - 55 mol% Nb_2O_5) (Fig. 3.4).

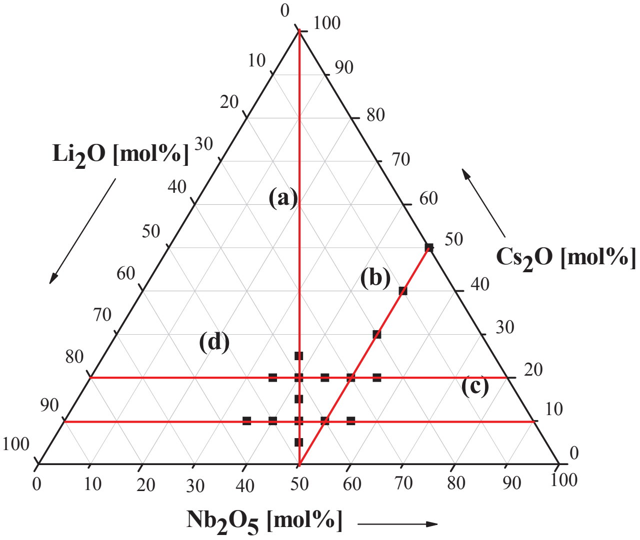

Figure 3.4. Composition of polycrystalline samples investigated by X-ray diffraction

The constituent phases were assessed by X-ray powder diffraction and the analyses were used to outline the boundaries of the constituent phases stable at RT. In the investigated compositional region different types of XRD patterns were found (Fig.3.5.1-3, the rest can be found in the appendix).

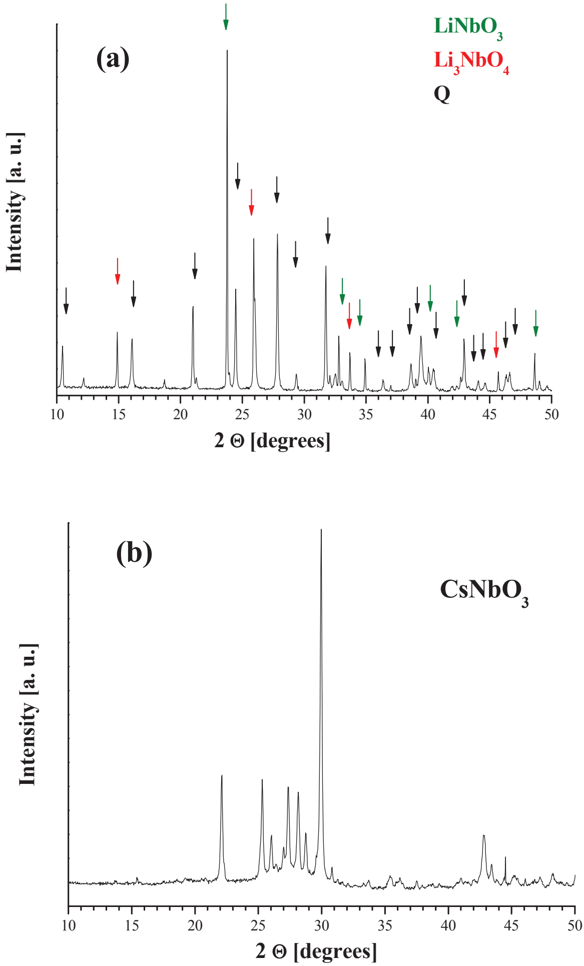

Figure 3.5.1. X-ray diffractograms from the investigated region with the identified phases 1: compositions of the samples: 20 mol% Cs_2O, 30 mol% Li_2O, 50 mol% Nb_2O_5 (a), 50 mol% Cs_2O, 50 mol% Nb_2O_5 (b). The unidentified peaks were signed with Q.

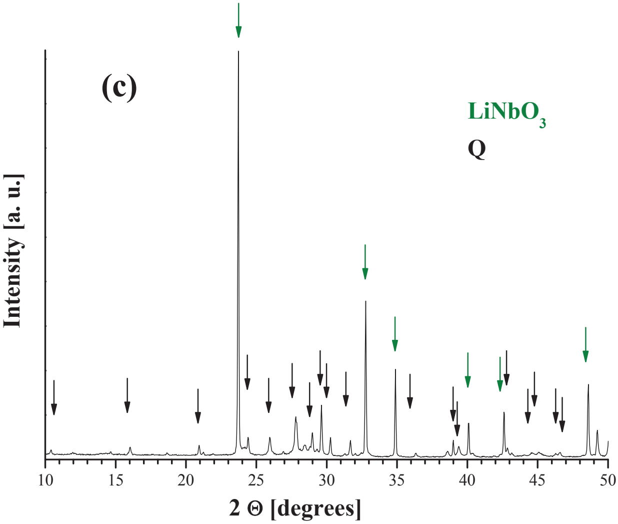

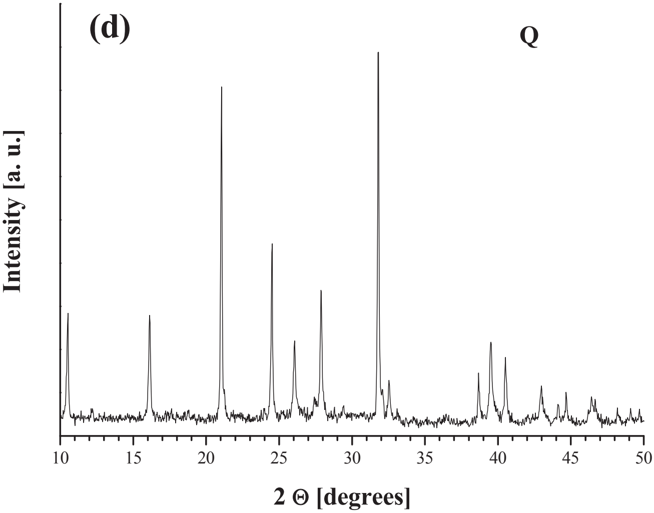

Figure 3.5.2. X-ray diffractograms from the investigated region with the identified phases 2: compositions of the samples: 10 mol% Cs_2O, 35 mol% Li_2O, 55 mol% Nb_2O_5 (c), 40 mol% Cs_2O, 10 mol% Li_2O, 50 mol% Nb_2O_5 (d). The unidentified peaks were signed with Q.

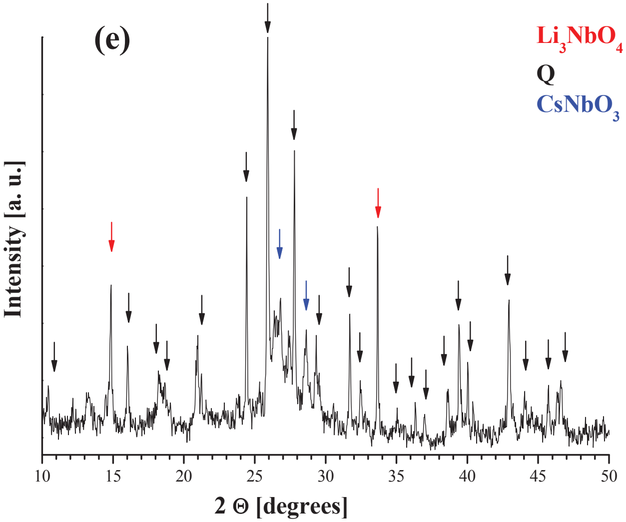

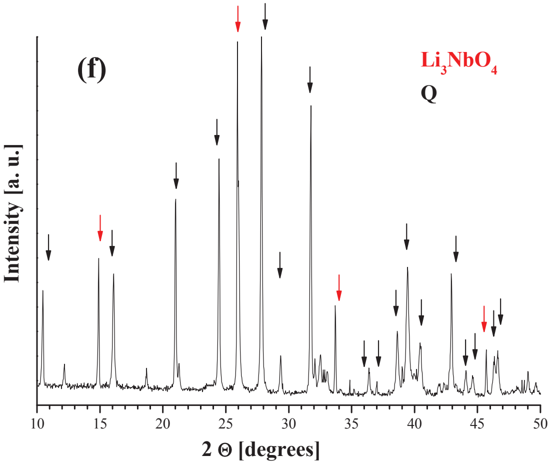

Figure 3.5.3. X-ray diffractograms from the investigated region with the identified phases 3: compositions of the samples: 25 mol% Cs_2O, 37.5 mol% Li_2O, 37.5 mol% Nb_2O_5 (e), 20 mol% Cs_2O, 40 mol% Li_2O, 40 mol% Nb_2O_5 (f). The unidentified peaks were signed with Q.

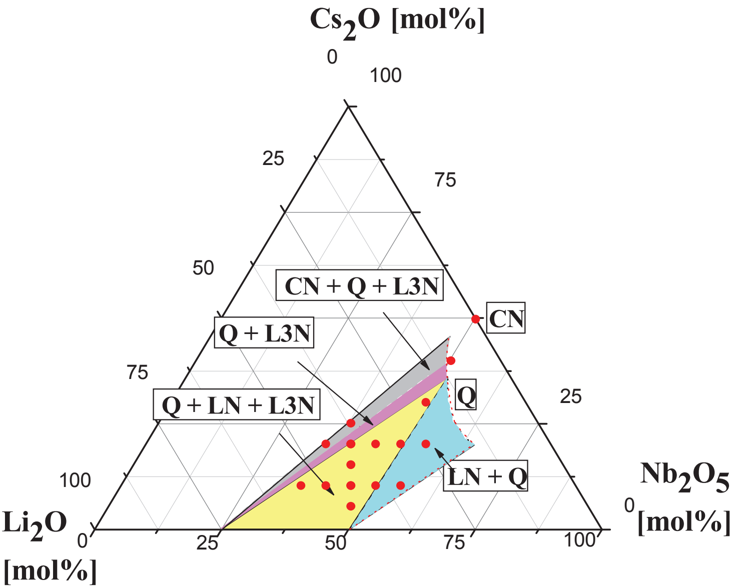

Figure 3.6. Subsolidus phase diagram of the Cs_2O - Li_2O - Nb_2O_5 ternary system at room temperature ($CN = CsNbO_3$, $LN = LiNbO_3$, $L3N = \beta\text{-}Li_3NbO_4$, Q = ternary solid solution of Cs - Li - Nb oxide, dashed red lines are estimated borders)

The identified phases at room temperature in the investigated part of the diagram as shown in Fig. 3.6 were the following:

- a single-phase domain called "Q"
- two two-phase domains: Q + β-Li_3NbO_4 (L3N) and Q + $LiNbO_3$ (LN)
- two three-phase regions: $CsNbO_3$ (CN) + Q + β-Li_3NbO_4 and Q + $LiNbO_3$ + β–Li_3NbO_4

The same series of peaks corresponding to the unidentified "Q" phase was found in the spectra of all investigated samples except for $CsNbO_3$ (Fig. 3.5.1. b). The spectrum of the 40 mol% Cs_2O, 10 mol% Li_2O, 50 mol% Nb_2O_5 sample (Fig. 3.5.2. d) contains only the Q peaks, so it can be identified as a single phase domain.

3.2. Single crystal growth and characterization

3.2.1. Crystal growth experiments in the X_2O – Li_2O – Nb_2O_5 ternary systems

Single crystals from melts of ternary compositions were grown by the HTTSSG method [7]. Based on the thermal analytical results (Fig. 3.7), detailed in chapter 3.1.1., the crystal growth experiments were started from 10 mol% alkali metal oxide (X_2O) content with [Li]/[Nb] = 1.

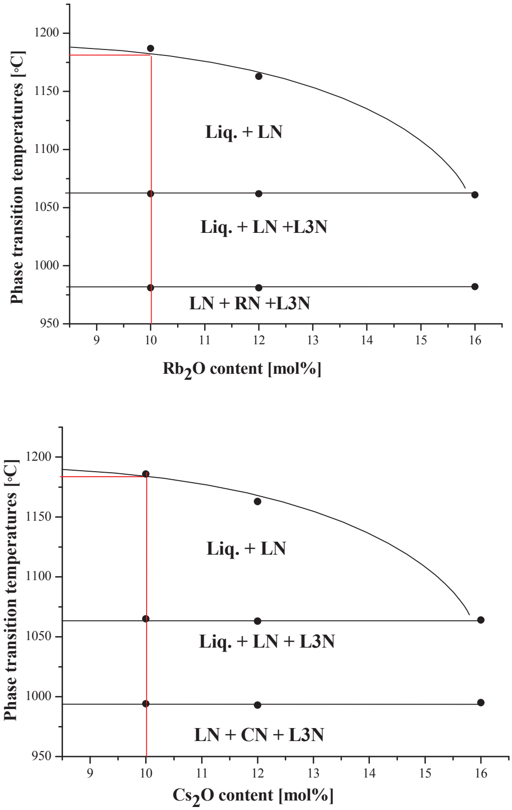

Fig. 3.7. Constructed phase diagram from DTA results (where black dots are the measured phase transition temperatures, horizontal straight lines correspond to subsolidus reactions). The red lines show the selected growth compositions (10 mol% in both cases) and the corresponding crystallization temperature (at about 1185 °C). RN and CN correspond to the $RbNbO_3$ and the $CsNbO_3$ phases.

By choosing this concentration it was possible to embrace a concentration range from 10 mol% to the single phase boundary.

The growth experiments were successful for all examined alkali fluxes. Transparent and crack free crystals of 4-5 cm length could be grown starting from the composition of 10 mol% alkali content with [Li]/[Nb] = 1 (Fig.3.8).

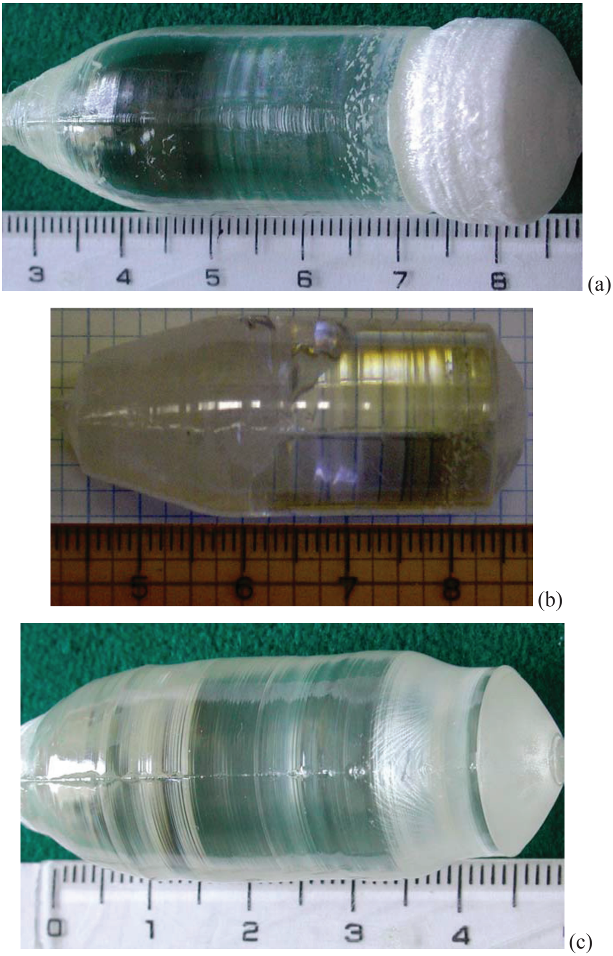

Figure 3.8. Crystals grown from 10 mol% alkali content (Rb_2O – a, Cs_2O – b and Na_2O – c) with [Li]/[Nb] = 1

The growth process was conducted until the liquid composition reached one of the monovariant lines (the limit of the crystallization field of the primary LN phase). In this way the maximum amount of the LN phase was pulled out and the crystallization yield was determined (Table 3.2).

Table 3.2. Starting compositions used for growth experiments, the experimentally obtained yield of the LN phase and the X content of the crystal and the residue.

X	**Liquid composition [mol%]**			**Yield [LN]/[flux] [wt%]**	**X content in the crystal [mol%]**	**X content in the residue [mol%]**
	Li_2O	**Nb_2O_5**	**Alkali oxide**			
Na	45	45	10	36.6	5.7	12.7
Rb	45	45	10	38.4	0.015	16.5
Cs	45	45	10	37.9	0.0002	15.8

At the end of the $LiNbO_3$ crystallization a white polycrystalline mass was grown, which contained two phases assessed by X-ray analysis.

The polycrystalline phase was identified as a mixture of $LiNbO_3$ and Li_3NbO_4 for crystals grown from Rb_2O- and Cs_2O-based flux, the same as before for the K_2O-based flux, while for Na_2O containing flux $LiNbO_3$ and $NaNbO_3$ were found.

Both in the single LN phase (samples cut from the clear part of the crystals) and in the two phase region of the crystals grown from Rb_2O- and Cs_2O-based fluxes, only traces of Rb and Cs ions (i.e. 10^{-3} – 10^{-4} atom/mol or less, Table 3.2.) were detected by atomic absorption spectroscopy, similarly to the previous results reported on the incorporation of K ions in the crystals grown from K_2O containing flux [7]. The behaviour of Na ion~~s~~ was different. According to our AAS measurements Na ions do enter the crystal lattice with an average segregation coefficient of $k_{sol/liq}$ (Na_2O) ~ 0.2.

Since K_2O, Rb_2O and Cs_2O are practically insoluble in lithium niobate the evolution of the liquid composition may be traced during the crystallization of the LN phase. Assuming constant [Li]/[Nb] = 1 ratio, for Rb_2O and Cs_2O containing fluxes the alkali oxide content of the liquid at the crystallization limit of the LN phase was found to be 16.5 mol % and 15.8 mol%, respectively (this value for the previously investigated K_2O containing flux was 18 mol%). These results correspond well to those obtained from the thermal analytical measurements. In this way the LN phase boundaries estimated by using the DTA results were verified and refined by the crystal growth experiments.

Since Na enters the lattice the properties of the crystal grown from Na_2O-based flux are quite different (e.g higher phase transition temperatures). For this crystal, the [Li]/[Nb] ratio varies both in the liquid and solid phases because of the incorporation of Na ions into the lattice as a dopant. The alkali content of the liquid at the limit concentration of the crystallization of the LN phase may be estimated by assuming a constant effective segregation coefficient k ~ 0.2 for Na_2O. Thus, from the yield of the pulled amount of LN phase both the whole amount of the incorporated sodium oxide and the alkali content of the liquid can be calculated.

With this method for the limit concentration of Na_2O in the liquid we obtained around 14.1mol%. Results of the atomic absorption spectroscopy on the alkali content of the residues obtained after pulling out the maximum amount of LN single phase support the above estimates on the limit concentrations for these solvents.

3.2.2. Solid composition determination by UV/Vis spectroscopic measurements

The Li_2O content of the slices of the $LiNbO_3$ crystals grown from the different alkali metal oxide (Na_2O, Rb_2O and Cs_2O) containing fluxes [53] was determined using a Jasco V-550 UV/VIS spectrometer [38]. 2 mm thick z-slices were cut along the growth axes and polished for the spectroscopic experiments (see Fig. 3.9).

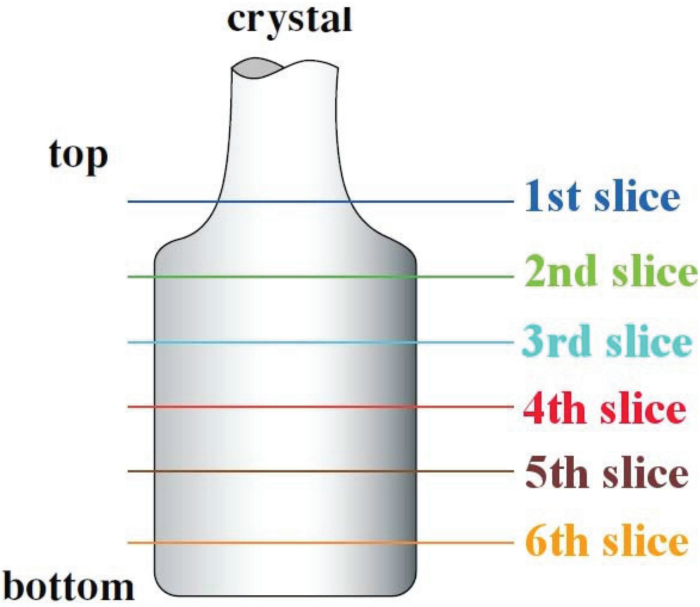

Figure 3.9. Schematic diagram of crystal cut

UV edge measurements were carried out at room temperature on the z cut slices.

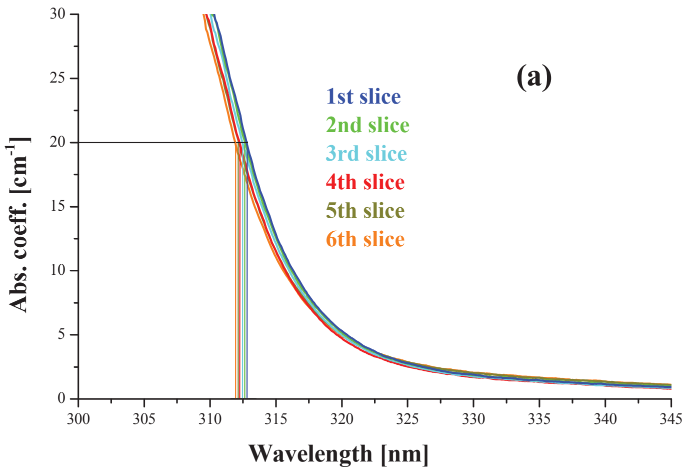

(a)
1st slice
2nd slice
3rd slice
4th slice
5th slice
6th slice
Abs. coeff. [cm^{-1}]
0
5
10
15
20
25
30
300
305
310
315
320
325
330
335
340
345
Wavelength [nm]

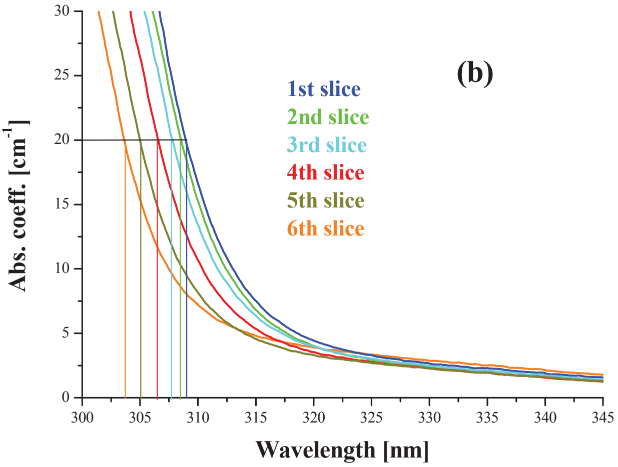

(b)
1st slice
2nd slice
3rd slice
4th slice
5th slice
6th slice
Abs. coeff. [cm^{-1}]
0
5
10
15
20
25
30
300
305
310
315
320
325
330
335
340
345
Wavelength [nm]

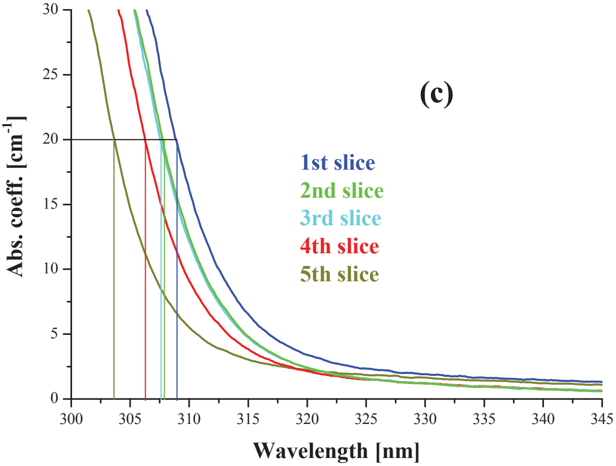

Figure 3.10. UV absorption spectra of the different parts of the crystals grown from different alkali metal containing fluxes (a) – Na, (b) – Rb and (c) – Cs

In each case, the wavelength value where the absorption coefficient reaches 20 cm^{-1} was determined. For all examined sample series this edge position was shifting to shorter wavelengths from the top to the end of the crystals (Fig. 3.10.). The evolution of the edge position as a function of the yield of the LN phase obtained from Rb_2O- and Cs_2O- containing flux is similar, while for crystals grown from K_2O-based flux it starts decreasing from a shorter wavelength and becomes constant above a given yield (~35 wt%). The UV-edge position for the crystal grown from Na_2O-containing flux differs remarkably: it starts at higher wavelength and shows only a slight change (Fig. 3.11).

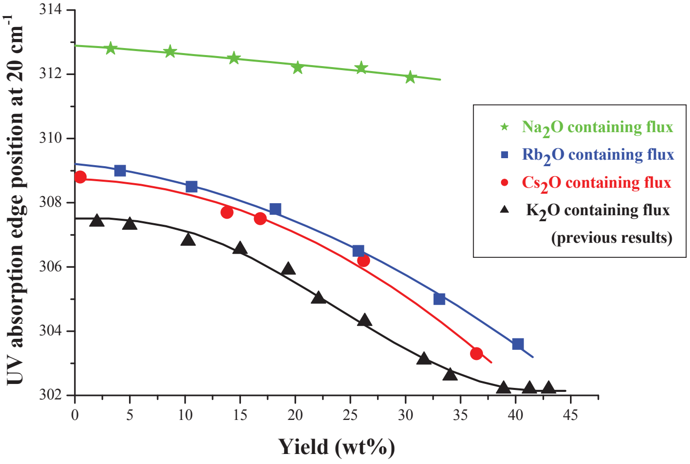

Figure 3.11. Measured UV edge positions as a function of the yield (the yield is given in weight % because this is the only way for comparison of the properties of the Na-doped crystal with the pure LN crystals)

Table 3.3 contains the wavelength values at $\alpha = 20$ cm^{-1} and the calculated compositions. The composition calculation is based on the previous calibration - described in chapter 1.5 - between the UV absorption edge position and the Li_2O content of the crystal [38].

Since Rb and Cs ions do not enter the lattice, the [Li]/[Nb] ratio of the pure $LiNbO_3$ crystals can be determined from the UV absorption edge position measured. However, the Na ions were incorporated into the crystal (at the Li sites as it will be shown in chapter 3.3.2.3.) therefore the calibration mentioned above is inappropriate for the determination of the Li_2O concentration, but it is assumed to give acceptable results for the total alkali oxide ($Na_2O + Li_2O$) content.

Table 3.3. UV absorption edge positions and the calculated compositions of the different parts of the crystals. * For the crystal grown from Na_2O containing flux the Li_2O or the [Li] value means the [Li_2O + Na_2O] content in all cases.

Alkali ion in the flux	N° of the slice	Yield at the slice [wt%]	Abs. coeff. at 20 cm^{-1}	Li_2O content of the slice [mol%]	[Li]/[Nb] ratio of the slice
Na	1	3.25	312.8	49.38*	0.9755*
	2	8.66	312.7	49.39*	0.9759*
	3	14.45	312.5	49.42*	0.9771*
	4	20.24	312.2	49.45*	0.9782*
	5	26.00	312.2	49.45*	0.9782*
	6	30.43	311.9	49.48*	0.9794*
K	**1**	**2.00**	**307.4**	**49.82**	**0.9928**
	2	**5.00**	**307.3**	**49.83**	**0.9932**
	3	**10.28**	**306.8**	**49.86**	**0.9944**
	4	**15.00**	**306.6**	**49.87**	**0.9948**
	5	**19.38**	**305.9**	**49.90**	**0.9960**
	6	**22.12**	**305.0**	**49.94**	**0.9976**
	7	**26.30**	**304.3**	**49.96**	**0.9984**
	8	**31.68**	**303.1**	**49.98**	**0.9992**
	9	**34.06**	**302.6**	**49.99**	**0.9996**
	10	**38.90**	**302.2**	**49.99**	**0.9996**
	11	**41.26**	**302.2**	**49.99**	**0.9996**
	12	**43.00**	**302.2**	**49.99**	**0.9996**
Rb	1	4.12	309.0	49.72	0.9889
	2	10.60	308.5	49.76	0.9904
	3	18.21	307.8	49.80	0.9920
	4	25.74	306.5	49.87	0.9948
	5	33.07	305.0	49.94	0.9976
	6	38.03	303.6	49.98	0.9992
Cs	1	0.50	308.8	49.74	0.9897
	2	13.81	307.7	49.81	0.9924
	3	16.84	307.5	49.82	0.9928
	4	26.21	306.2	49.89	0.9956
	5	36.46	303.3	49.98	0.9992

For the most stoichiometric part of the Rb-LN and Cs-LN crystals the [Li]/[Nb] ratio was calculated to be 0.9992 (49.98 mol% Li_2O). The [Li]/[Nb] ratio closest to 1 was obtained for the *K-LN* crystal with a measured absorption edge of about 302.2 nm corresponding to [Li]/[Nb] ~ 0.9996 (49.99 mol% Li_2O).

The composition of the samples (grown from 10 mol% Rb or Cs containing fluxes) changed between 49.72 – 49.98 mol% Li_2O content, the typical range what is called "nearly stoichiometric". Though the [Li]/[Nb] ratio of the melts was changing during growth from 1 to 1.002, 1.005 and 1.004 for K, Rb and Cs, respectively, these changes could be neglected in the analysis.

The data of Table 3.4 are represented in Fig. 3.12.

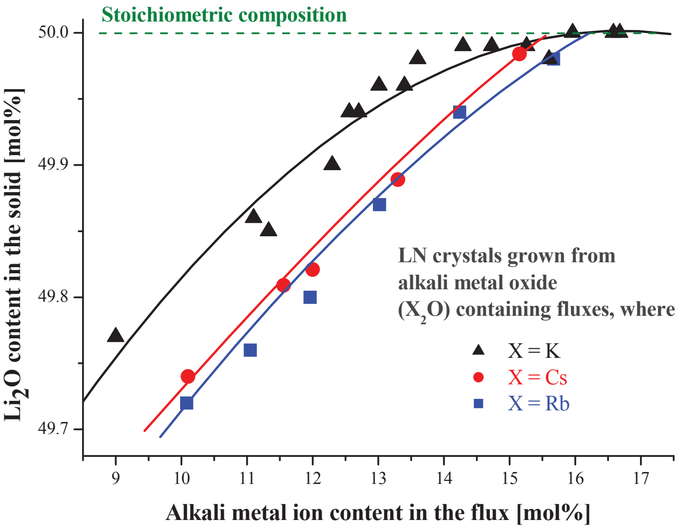

Figure 3.12. Comparison of the Li_2O content in the solid as a function of the alkali metal ion content in the flux for the crystals grown from Rb_2O and Cs_2O with the crystal grown from K_2O containing fluxes ([Li] / [Nb]= 1 in all cases)

3.2.3. Phase relations along the vertical section of $LiNbO_3$-X_2O systems

With the method described in chapter 2 we can determine tie-lines (corresponding compositions of the liquidus and solidus at a given temperature) of the ternary phase diagram along the vertical section of $LiNbO_3$-X_2O by the combination of the results of the thermal analytical, X-ray, crystal growth and spectroscopic measurements. Table 3.4 and Fig. 3.13 summarize the data gained for our nearly sLN crystals grown from Rb_2O or Cs_2O containing fluxes.

Table 3.4. The data correspond to the composition of liquid and solid phases in equilibrium at the given temperature

X	X_2O content of the flux [mol%]	Li_2O content of the crystal [mol%]	Crystallization temperature [°C]
Rb	10.08	49.72	1185
	11.05	49.76	1179
	11.96	49.8	1171
	13.02	49.87	1150
	14.24	49.94	1125
	15.67	49.98	1091
Cs	10.10	49.74	1185
	11.56	49.81	1179
	12.00	49.82	1163
	13.30	49.89	1143
	15.15	49.98	1079

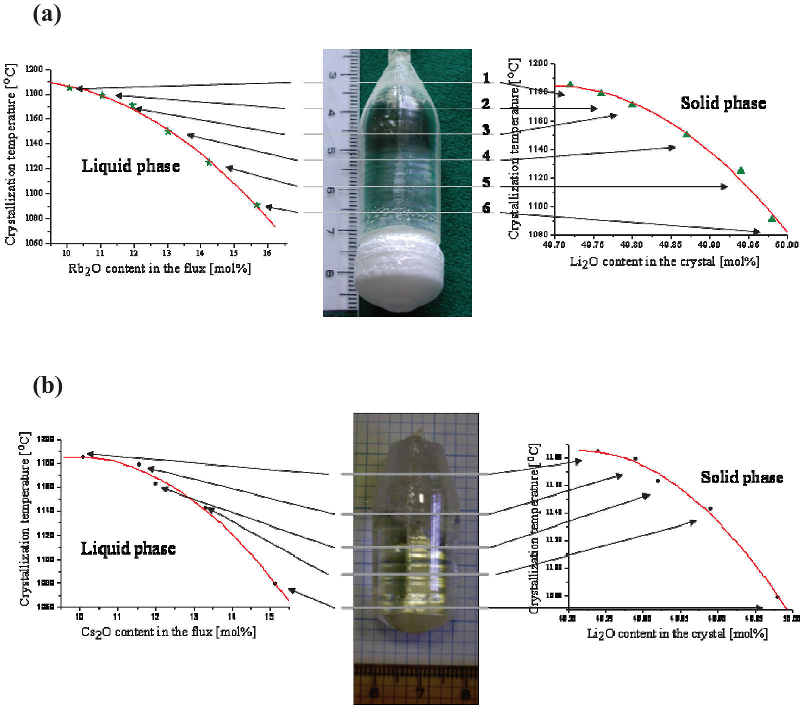

Figure 3.13. The dependence of the stoichiometry (crystallization temperature) of the crystals grown from Rb_2O (a) and Cs_2O (b) containing fluxes on the actual flux composition. The red curves show the evolution of the crystallization process.

As it was established before, the key parameter for the composition of the solution grown $LiNbO_3$ is the crystallization temperature. Consequently the shape of the solidus curves must be the same for all ideal solvents as it is demonstrated by Table 3.4 and Fig. 3.13. (We note that the accuracy of temperature reading in this case is about ± 5 °C.)

3.3. Spectroscopic characterization and composition determination of the crystals grown from alkali metal oxide fluxes

3.3.1. IR absorption measurements

3.3.1.1. OH⁻ vibrational spectra of crystals grown from Rb_2O and Cs_2O containing fluxes

As it is shown in chapter 1.5 the intensity ratio of the two principal OH^- vibrational peaks of the nearly stoichiometric $LiNbO_3$ crystal can be suitable for determining the composition of the crystal.

The IR spectra – of the LN crystals grown from different alkali metal oxide containing solvents – were recorded at room temperature by an FTIR spectrometer with a resolution of 0.5 cm^{-1} immediately after crystal growth (Fig. 3.14). The composition of the samples was in the 49.7 – 50.0 mol% Li_2O range (according to the UV absorption measurements).

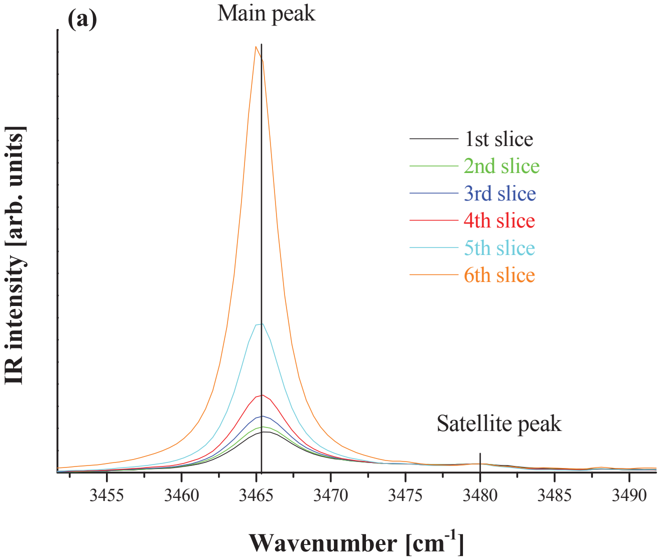

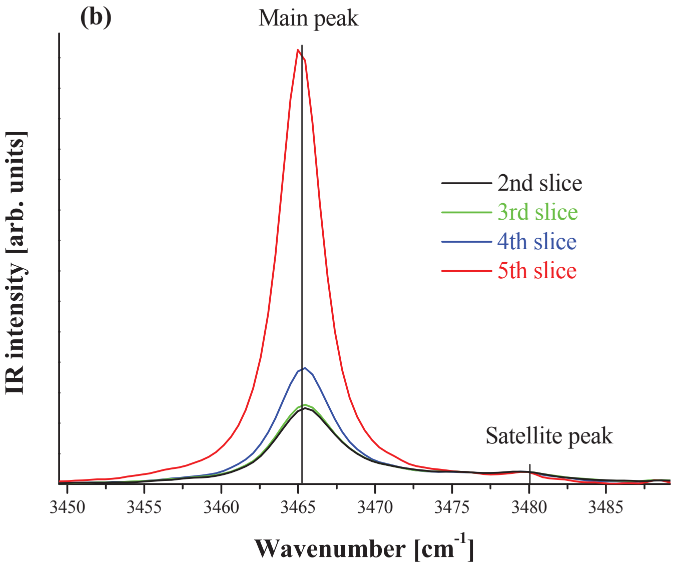

Fig. 3.14. OH$^-$ absorption spectra of consecutive slices of the LN crystals grown from Rb_2O (a) and Cs_2O (b) containing fluxes measured 2 weeks after the growth

The spectra were normalized to the 3480 cm^{-1} satellite band. It is clearly seen that the higher the Li_2O content of the crystal, the higher the intensity of the 3465 cm^{-1} main line, i.e. the intensity ratio $R = I_{3480} / I_{3465}$ of the two components decreases with increasing Li_2O content. Although the R value seems to be usable for the determination of the crystal composition, one has to take into account the dependence of the spectral changes on temperature and time [54].

For the observation and characterization of this phenomenon a long term systematic investigation was conducted. The IR spectra of the samples were also recorded 7.5, 16, 18, and 20 months after the crystal growth. Between the measurements the samples were kept at room temperature.

Figure 3.15 shows the time dependence of the OH$^-$ absorption spectra. For the sake of simplicity one characteristic slice was chosen from each crystal. It is clearly seen on the normalized spectra that the intensity of the main line decreases monotonously with increasing time.

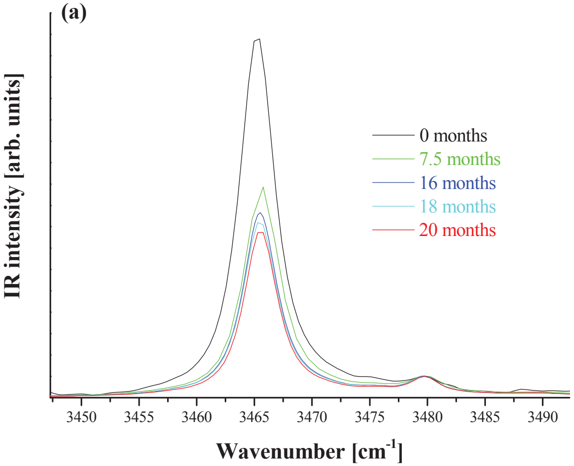

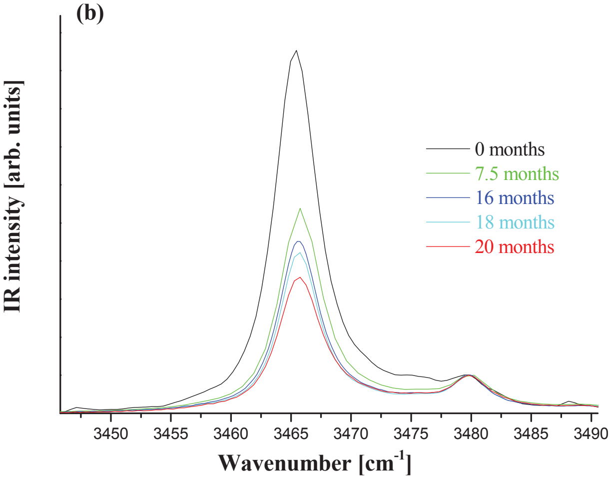

Fig. 3.15. Time dependence of the OH^- absorption spectra of the 5th and 4th slices of the LN crystals grown from Rb_2O (a) and Cs_2O (b) containing fluxes, respectively

The accuracy of the absorbance measurements was better than 0.001, which results in $R = I_{3480} / I_{3465}$ values more accurate than 0.01 even for weak OH^- signals and taking into account the background uncertainty of the spectra.

The intensity ratio of the two bands (R, or 1 / R, Table 3.5) has been calculated applying background correction (the figures show background-corrected spectra) and reading the absorbance maxima near 3465 and 3480 cm^{-1}.

Table 3.5. Calculated 1/R values from the IR absorption spectra for all the slices measured 0, 7.5, 16, 18 and 20 months after the crystal growth

Alkali ion in the flux	**N° of the slice**	**Li_2O content of the slice [mol%]**	**Intensity ratios of the IR bands, $1/R = I_{3465}/I_{3480}$**				
			0	**7.5**	**16**	**18**	**20**
			months after the growth				
Rb	1	49.72	4.69	2.17	1.87	1.82	1.79
	2	49.76	5.17	2.47	2.12	2.07	2.08
	3	49.8	6.37	3.19	2.68	2.66	2.5
	4	49.87	8.76	4.65	4.05	3.81	3.85
	5	49.94	16.79	9.86	8.24	8.2	7.73
	6	49.98	48.13	36.09	36.92	35.59	34.2
Cs	2	49.81	6.24	3.24	2.7	2.73	2.7
	3	49.82	6.51	3.46	3.05	2.93	2.83
	4	49.89	9.53	5.39	4.48	4.3	4.22
	5	49.98	35.65	22.84	21.35	19.61	18.96

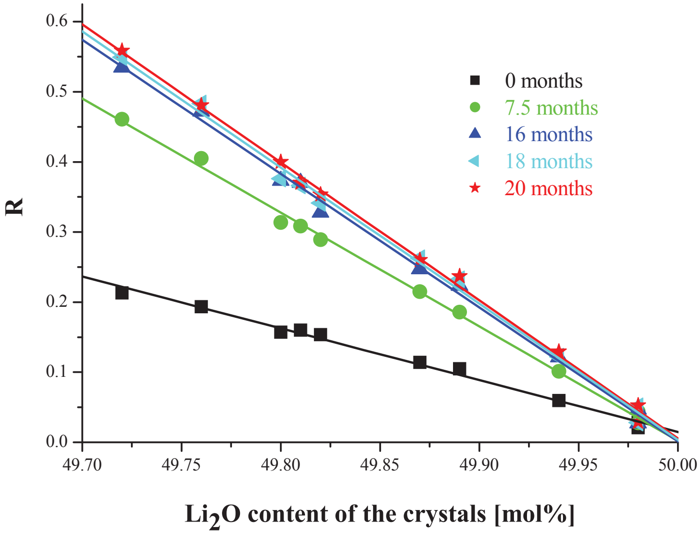

Figure 3.16. R as a function of time for all measured LN slices. The error bars in R are in the range of the symbol size [55]

The R values were plotted as a function of the crystal composition (Fig. 3.16) for different times passed after the crystal growth. We obtained straight lines with different slopes (S). The change of R as a function of time is related to the redistribution of hydroxyl ions among the different defect sites (approaching their room temperature equilibrium).

The phenomenon can be formulated by a general equation:

$$R(t) = S(t) \times (C - [Li_2O]), \tag{3.1}$$

where $[Li_2O]$ is the lithium oxide concentration of the crystal in mol%. Using least square fits the parameter C was always equal to 50 with an accuracy of < 0.005 mol%. This result has been expected, since at the stoichiometric composition, at $[Li_2O] = 50$ mol%, the OH^- defects appearing at 3480 cm^{-1} due to non-stoichiometry should disappear (R = 0).

Equation (3.1) provides an easy and fast determination of the sample composition at 0, 7.5, 16, 18, and 20 months after crystal growth. The relative accuracy of the present method in the [Li_2O] = 49.7 – 50.0 mol% composition range is about 0.01 mol%, similarly to the UV edge method. The fact that R takes the 0 value exactly at 50 mol% in all cases proves that the absolute accuracy is also in the range of 0.01 mol%. A posteriori this also confirms that the UV absorption edge method on its turn, used for the composition determination of the samples, has an absolute accuracy of at least 0.01 mol% in this region. Earlier this was assumed to be only at about 0.1 mol% and the composition calibration, in the absence of a 'zero-parameter' like R, was only based on the less precise Curie-temperature measurements [23].

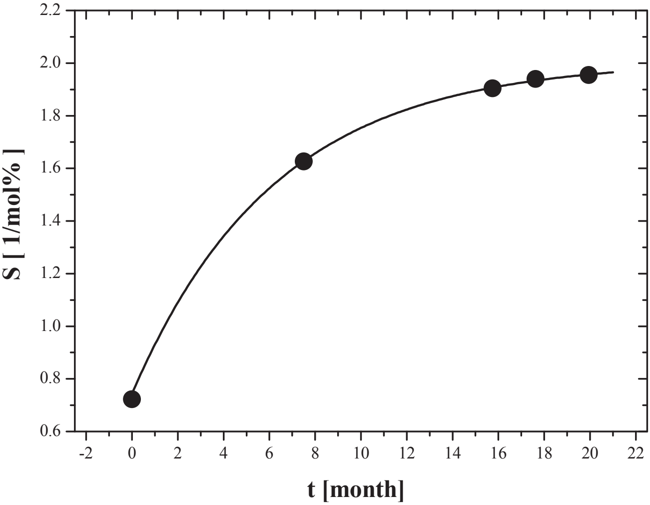

Fig. 3.17. The slope of the calibration lines as a function of time passed after crystal growth. The continuous line corresponds to the best fit using equation (3.2)

Figure 3.17 shows the time dependence of the slopes of the calibration lines. The obtained values fit well to a first order exponential curve

$$S(t) = S_{\infty} - A \times \exp(-t/\tau), \tag{3.2}$$

where S_∞ represents the slope of the calibration line at $t = \infty$ (i.e. in thermal equilibrium at room temperature, which in our case was 22 ± 2 ˚C), and τ is the time constant of the thermally induced change of the OH^- bands ($S_\infty = 2.01 \pm 0.02$ [1/mol%], $A = 1.27 \pm 0.02$ [1/mol%], $\tau = 6.2 \pm 0.3$ months). Equations (3.1) and (3.2) allow us to determine the Li_2O content of the crystal kept at room temperature for any time after the growth. Although τ depends on the exact value of room temperature, the accuracy of $[Li_2O]$ is better than 0.01 for ± 1 ˚C and about 0.02 for ± 2 ˚C temperature uncertainties.

The redistribution rate of hydroxyl defects can be accelerated by heating the $LiNbO_3$ crystals to higher temperatures [54]. The thermal equilibrium state of the OH^- defects is different at different temperatures. After heating the crystal up to 1000 °C and then cooling back to room temperature it returns to its initial state measured immediately after the growth.

Two slices were chosen for investigating the temperature dependence of the redistribution rate of OH^- defects. These samples were the 2nd and the 4th slices of the crystal grown from Rb_2O containing flux with 49.76 and 49.87 mol% Li_2O content, respectively. The heating and cooling rates applied were about 300 °C/hour which is about 3 times faster than the cooling rate used after crystal growth. Partial recovery was reached by heat treatments at intermediate temperatures (at 100 °C, 250 °C, or 500 °C for 10 – 30 minutes, see Fig. 3.18), with the R values approaching but not reaching those obtained after crystal growth at the $t = 0$ moment.

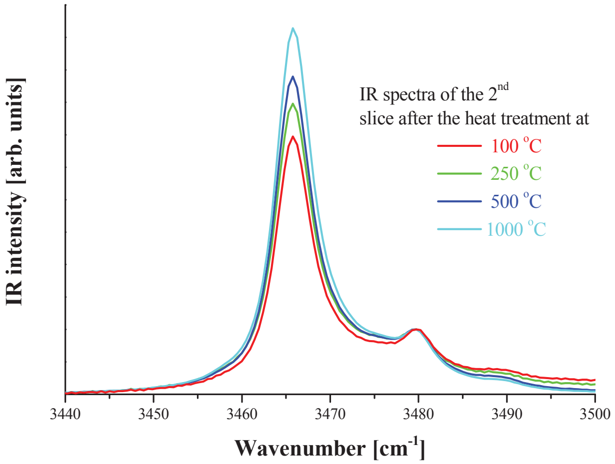
IR intensity [arb. units]
IR spectra of the 2nd slice after the heat treatment at
100 °C
250 °C
500 °C
1000 °C
3440
3450
3460
3470
3480
3490
3500
Wavenumber [cm-1]

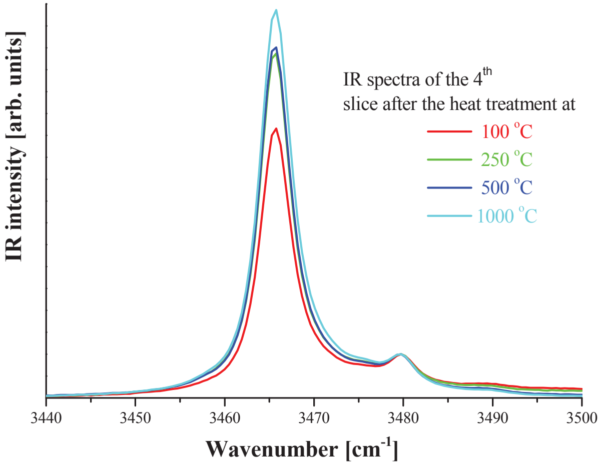
IR intensity [arb. units]
IR spectra of the 4th slice after the heat treatment at
100 °C
250 °C
500 °C
1000 °C
3440
3450
3460
3470
3480
3490
3500
Wavenumber [cm-1]

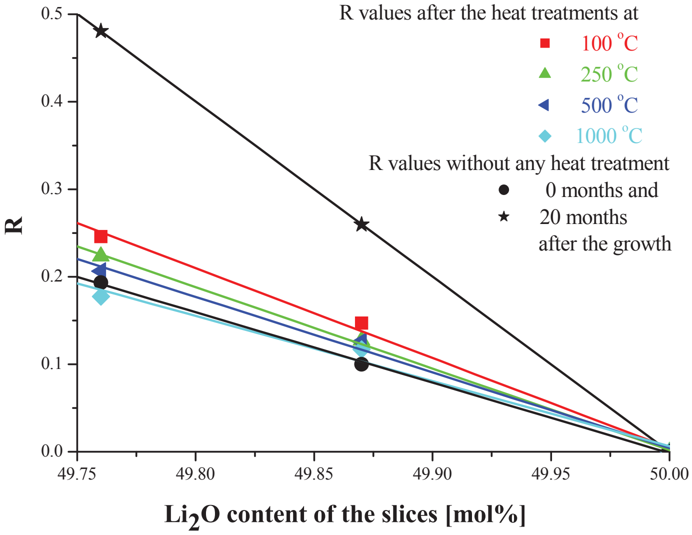

Figure 3.18. IR spectra and the change of the calculated R as a function of the annealing temperature for two selected LN slices.

After annealing at 1000 °C the ratio of the peaks returned to their original value measured just after the crystal growth. The OH^- spectra of these two slices were then re-measured after 4, 11, 21, 37, and 72 days (Fig. 3.19).

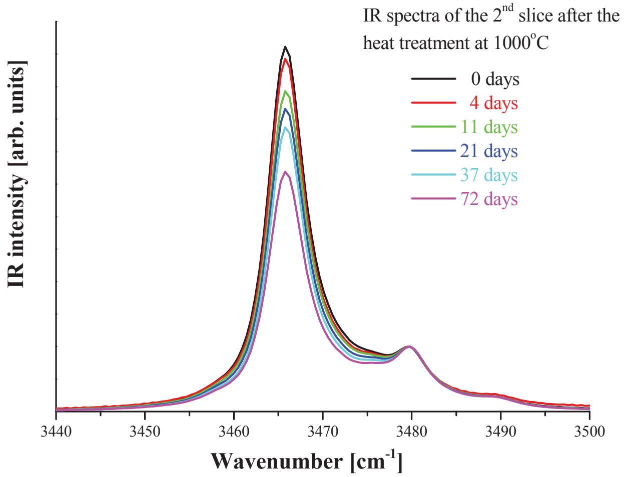
IR spectra of the 2nd slice after the heat treatment at 1000°C
0 days
4 days
11 days
21 days
37 days
72 days
IR intensity [arb. units]
3440
3450
3460
3470
3480
3490
3500
Wavenumber [cm-1]

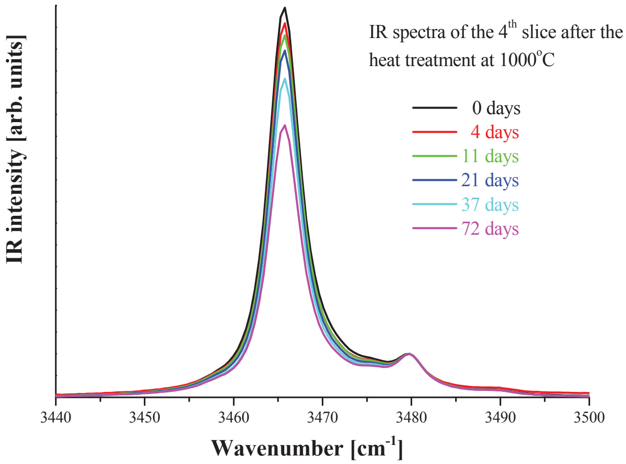
IR spectra of the 4th slice after the heat treatment at 1000°C
0 days
4 days
11 days
21 days
37 days
72 days
IR intensity [arb. units]
3440
3450
3460
3470
3480
3490
3500
Wavenumber [cm-1]

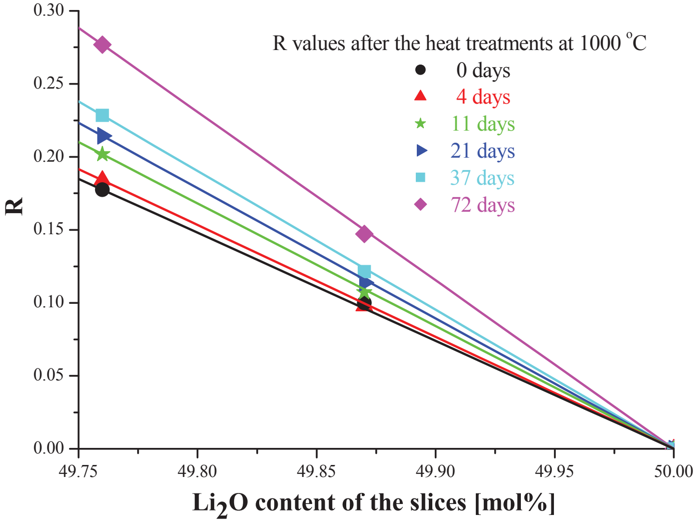

Figure 3.19. IR spectra and the change of R as a function of time passed after the heat treatment at 1000 °C for two selected LN slices

The slopes obtained after the 1000°C heat treatment with 4, 11, 21, 37, and 72 days perfectly fit the line calculated by equation (3.2) using the parameter values given above (see empty circles in Fig. 3.20). This means that the crystal indeed returned to its initial state after the heat treatment at 1000 °C.

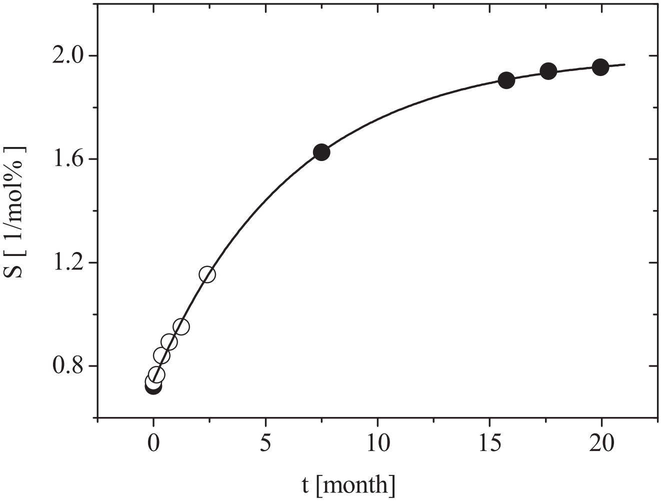

Figure 3.20. The slope of the calibration lines as a function of time passed after crystal growth (full circles) after a heat treatment at 1000 °C (empty circles). The continuous line corresponds to the best fit using equation (3.2) [55]

The method of determination of the crystal composition from the OH^- spectra has been tested by measuring the intensity ratio of the two peaks of 5 different nearly stoichiometric samples kept at room temperature for several years (thermally equilibrated samples). The [Li_2O] content of the crystals was found to be between 49.6 – 49.9 mol% based on the calibration by the UV absorption edge method (Fig.3.21). Their Li_2O content was also determined using equation (3.1) and was compared to those obtained from the UV absorption edge calibration (Table 3.6).

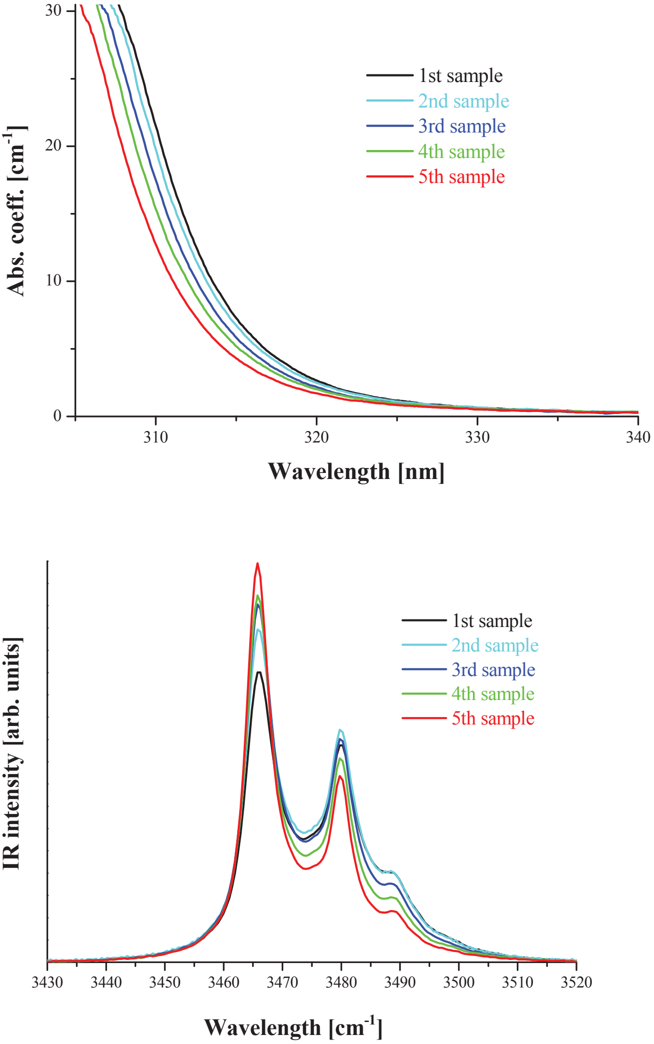

Figure 3.21. UV absorption and OH^- vibration spectra of a series of 5 different nearly stoichiometric LN samples in thermal equilibrium

Table 3.6. Sample compositions obtained by two different calibration methods

N°. of the sample	**UV measurements**		**IR measurements**	
	Abs. edge position at 20 cm^{-1}	**Corresponding Li_2O content [mol%]**	**R**	**Corresponding Li_2O content [mol%]**
1	310.3	49.62	0.7481	49.63
2	309.9	49.65	0.6984	49.65
3	309.3	49.7	0.6238	49.69
4	308.7	49.73	0.5559	49.72
5	307.9	49.78	0.4669	49.77

The difference between the two values was smaller than or equal to 0.01 mol% proving that the accuracy of the OH^- band method allows us to determine the Li_2O content of the samples with an accuracy of about 0.01 mol%. The peak at 3488 cm^{-1} is more intensive in these spectra (Fig. 3.21) than it was observed with the samples used for the calibration which can be explained by the less Li_2O content of these crystals.

The compositions of two samples out of five in the table were in the range of 49.6 - 49.7 mol% which is far from the stoichiometric composition therefore it seems plausible to assume that our calibration can be extended towards the lower Li content up to the merging of the two distinct peaks in the spectrum.

R can easily be measured on samples in a wide thickness range of about 0.5 – 10 mm (below 0.5 mm the intensity of the 3480 cm^{-1} band is too weak, while above 10 mm the intensity of the 3465 cm^{-1} band is too high to be accurately measured) which is an advantage against the calibration based on the UV-edge position. The latter method can optimally be used only for 1 – 3 mm thick samples as described in Ref. [38].

The method described above is based on the measurements of undoped crystals. So it can be used for the determination the Li_2O content of any other undoped LN samples falling into the indicated composition range after appropriate heat treatment.

3.3.1.2. OH⁻ spectra of crystals grown from Na_2O containing flux

For the crystal grown from Na_2O containing flux the OH^- spectra were found remarkably different due to the incorporation of Na ions. The UV absorption edge position was at 312 – 313 cm^{-1} corresponding to about 49.38 – 49.48 mol% alkali oxide content ($[Li_2O]$ + $[Na_2O]$, see also Table 3.3), which is rather far from the stoichiometric composition. In the IR spectra only one wide, asymmetric band was found at about 3473 cm^{-1} which can be attributed to various kinds of Na-OH defects [56] (Fig. 3.22).

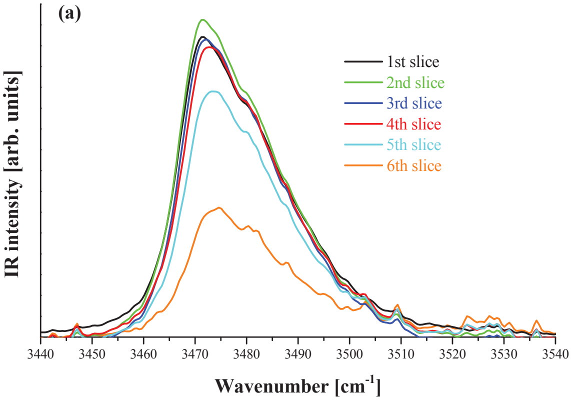

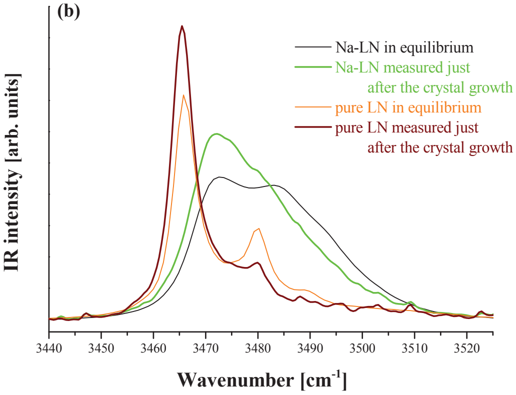

Figure 3.22. IR absorption spectra of the different slices of the Na-LN crystal (a) and time dependence of the 3rd slice compared with that of stoichiometric LN (3rd slice of the Rb-LN crystal) (b)

Time dependence can also be observed for the spectra of the Na-LN crystal. The intensity of the peak at 3473 cm^{-1} decreases while a new peak at 3483 cm^{-1} appears. The two peaks that could have been applied for the calibration of the composition are not present in this case.

3.3.2. Raman spectroscopic properties of the crystals

3.3.2.1. Composition calibration for lithium niobate crystals based on Raman experiments

As it was shown in chapter 1.5 composition calibrations of lithium niobate crystals based on the full width at half maximum (FWHM) measurements of the E(TO1) Raman mode cannot be directly compared. The main reason of this phenomenon is the overlap of the Lorentzian-shaped Raman band and the apparatus function. The apparatus function expresses the apparent broadening of a signal due to the experimental limitations. It is determined, for example, by the quality (sharpness) of the laser excitation, the spectral analysis (e.g. widths of internal slits, focal length, number of grooves per millimetre at the grating), the technical resolution of the detector, and other features of the optical pathway (quality of adjustment, confocality, etc.) [57]. The half-width of the apparatus function is often reported as the spectral resolution of the measurement. To deduce the real FWHM of a Raman band, its measured FWHM has to be corrected for the apparatus function. Assuming the apparatus function to have a Gaussian shape, band-width correction can be done by deconvolution. Assuming a triangularly shaped apparatus function a simplified equation can be derived [57]:

$$\Delta\nu = \Delta\nu_{meas}\sqrt{1-2\left(\frac{s}{\Delta\nu_{meas}}\right)^{2}} \tag{3.3}$$

where $\Delta\nu$ is the real FWHM, $\Delta\nu_{meas}$ is the measured FWHM and s is the spectral resolution of the respective Raman system. This mathematical correction yields reliable real FWHMs only if $\Delta\nu \geq 2s$. It has to be mentioned that for broad bands ($\Delta\nu >> s$) the correction can be neglected. For the relatively narrow lines, especially in nearly stoichiometric $LiNbO_3$ crystals, the correction is necessary, as shown below.

E(TO1) Raman modes at 152 cm^{-1} of undoped lithium niobate crystal slices with different Li_2O contents (48.60 – 49.99 mol%, determined by the UV absorption edge position method, see chapter 1.5) were measured in z(xy)z geometry with He-Ne laser excitation (633 nm) and the FWHM of this peak was determined by fitting with a Lorentzian function. The instrumental function (s) for this apparatus was determined by measuring the FWHM of the Rayleigh line and was found to be about 3 cm^{-1}. Figure

3.23 shows the measured and the corrected (determined by equation 3.3) halfwidths for the different samples.

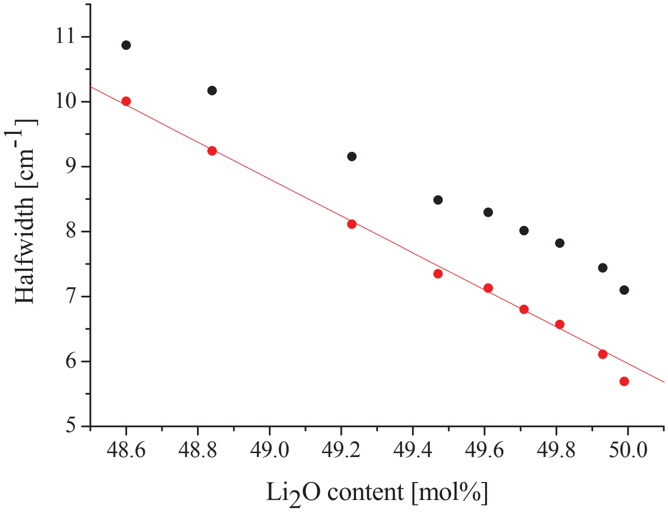

Fig. 3.23. FWHMs of the E(TO1) Raman mode of lithium niobate crystal samples with different Li$_2$O content (black circles are the Δv_{meas} values while the red ones are the corrected FWHMs (Δv))

The bandwidth of the E(TO1) mode changes unambiguously with the stoichiometry of the samples. The highest FWHMs correspond to the less stoichiometric samples. The real FWHMs are about 1 cm^{-1} below the measured values. The corrected points can be fitted well with a linear function except the last one corresponding to a Li$_2$O content higher than 49.9 mol%. This function can be described by FWHM [cm^{-1}] = 148 - 2.84·(Li$_2$O content [mol%]). Above 49.9 mol% Li$_2$O content the deviation from the linear function can be explained by the inaccuracy of the correction ($\Delta v \leq 2s$).

3.3.2.2. Raman spectra of crystals grown from Rb_2O and Cs_2O containing fluxes

Raman measurements were carried out by a micro Raman spectrometer using 633 nm He-Ne and 514.5 nm Ar-ion laser sources, with a spatial resolution of about 1 µm. The Raman spectra of y and z cut samples of the crystals were measured in different polarization configurations. Fig. 3.24 shows only those spectra which contain the E(TO) modes measured with the two different excitations.

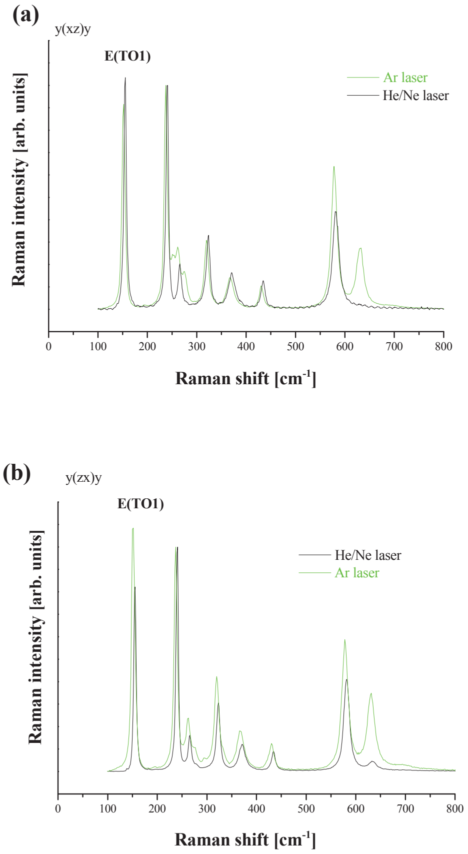

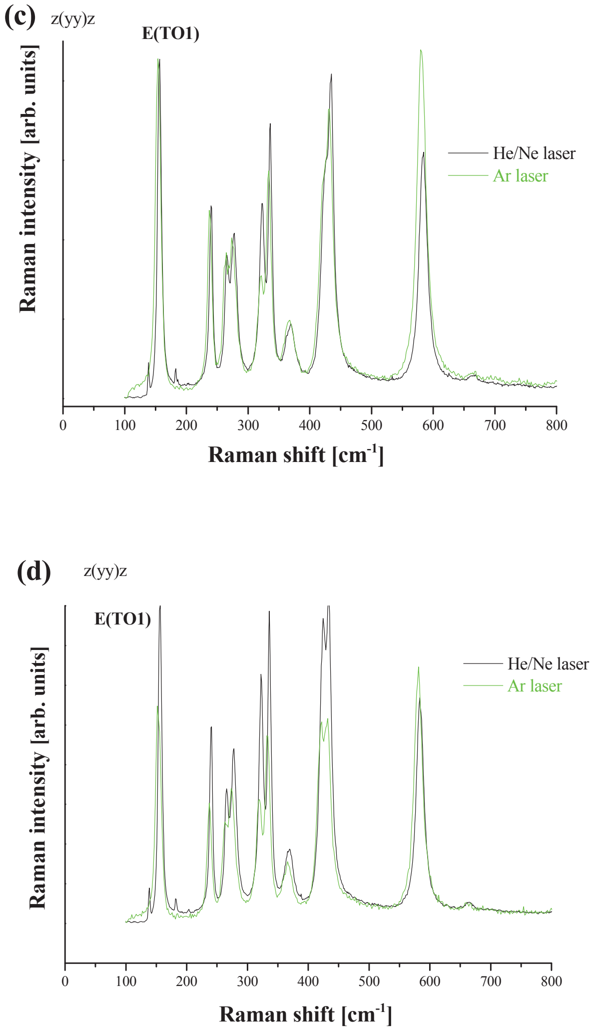

Figure 3.24. E(TO1) modes measured with different excitations in different configurations y(xz)y (a), y(zx)y (b), z(yy)z (c, d) (the slices were y cut of Rb-LN (a, b), the 1st slice (c) and the 5th slice (d) of Cs-LN)

In the configurations presented in Fig. 3.24 c, d the A_1(LO) longitudinal modes also appear beside the 9 E(TO) transversal modes. The spectra excited by the two different lasers are essentially similar, but slight differences occur in both the relative band intensities and the FWHMs. The spectra were recorded for 5 different compositions. Fig. 3.25 shows that the FWHM of the E(TO1) mode decreases with increasing Li_2O content of the samples (Table 3.3). The halfwidth values listed in Table 3.7 were obtained fitting the spectra by using Lorentzian functions. The observed differences depend not only on the exciting wavelength but on the polarization configuration as reported in chapter 1.5.

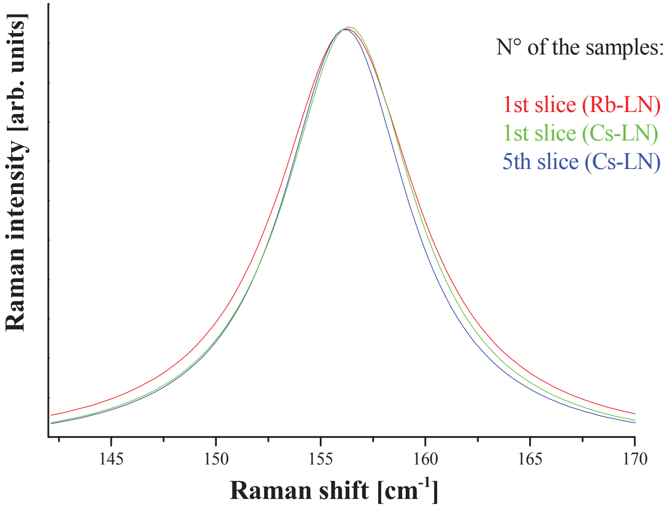

Figure 3.25. Normalized spectra of the E(TO1) modes for different compositions measured by He-Ne laser in z(yy)z configuration

Table 3.7. Measured (uncorrected) FWHMs of the E(TO1) modes in different polarizations and with different lasers. The y slices were cut from the parts of the crystals between the 2nd and 3rd slice (Rb-LN) and between the 3rd and 4th slice (Cs-LN).

Alkali ion in the flux	**N° of the slice**	**Laser**	**Configuration**	**FWHM of the E(TO1) mode [cm^{-1}]**
Rb	1	Ar	z(yy)z	9.84
Cs	1			9.58
Cs	5			9.18
Rb	1	He-Ne	z(yy)z	7.61
Cs	1			7.32
Cs	5			6.77
Rb	Y cut slice	He-Ne	y(xz)y	5.86
Cs	Y cut slice			5.72
Rb	Y cut slice	He-Ne	y(zx)y	5.39
Cs	Y cut slice			5.2

Small differences in FWHM may also come from either the compositional difference of the sample or from the surface quality. For this purpose 3 different parts of 2 selected samples (with 49.74 and 49.98 mol% Li_2O content) were measured and compared (Fig. 3.27). The spectra were also recorded on the two different surfaces (+z and –z) of the same sample. The curves strongly overlap and the differences between the FWHM values are about ± 0.15 cm^{-1}.

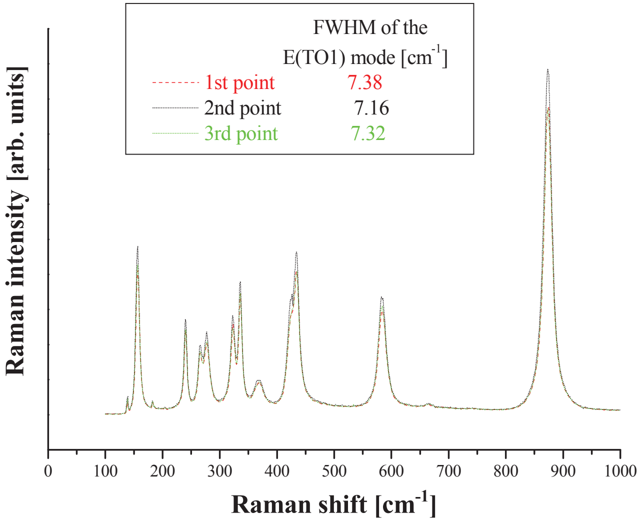

Figure 3.27. The z(yy)z Raman spectra of the 1st Cs-LN slice measured by a He-Ne laser at 3 different points

The apparatus function (*s*, see chapter 3.3.2.1.) for this Labram spectrometer was found to be about 2.2 for the He-Ne laser in z(yy)z configuration. Correction was made using equation 3.3 and the Li_2O content of the samples was calculated from the calibration line FWHM [cm^{-1}] = 148 – 2.84·(Li_2O content [mol%]). The results were compared to those obtained from the UV absorption edge method (Table. 3.8). The uncertainty of the Li_2O content calculated from the calibration based on the FWHMs of the E(TO1) mode was 0.05 mol%. This can be explained by the error of the FWHM determination (± 0.15 cm^{-1}, see above) related to the inhomogenity and the surface quality. For this apparatus (s = 2.2) the ± 0.15 cm^{-1} uncertainty of $\Delta\nu_{meas}$ causes ± 0.06 mol% uncertainty in the calculated Li_2O content in the z(yy)z configuration using a 633 nm He-Ne laser.

Table 3.8. Comparison of the Li_2O content from the two different calibration methods (Raman, UV)

Sample	**$\Delta\nu_{meas}$ [cm^{-1}]**	**$\Delta\nu$ [cm^{-1}]**	**Li_2O content calculated from the FWHMs [mol%]**	**Li_2O content from UV absorption measurements [mol%]**
Rb-1	7.61	6.94	49.67	49.72
Cs-1	7.32	6.63	49.78	49.74
Cs-5	6.77	6.01	50.00	49.98

It can be concluded that, although the FWHM of the E(TO1) Raman mode changes unambiguously with the Li_2O content of the $LiNbO_3$ crystal, for a precise composition calibration an accurate correction of the measured values is required. For this correction the apparatus function for the given laser in the given polarization must be known. Another inaccuracy of the measured FWHM comes from the surface inhomogenity and causes ± 0.06 mol% error in the calculated Li_2O content.

3.3.2.3. Raman spectra of crystals grown from Na_2O containing flux

The Raman spectra of the crystal grown from Na_2O containing solution differ from those grown from Rb_2O, Cs_2O containing solutions (Fig. 3.28). Most of the bands were shifted and broadened as compared to pure sLN indicating the presence of a high number of lattice defects induced by the incorporation of Na ions into the crystal.

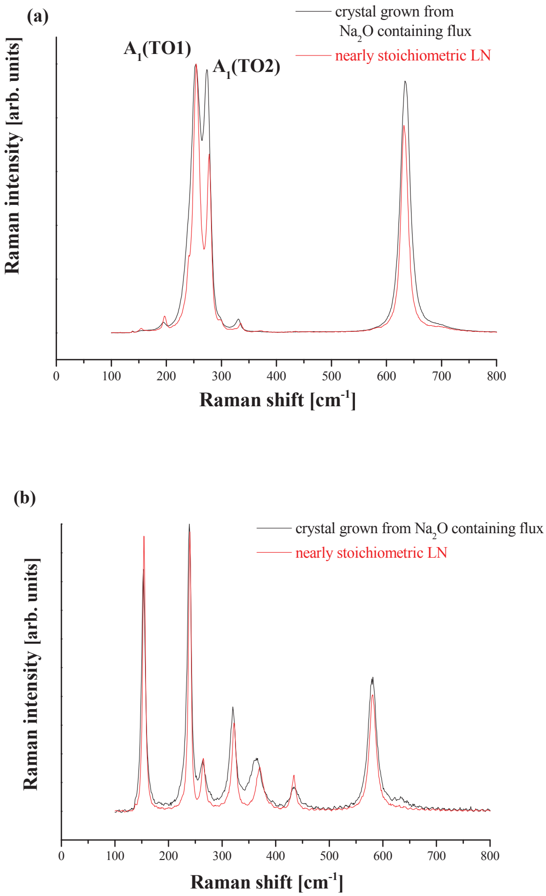

Figure 3.28. Comparison of the Raman spectra of the Na_2O containing crystal and the nearly stoichiometric LN (Li_2O content equal to 49.74 mol%) measured in y(zz)y (a) and y(xz)y (b) configurations by He-Ne (633 nm) laser

There is a remarkable difference between the spectra of the nearly stoichiometric and the Na doped crystal, namely the intensity ratio of the A_1(TO1) and A_1(TO2) modes measured in the y(zz)y configuration (Fig. 3.29).

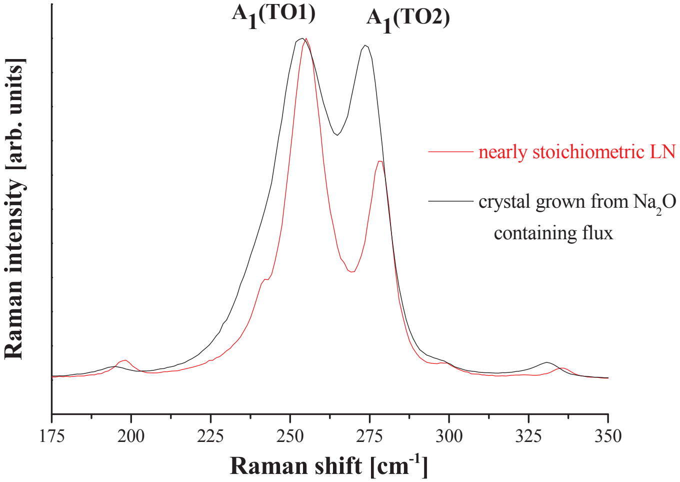

Figure 3.29. Enlarged part of figure 3.28 (a).

According to normal coordinate analysis the A_1(TO1) mode is related to Nb-O vibration, while the A_1(TO2) mode mainly involves Li-O/Nb-O motions [41]. Therefore the increase of the intensity of the A_1(TO2) mode induced by the incorporation of the Na ions into the lattice indicates that Na probably enters Li sites as it is expected from the similarities of the alkali ions.

4. Summary

We have investigated the X_2O - Li_2O - Nb_2O_5 (X = Na_2O, Rb_2O, Cs_2O) ternary systems with special emphasis on using them as flux for the growth of (nearly) stoichiometric $LiNbO_3$ single crystals by the HTTSSG (high temperature top seeded solution growth) technique. Comparison was made with the previously used K_2O - Li_2O - Nb_2O_5 ternary system. In our research program thermal analytical, x-ray phase analysis, crystal growth and several spectroscopic methods (UV, IR, Raman) were used.

Samples with different compositions were synthesized by solid state reactions, their phase transition temperatures were determined by thermal analytical methods, the formed phases were assessed by x-ray phase analysis. Phase diagrams were constructed. The consecutively crystallizing phases were separated by crystal growth, the phase identification was done by x-ray phase analysis as well. The composition of the single crystalline $LiNbO_3$ phase was determined by spectroscopic methods. The phase diagrams of the ternary systems were refined according to the gained information. The crystallization yields were calculated for each solvent. The crystals were characterized by different spectroscopic methods. A simple non-destructive spectroscopic method based on the OH^- spectra of the crystals was developed for the determination of the crystal composition.

5. New results

1. The thermal behaviour of the X_2O - Li_2O - Nb_2O_5 (X = Rb, Cs) ternary systems was found to be very similar to that of the K_2O - Li_2O - Nb_2O_5 system, with nearly the same phase transition temperatures and constituent phases according to the thermal analytical and X-ray diffraction investigations. The limit of the $LiNbO_3$ liquidus surface was estimated to be near 16 mol% X_2O for the systems with Rb_2O and Cs_2O and with [Li] / [Nb] = 1 ratio. The ternary phase diagram of the Cs_2O - Li_2O - Nb_2O_5 system at room temperature was constructed, a new phase was found.

2. It was established that crystals with $[Li_2O] / [Nb_2O_5] = 1$ can be grown from all examined ternary systems containing between 10 - 16 mol% X_2O (X = Na, Rb, Cs). Rb_2O and Cs_2O behave as ideal solvents, since they do not enter the lattice and yield (nearly) stoichiometric $LiNbO_3$ single crystals. The crystallization temperatures are nearly the same for Rb_2O and Cs_2O containing fluxes, resulting in similar [Li] / [Nb] ratios and yields of $LiNbO_3$ crystal.

3. A new method was developed for an easy and accurate determination of the Li_2O content of undoped $LiNbO_3$ crystals close to the stoichiometric composition based on the measurement of the intensity ratio (R) of the two main hydroxyl ion vibration peaks (at 3465 and 3480 cm^{-1}) in the infrared absorption spectra. The composition can be determined from the equation $R(t) = S(t) \times (C - [Li_2O])$, where $S(t) = S_\infty - A\exp(-t/\tau)$. S_∞ represents the slope of the calibration line in thermal equilibrium, $[Li_2O]$ is the lithium oxide content of the crystal in mol%, C and A are constants, τ is the time constant describing OH^- redistribution and t is the time passed after the crystal growth.

In the case of unknown thermal history (unknown *t*) of the crystal a simple annealing at 1000°C reconstructs the as grown state ($t = 0$).

4. It was confirmed that the FWHM of the E(TO1) Raman mode changes with the Li_2O content of the $LiNbO_3$ crystal but without correction these measurements cannot be used, as assumed earlier, for a universal composition determination of $LiNbO_3$. Using the FWHMs of the E(TO1) Raman modes excited by a He-Ne laser (633 nm) and corrected with the spectral resolution, a calibration line was determined for the z(xy)z configuration. The uncertainty of the calibration was determined as ± 0.06 mol% Li_2O content which may come from the uncertainty of the correction factor and the possible inhomogeneity of the sample surface.

5. Na was shown to be incorporated into the $LiNbO_3$ lattice with an average segregation coefficient of $k_{sol/liq}$ (Na_2O) ~ 0.2. Accordingly the phase transition temperatures for Na_2O containing polycrystalline samples are found to be higher than for Rb_2O or Cs_2O containing ones and their spectroscopic properties show changed behaviour: the UV absorption edge positions shift to longer wavelengths, the OH^- vibrational bands merge to only one asymmetric band and the Raman peaks also broaden and shift. According to normal coordinate analysis the A_1(TO1) mode is related to Nb-O vibration, while the A_1(TO2) mode mainly involves Li-O/Nb-O motions. Therefore the increase of the intensity of the A_1(TO2) mode induced by the incorporation of the Na ions into the lattice indicates that Na enters Li sites.

Publications

G. Dravecz, Á. Péter, K. Polgár, L. Kovács "Alkali metal oxide solvents in the growth of stoichiometric $LiNbO_3$ single crystal" Journal of Crystal Growth **286** (2006) 334-337

G. Dravecz, L. Kovács, Á. Péter, K. Polgár, P. Bourson "Raman and IR spectroscopic characterization of $LiNbO_3$ crystals grown from alkali metal oxide solvents" Phys. Stat. Sol. (c) **4** (2007) 1313-1316

G. Dravecz, L. Kovács "Determination of the crystal composition from the OH^- vibrational spectrum in lithium niobate" Appl. Phys. B **88** (2007) 305-307

G. Dravecz, B. Shackmann, M. Cochez, M. Ferriol "Investigations of new fluxes for the single-crystal growth of stoichiometric lithium niobate: study of phase relations in the ternary system of Cs_2O - Li_2O - Nb_2O_5" Journal of Thermal Analysis and Calorimetry **90** (2007) 343-345

I. Hajdara, K. Lengyel, G. Dravecz, L. Kovács, Á. Péter, Zs. Szaller "Spectroscopic methods for the determination of the composition of potassium lithium niobate crystals" Phys. Stat. Sol. (c) **4** (2007) 1321-1324

Á. Péter, I. Hajdara, K. Lengyel, G. Dravecz, L. Kovács, M. Tóth "Characterization of Potassium Lithium Niobate (KLN) Ceramic System" Journal of Alloys and Compounds **463** (2008) 398-402

I. Hajdara, K. Lengyel, L. Kovács, Á. Péter, G. Dravecz,, Zs. Szaller “Compositional dependence and structure of hydroxyl ion defects in ferroelectric potassium lithium niobate” Ferroeletrics **369** (2008) 98-107

Acknowledgements

I would like to thank my supervisor Dr. Katalin Polgár for her guidance throughout my years at the Research Institute for Solid State Physics and Optics. Without her professional support this work could not have been completed. I would also like to thank Prof. Michel Ferriol with whom the majority of work in Chapter 3.1.2 has been done during my stay at the Paul Verlaine University of Metz.

I would like to express my gratitude towards Ágnes Péter and Dr. László Kovács for the lots of explanations for understanding the thermal analytical and the spectroscopic phenomena and for having dedicated their valuable time to carefully reading the manuscript and adding their indispensable comments to it.

Thanks for the X-ray diffraction measurements to Dr. Mária Tóth and for the chemical (AAS) analysis to Dr. László Bencs.

I would also like to thank all the members of the Departments of Crystal Technology and Crystal Physics whom I had the opportunity to work with, for creating and maintaining an inspiring working and social atmosphere. In addition to those already mentioned from these groups, I would like to thank Dr. Zsuzsanna Szaller, Dr. Krisztián Lengyel and Ivett Hajdara.

Special thanks to the professors at the University of Paul Verlaine, namely Prof. Marianne Chochez, Prof. Michel Aillerie, Prof. Patrice Bourson and Prof. Marc Fontana for many helpful discussions on DTA and Raman processing and for their hospitality during my stay at France.

In particular, I would like to thank Dr. István Földvári, Head of Department and Dr. János Kollár, Institute Director for supporting and supervising.

Bibliography

[1] B. T. Matthias, J. P. Remeika "Ferroelectricity in the Ilmenite Structure" Phys. Rev. **76** (1949) 1886

[2] A. Rauber "Chemistry and physics of lithium niobate" in Current Topics in Materials Sience, Volume 1, edited by E. Kaldis, North-Holland Publishing Company, Amsterdam, New York, Oxford (1978)

[3] L. Arizmendi "Photonics applications of lithium niobate crystals" Phys. Stat. Sol. (a) **201** (2004) 253

[4] "Properties of Lithium Niobate" edited by K. K. Wong, INSPEC, The institution of Electrical Engineers, London, UK (2002)

[5] G. Malovichko, V. G. Grachev, L. P. Yurchenko, V. Ya. Proshko, E. P. Kokanyan, V. T. Gabrielyan "Improvement of $LiNbO_3$ microstructure by crystal growth with potassium" Phys. Stat. Sol. (a) **133** (1992) K29

[6] F. Abdi, M. Aillerie, P. Bourson, M. D. Fontana, K. Polgár "Electro-optic properties in pure $LiNbO_3$ crystals from the congruent to the stoichiometric composition" J. Appl. Phys. **84** (1998) 2251

[7] K. Polgár, Á. Péter, L. Kovács, G. Corradi and Zs. Szaller "Growth of stoichiometric $LiNbO_3$ single crystals by top seeded solution growth method" J. Cryst. Growth **177** (1997) 211

[8] M. Cochez, M. Ferriol, L. Pöppl, K. Polgár, Á. Péter "Ternary system Li_2O - K_2O - Nb_2O_5: Part I: Phase equilibria around the lithium niobate existence field" J. All. Comp. **386** (2005) 238

[9] K. Polgár, Á. Péter, M. Ferriol "Phase relations in the growth of stoichiometric $LiNbO_3$" Phys. Stat. Sol. (a) **201** (2004) 284

[10] Á. Péter, K. Polgár, M. Ferriol, L. Pöppl, I. Földvári, M. Cochez, Zs. Szaller "Ternary system Li_2O–K_2O–Nb_2O_5: Part II: Growth of stoichiometric lithium niobate" J. All. Comp. **386** (2005) 246

[11] R. J. Holmes, W. J. Minford "The effects of boule to boule compositional variations on the properties of $LiNbO_3$ electrooptic devices – an interpretation from defect chemistry studies" Ferroelectrics **75** (1987) 63

[12] P. K. Gallagher, H. M. O'Bryan "Effects of TiO_2 addition to $LiNbO_3$ on the cation vacancy content, Curie temperature, and lattice constants" J. Am. Ceram. Soc. **71** (1988) C56

[13] S. C. Abrahams, J. M. Reddy, J. L. Bernstein "Ferroelectric lithium niobate. 3. Single crystal X-ray diffraction study at 24°C" J. Phys. Chem. Solids **27** (1966) 997

[14] S.C. Abrahams, W. C. Hamilton, J. M. Reddy "Ferroelectric lithium niobate. 4. Single crystal neutron diffraction study at 24°C" J. Phys. Chem. Solids **27** (1966) 1013

[15] S.C. Abrahams, H. J Levinstein, J. M. Reddy "Ferroelectric lithium niobate. 5. Polycrystal X-ray diffraction study between 24° and 1200°C" J. Phys. Chem. Solids **27** (1966) 1019

[16] P. Lerner, C. Legras, J. P. Dumas "Stoechiométrie des monocristaux de métaniobate de lithium" J. Cryst. Growth **3** (1968) 231

[17] S. C. Abrahams, P. Marsh "Defect structure dependence on composition in lithium niobate" Acta Cryst. B **42** (1986) 61

[18] F. Abdi, M. D. Fontana, M. Aillerie, P. Bourson "Coexistence of Li and Nb vacancies in the defect structure of pure $LiNbO_3$ relationship to optical properties" Appl. Phys. A **83** (2006) 427

[19] A. Reisman, F. Holtzberg "Heterogeneous equilibria in the systems Li_2O - Ag_2O - Nb_2O_5 and oxide models" J. Am. Chem. Soc. **80** (1958) 6503

[20] H. M. O'Bryan, P. K. Gallagher, C. D. Brandle, "Congruent composition and Li-rich phase boundary of $LiNbO_3$" J. Am Ceram. Soc. **68** (1985) 493

[21] I. Baumann, P. Rudolph, D. Krabe, R. Schalge "Orthoscopic investigation of the axial optical and compositional homogeneity of Czochralski grown $LiNbO_3$ crystals" J. Cryst. Growth **128** (1993) 903

[22] Yu. S. Kuzminov "Opredelenie khimicheshkogo sostava kristallov niobata litiya fizicheskimi metodami" Kristallografiya **40** (1995) 1034

[23] P. F. Bordui, R. G. Norwood, D. H. Jundt, and M. M. Fejer "Preparation and characterization of off-congruent lithium niobate crystals" J. Appl. Phys. **71** (1992) 875

[24] K. Chow, H. G. McKnight, L. R. Rothrock "The congruently melting composition of $LiNbO_3$" Mat. Res. Bull. **9** (1974) 1067

[25] L. O. Svasaand, M. Eriksrud, A. P. Grande, F. Mo "Crystal growth and properties of $LiNb_3O_8$" J. Cryst. Growth **18** (1973) 179

[26] B. A. Scott, E. A. Giess, B. L. Olson, G. Burns, A. W. Smith, D. F. O'Kane "The tungsten bronze field in the system $K_2O - Li_2O - Nb_2O_5$" Mat. Res. Bull. **5** (1970) 47

[27] T. Ikeda, K. Kiyohashi "Study of subsolidus equilibria in $K_2O - Li_2O - Nb_2O_5$ system" Japan J. Appl. Phys. **9** (1970) 1541

[28] G. I. Malovichko, V. G. Grachev, V. T. Gabrielyan, E. P. Kokanyan "Widths and intensities of ESR lines of iron-group impurities in nonstoichiometric lithium niobate crystals" Sov. Phys. Solid State **28** (1986) 1453

[29] Y.S. Luh, M. M. Fejer, R.L. Byer and R.S. Feigelson "Stoichiometric $LiNbO_3$ single-crystal fibres for nonlinear optical applications" J. Cryst. Growth **85** (1987) 264

[30] K. Polgár, Á. Péter, I. Földvári "Crystal growth and stoichiometry of $LiNbO_3$ prepared by the flux method" Opt. Mat. **19** (2002) 7

[31] K. Polgár, Á. Péter, L. Pöppl, M. Ferriol, I. Földvári "Chemical and thermal conditions for the formation of stoichiometric $LiNbO_3$" J. Crystal Growth **237-239** (2002) 682

[32] K. Kitamura, J.K.Yamamoto, N. Iyi, S.Kimura, T Hayashi "Stoichiometric $LiNbO_3$ single crystal growth by double crucible Czochralski method using automatic powder supply system" J. Cryst. Growth **116** (1992) 327

[33] M. Wöhlecke, G. Corradi, and K. Betzler "Optical methods to characterise the composition and homogeneity of lithium niobate single crystals" Appl. Phys. B **63** (1996) 323

[34] J. G. Bergman, A. Ashkin, A. A. Ballman, J. M. Dziedzic, H. J. Levinstein, R. G. Smith "Curie temperature, birefringence and phase-matching temperature variations in $LiNbO_3$ as a function of melt stoichiometry" Appl. Phys. Lett. **12** (1968) 92

[35] J. R. Carruthers, G. E. Peterson, M. Grasso, P. M. Bridenbaugh "Nonstoichiometry and crystal growth of lithium niobate" J. Appl. Phys. **42** (1971) 1846

[36] U. Schlarb, K. Betzler "Refractive indices of lithium niobate as a function of temperature, wavelength, and composition: A generalized fit" Phys. Rev. **B48** (1993) 15613

[37] I. Földvári, K. Polgár, R. Voszka, R. N. Balasanyan "A simple method to determine the real composition of $LiNbO_3$ crystals" Cryst. Res. Techn. **19** (1984) 1659

[38] L. Kovács, G. Ruschhaupt, K. Polgár, G. Corradi, and M. Wöhlecke "Composition dependence of the ultraviolet absorption edge in lithium niobate" Appl. Phys. Lett. **70** (1997) 2801

[39] M. Wöhlecke, and L. Kovács "OH^- ions in oxide crystals" Crit. Revs. Sol. St. Mat. Sci. **26** (2001) 1

[40] L. Kovács, V. Szalay, R. Capelletti "Stoichiometry dependence of the OH^- absorption band in $LiNbO_3$ crystals" Sol. State Comm. **52** (1984) 1029

[41] V. Caciuc, A. V. Postnikov, G. Borstel "*Ab initio* structure and zone-center phonons in $LiNbO_3$" Phys. Rev. B **61**, No 13 (2000-I) 8806

[42] A. de Bernabé, C. Prieto, A. de Andrés "Effect of stoichiometry on the dynamic mechanical properties of $LiNbO_3$" J. Appl. Phys. **79** (1) (1995) 143

[43] G. I. Malovichko, V. G. Grachev, E. P. Kokanyan, O. F. Schrimer, K. Betzler, B. Gather, F. Jermann, S. Klauer, U. Schlarb, M. Wöhlecke "Characterization of stoichiometric $LiNbO_3$ grown from melts containing K_2O" Appl. Phys. A **56** (1993) 103

[44] N. V. Sidorov, M. N. Palatnikov, V. T. Gabrielyan, P. G. Chufyrev, V. T. Kallinikov "Raman spectra and structural perfection of nominally pure lithium niobate crystals" Inorg. Mat. **43** (1) (2007) 60

[45] I. Savova, P. Kircheva, I. Savatinova "Relaxation of Raman polarisation rules in H : $LiNbO_3$" Appl. Phys. A **80** (2005) 1117

[46] Y. Zhang, L. Guilbert, P. Bourson, K. Polgár, M. D. Fontana "Characterization of short-range heterogeneities in sub-congruent lithium niobate by micro-Raman spectroscopy" J. Phys. Cond. Mat. **18** (2006) 957

[47] A. Ridah, P. Bourson, M. D. Fontana, G. Malovichko "The composition dependence of the Raman spectrum and new assignment of the phonons in $LiNbO_3$" J. Phys. Cond. Matt. **9** (1997) 9687

[48] U. Schlarb, S. Klauer, M. Wesselmann, K. Betzler, M. Wöhlecke "Determination of the Li/Nb ratio in lithium niobate by means of birefringence and Raman measurements" Appl. Phys. A **56** (1993) 311

[49] M. Fontana, K. Chah, M. Aillerie, R. Mouras, P. Bourson "Optical damage resistance in undoped $LiNbO_3$ crystals" Opt. Mater. **16** (2001) 111

[50] R. Hammoum, M. D. Fontana, P. Bourson, V. Y. Shur "Characterization of PPLN-microstructures by means of Raman spectroscopy" Appl. Phys. A **91** (2008) 65

[51] P. Galinetto, M. Marinone, D. Grando, G. Samoggia, F. Caccavale, A. Morbiato, M. Musolino "Micro-Raman analysis on $LinbO_3$ substrates and surfaces: Compositional

homogeneity and effects of etching and polishing processes on structural properties" Opt. Las. Eng. **45** (2007) 380

[52] G. Dravecz, B. Shackmann, M. Cochez, M. Ferriol "Investigations of new fluxes for the single-crystal growth of stoichiometric lithium niobate: study of phase relations in the ternary system of Cs_2O - Li_2O - Nb_2O_5" Journal of Thermal Analysis and Calorimetry **90** n° 2 (2007) 343

[53] G. Dravecz, Á. Péter, K. Polgár, L. Kovács "Alkali metal oxide solvents in the growth of stoichiometric $LiNbO_3$ single crystal" J. Crystal Growth **286** (2006) 334

[54] K. Lengyel, L. Kovács, G. Mandula, and R. Rupp "Kinetics of OH^- ions in nearly stoichiometric $LiNbO_3$ crystals," Ferroelectrics, **257** (2001) 255

[55] G. Dravecz, L. Kovács "Determination of the crystal composition from the OH^- vibrational spectrum in lithium niobate" Appl. Phys. B **88** (2007) 305

[56] G. Dravecz, L. Kovács, Á. Péter, K. Polgár, and P. Bourson "Raman and infrared spectroscopic characterization of $LiNbO_3$ crystals grown from alkali metal oxide solvents" Phys. Stat. Sol. (c) **4** (2007) 1313

[57] L. Nasdala, M. Wenzel, G. Vavra, G. Irmer, T. Wenzel, B. Kober "Metamictisation of natural zircon: accumulation versus thermal annealing of radioactivity-induced damage" Contrib Mineral Petrol **141** (2001) 125

Appendix

A.1. Definitions

Liquidus[*]

A line on a binary phase diagram (or surface on a ternary phase diagram) that indicates the temperature at which solidification begins on cooling or at which melting is completed on heating under equilibrium conditions.

Liquidus temperature

This is the maximum temperature at which crystals can co-exist with the melt in thermodynamic equilibrium. Above the liquidus temperature the material is homogeneous. Below the liquidus temperature the crystal begins to grow.

Solidus*

A line on a binary phase diagram (or a surface on a ternary phase diagram) that indicates the temperature at which a system becomes completely solid on cooling or at which melting begins on heating under equilibrium conditions.

Solidus temperature

Below this temperature the given substance is completely crystallized. The solidus and liquidus do not align or overlap in all cases. If a gap exists between the solidus and

---

[*] IUPAC Gold Book (http://goldbook.iupac.org)

liquidus, then within that gap, the substance consists of solid and liquid phases simultaneously.

Eutectic reaction*

An isothermal, reversible reaction between two (or more) solid phases during the heating of a system, as a result of which a single liquid phase is produced.

Peritectic reaction[*]

An isothermal, reversible reaction between two phases, a liquid and a solid, that results, on cooling of a binary, ternary, ... , *n* system in one, two, ... (*n-1*) new solid phases. Synonymous with incongruent reaction.

---

[*] IUPAC Gold Book (http://goldbook.iupac.org)

A.2. List of abbreviations

LN – Lithium – meta niobate, $LiNbO_3$
  sLN – Stoichiometric lithium niobate
  cLN– Congruent lithium niobate
L3N – Lithium – ortho niobate, Li_3NbO_4
LN3 – $LiNb_3O_8$
KLN – Potassium lithium niobate, $K_3Li_2Nb_5O_{15}$
HTSG – High temperature solution growth
HTTSSG – High temperature top seeded solution growth
DSC – Differential scanning calorimetry
IR - Infrared
UV - Ultraviolet
[Z] – Concentration of Z in mol%
Liq. – Liquidus
AAS – Atomic absorption spectroscopy
FTIR Spectroscopy – Fourier-transformed infrared spectroscopy
Na-LN – Na doped lithium niobate crystal grown from a flux containing 10 mol% Na_2O and 45 mol% of both Li_2O and Nb_2O_5
K-LN – Stoichiometric lithium niobate crystal grown from a flux containing 10 mol% K_2O and 45 mol% of both Li_2O and Nb_2O_5
Rb-LN – Stoichiometric lithium niobate crystal grown from a flux containing 10 mol% Rb_2O and 45 mol% of both Li_2O and Nb_2O_5
Cs-LN – Stoichiometric lithium niobate crystal grown from a flux containing 10 mol% Cs_2O and 45 mol% of both Li_2O and Nb_2O_5
FWHM – Full width at half maximum

A.3. Crystal growth methods

The technical application of the oxide crystals needs chemically well defined single crystals free from crystallographic defects. For growing bulk oxide crystals the Czochralski, the Bridgman, and the high temperature solution growth (HTSG) methods are widely used. The high temperature top seeded solution growth (HTTSSG) is a variant of the HTSG method.

The Czochralski and the Bridgman techniques produce good quality crystals within a relatively short time. A disadvantage is that they can be used only for the growth of congruently melting materials.

A.3.1. Bridgman technique

The method involves heating polycrystalline material in an alongated container above its melting point and slowly cooling it from one end where a seed crystal can be located. Single crystal material is progressively formed along the length of the container. The process can be carried out in a horizontal or vertical geometry.

The original technique involves a crucible filled with the material to be grown, that will be melted and lowered through a two (or more)-zone furnace. The growth of single crystal starts at the tip of the container and the solidification interface moves slowly (fig. A.1). The rates of the movement for such processes range from about 0.1 to 200 mm/h but are generally in the range 1 to 30 mm/h.

The requirement that the freezing isotherm should move systematically through the molten charge can be satisfied by moving the crucible or the furnace, or by continuously shifting the furnace temperature.

There is no need to have the whole charge molten at one time. There are advantages in having only one part of the charge molten. Such methods are referred to as zone melting (or zone refining) methods. This process is widely used for the purification of materials and may be followed by single crystal growth in the same system.

The advantage of the Bridgman method is that crystals with good dimensional tolerances can be obtained relatively quickly, it employs relatively simple technology and requires neither elaborate control system nor many man-hours supervision.

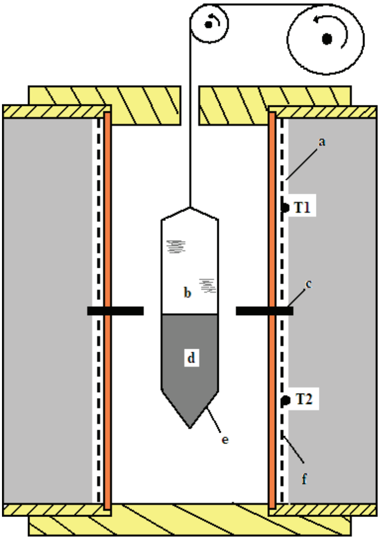

Figure A.1.: Typical Bridgman-system (T1 > T2)

a – upper winding, b - melt, c - baffle, d - crystal, e - crucible, f - lower winding

A.3.2. Czochralski technique

The basic method is simple. A typical routine is the following. The raw material is melted in a crucible. The melt is heated to a temperature few degrees above the melting point. An oriented seed crystal is brought into contact with the melt surface. After the thermal equilibrium between the melt and the seed is established (the seed is not melting and no crystallization is observed), pulling and rotation of the seed are commenced. Normally an electronic diameter control system insures the increase of the diameter of the crystal. Growth at a constant diameter is maintained until the desired length of crystal has grown. Growth is then terminated. In some cases this is done by sharply increasing the pulling rate so that the crystal breaks contact with the melt. Another procedure is to increase the furnace’s temperature so that the crystal diameter decreases fairly slowly to zero. After growth has been terminated, the system should be cooled slowly.

The apparatus used is similar to that described for the HTTSSG method in the main text (fig. 1.5). By this method, large, good quality crystals can be grown. The Czochralski growth is an important industrial method, so much the more as it can be easily automatized. It has different modifications: the liquid encapsulation Czochralski (LEC), Kyropoulos growth, the Stepanov method and the edge-defined film-fed growth. Advantages are due to the fact that the growing crystal is no longer in contact with the crucible, so it contains less strain induced dislocations and the contamination by the crucible material can be kept at a low level.

A material suitable for growth by this method should have the following properties:

(a) congruent melting,

(b) no destructive phase changes between the melting point and room temperature,

(c) low vapour pressure of each component (this condition, however, can be circumvented due to technical improvements like LEC growth of GaP),

(d) low viscosity.

A.3.3. High temperature solution growth (HTSG) methods

This is a method of crystal growth where the components of the desired substance are dissolved in an appropriate molten substance (flux) and growth takes place at the saturation temperature. A saturated solution is prepared by keeping the constituents of the desired crystal and the flux at a temperature slightly above the saturation temperature long enough to form a homogeneous solution. Then the material is cooled to the saturation temperature and the growth is started. The growth can happen by spontaneous nucleation or growth on a seed. Rates of growth from solution falls in the range 0.1 to 10 mm/day, much smaller than the rates of melt growth for the methods discussed above.

The advantages of solution growth compared to the Czochralski- and the Bridgman techniques are that its work temperature is lower than the pure material's melting point and single crystals of those substances can be grown which are impossible to obtain with other methods because:

(a) they don't melt congruently (sLN),

(b) they have destructive phase transition just below the melting point ($BaTiO_3$),

(c) the material decomposes at the melting point,

(d) the melting point is too high so there is no material available for crucible or furnace construction,

(e) we want to crystallize a low temperature phase of the material (β-BBO).

There are different versions: slow cooling method, temperature-difference method (large rare-earth ion garnet crystals), high-pressure method (diamond), solvent evaporation method (Al_2O_3, TiO_2, CeO_2, etc.), electrolytic processes (borides, oxides, sulphides, arsenides, phosphides, germanides, silicides) and liquid-phase epitaxy (semiconductors, oxidic materials).

Choosing the right solvent is very important for the HTSG technique. The main selection criteria for the solvent are: the solvent should not react with the crystal material, should not enter the lattice as a dopant, should significantly lower the crystallization temperature and the temperature dependence of solubility of the solute in the flux should be positive and significant. Table A.1 gives some examples. [J. C. Brice "Crystal growth processes", Blackie Halsted Press (1986), Glasgow]

Table A.1.: Solvents used for the growth of some materials

Material	Solvent
Al_2O_3	$PbF_2 + B_2O_3$
B	Pt
$BaFe_2O_4$	Na_2CO_3
$BaTiO_3$	Bi_2O_3
$BeAl_2O_4$	PbO, Li_2MoO_3, $PbMoO_4$
CeO_2	$NaF + B_2O_3$
Fe_2O_3	$Na_2B_4O_7$
GaAs	Ga, Sn
$GaFeO_3$	$Bi_2O_3 + B_2O_3$
GaP	Ga, Sn
Ge	In, Sn + Pb
GeO_2	$Li_2Mo_2O_7$, $Li_2W_2O_7$
$KNbO_3$	KF, KCl
$KTa_xMb_{1-x}O_3$	K_2CO_3
$MgFe_2O_4$	$Bi_2O_3 + B_2O_3$
$NiFe_2O_4$	$Na_2B_4O_7$
$PbZrO_3$	PbF_2
SiC	Si
TiO_2	$Na_2B_4O_7 + B_2O_3$
$Y_3Al_5O_{12}$	$PbO + B_2O_3$, $PbO + PbF_2$
$Y_3Fe_5O_{12}$	PbO, $PbO + PbF_2$, $BaO + B_2O_3$
ZnO	PbF_2
ZnS	ZnF_2
ZnTe	In, Ga, Sn, Bi, Pb

A.3.3.1. High temperature top seeded solution growth (HTTSSG) method

Described in chapter 1.4.1.

A.3.3.2. Pedestal Growth

The goal of this method is to grow homogeneous single crystals with non-equilibrium composition (for example: off-congruent $LiNbO_3$) by keeping the composition of the crystallizing material constant.

The starting mixed powder is sintered and pressed to a ceramic bar and the material on the top of that is melted by radiation (lamp, laser, etc.) hereby a drop appears. A seed is brought into contact with the surface of the drop where the melt is crystallized. Since only a small amount of the whole mixture is melted, the crystal is grown from the melted drop which has the same composition. There is almost no possibility for segregation because the melted part is only one drop due to the steep temperature gradient. Crystals grown by this method have small size (typically 0.1 – 2 mm in diameter and up to 10 cm long).

A.3.3.3. Micro Pulling Down method

This method involves growing single crystals through a micro nozzle by pulling in the downward direction (fig. A.2). The growth equipment consists of a micro crucible with a nozzle at the bottom, an afterheater made from Pt wire, an annealing furnace, and crystal lowering mechanism.

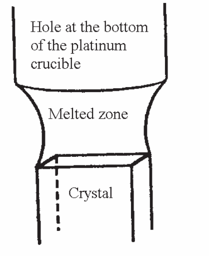

Figure A.2.: Explanation of the micro pulling down

The raw material is melted in the crucible and a droplet of the melt is allowed to pass through the micro nozzle. For oriented crystallization of a fiber crystal a seed is brought into contact with the drop and is slowly pulled down forming a fiber-like single crystal.

The amount of starting material is merely 1-10 g and due to the small volume of crystallizing droplet and the lack of segration the composition of the growing crystal may be off-equilibrium (overdoped or off-congruent), this method is ideal for exploratory crystal preparation.

By this method high quality crystals can be grown with a small size (typically 0.1 – 2 mm in diameter and 50 – 100 mm long).

A.3.4. Double crucible method

With this method single crystals with high quality and high homogeneity from congruent or off-congruent melt can be grown (by Czochralski, or HTSG method) with almost any size. The melt is divided into two parts by a double structure (two chamber system) crucible. The crystal is grown from the inner melt, and powder with the same composition as the growing crystal is continously supplied to the outer melt. The powder is supplied smoothly at the rate of weight increase of the growing crystal.

The scheme of the apparatus is presented in fig. A.3.

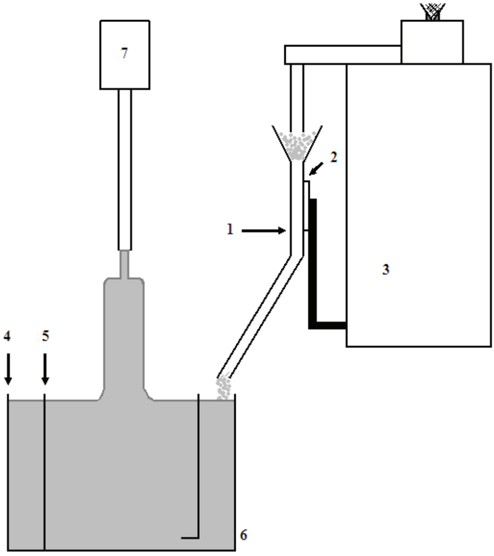

Figure A.3.: Schematic diagram of the double crucible method.
(1) – feeding tube, (2) – feeding system, (3) – automatic powder supply controller, (4) – outer wall, (5) - inner wall, (6) - double crucible, (7) – crystal weighing system

The advantage of the system is that the surface level of the melt is always constant. This suggests that the crystals can be grown in constant thermal conditions, diminishing the effect of changes in melt convection caused by the decrease in the depth of the melt during conventional pulling growth methods.

A.4. Examination and characterization methods

A.4.1. Differential scanning calorimetry

By this method the thermal behaviour of materials can be studied. It maps the heat effects of phase transformations which allows the determination of the transition temperatures and the involved enthalpy changes.

Differential scanning calorimetry (DSC) is a technique for measuring the energy necessary to establish a zero temperature difference between a substance and an inert reference material, as the two specimens are subjected to identical temperature regimes in an environment heated or cooled at a controlled rate.

Alumina, Al_2O_3 and SiC have been extensively used as reference substances for inorganic samples. Both solid samples and reference materials are usually used in powdered form. The particle size influences the results. The furnace system is usually purged with an inert gas.

Heat flux DSC

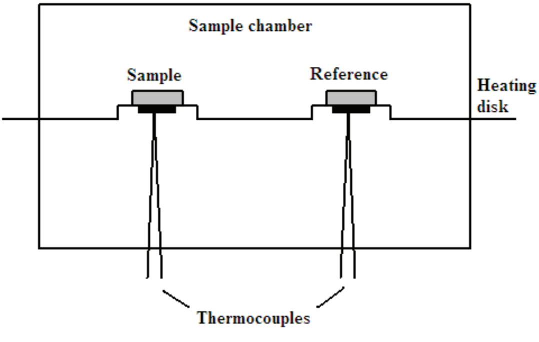

Figure A.4.: Diagram of a heat flux differential scanning calorimeter

In heat-flux DSC, the sample and the reference, in equivalent holders, usually flat pans, are placed on individual thermally conducting bases (fig. A.4). The thermocouple junctions are attached to these bases and are thus not directly in the sample or reference material. The configuration has the advantage that the output signal is less dependent upon the thermal properties of the sample, but the response is slower.

Power-compensated DSC

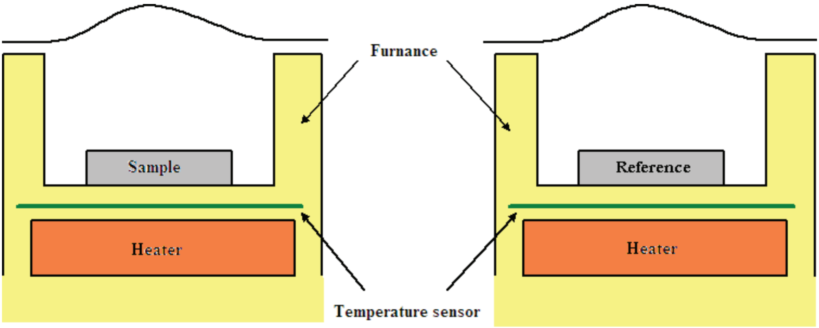

Figure A.5.: Diagram of a power compensated differential scanning calorimeter

In power-compensated DSC (fig. A.5), the sample and a reference material are maintained at the same temperature throughout the controlled temperature programme. Any energy difference in the independent supplies to the sample and the reference is recorded against the programme temperature.

DSC curves

Thermal events in the sample appear as deviations from the DSC baseline, in either an endothermic or exothermic direction, depending upon whether more or less energy has to be supplied to the sample relative to the reference material. A typical DSC curve can be seen in Fig. A.6.

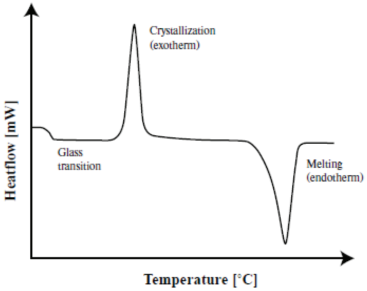

Figure A.6.: A schematic DSC curve demonstrating the appearance of several common features[*]

---

[*] www.answers.com/topic/differential-scanning-calorimetry

A.4.2. X-ray diffraction

X-rays are electromagnetic radiation of wavelength about 1 Å (10^{-10} m), which is about the same size as an atom.

X-ray diffraction has been used in two main areas, for the determination of the structure of crystalline materials and their fingerprint characterization. Each crystalline solid has its unique characteristic X-ray powder pattern which may be used as a "fingerprint" for its identification. If the material has been identified, X-ray crystallography on single crystals can be used to determine its structure, i. e. how the atoms pack together in the crystalline state and what the interatomic distances and angles are. X-ray diffraction is one of the most important characterization tools used in solid state chemistry and materials science. We can determine the size and the shape of the unit cell for any compound most easily using the diffraction of x-rays.

Bragg diffraction

As the wave enters the crystal, some portion of it will be reflected by the first layer, while the rest will continue through to the second layer, where the process continues.

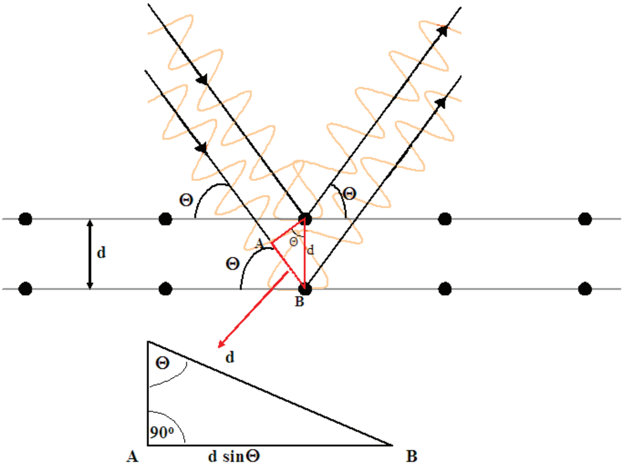

Figure A.7.: Reflection of x-rays from two planes of atoms in a solid

A single monochromatic wave is incident on aligned planes of lattice points with separation *d* at angle Θ as shown in figure A.7. The path difference between the two reflected beams is two times the *AB* distance. The interference is constructive when the phase shift is multiple to 2π, this conditions can be expressed by Bragg's law:

$$n\lambda = 2d \bullet \sin\Theta \tag{A.1}$$

where n is an integer, λ is the wavelength of x-rays, d is the spacing between the planes in the atomic lattice and Θ is the angle between the incident ray and the scattering planes.

X-ray powder diffraction

Powder diffraction is a scientific technique using X-Ray or neutron diffraction on powder or microcrystalline samples for structural characterization of materials. Ideally, every possible crystalline orientation is represented equally in the sample, leading to smooth diffraction rings around the beam axis rather than the discrete spots observed for single crystal diffraction. In accordance with Bragg's law, each ring corresponds to a particular reciprocal lattice vector in the sample crystal, with intensity proportional to the number of such planes. In practice, it is sometimes necessary to rotate the sample orientation to eliminate the effects of texturing and achieve true randomness. The dedicated machine to perform such measurements is called a powder diffractometer and the registered parameters are automatically the counts (fig. A.8).

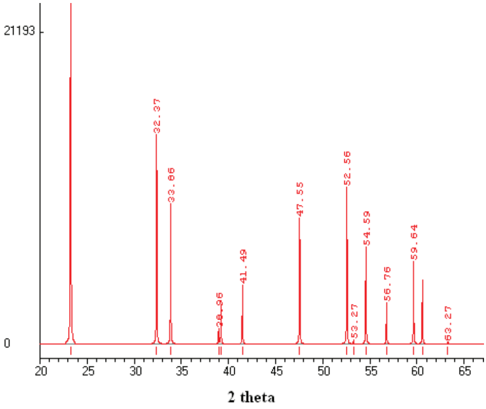

Figure A.8.: X-ray powder diffractogram of lithium niobate

A.4.3. Ultraviolet/visible and infrared spectroscopy

Lambert-Beer law

Consider a monochromatic beam of intensity I_0 with a perpendicular incidence onto a sample with parallel faces and a thickness d. Absorption takes place in the sample and the beam of radiation leaves the sample with a smaller intensity I, while a fraction of light is absorbed by the sample (Fig. A.9).

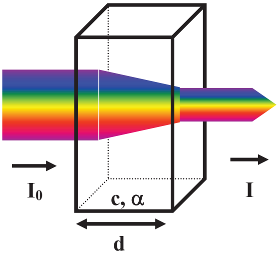

Figure A.9.: Basic phenomena underlying the Beer-Lambert law

The following definitions assume that the entire incident light is either transmitted or absorbed, while reflection or scattering is negligible. The amount of radiation absorbed may be then described by several quantities below:

Transmittance: $T = I/I_0$ (A.2)

Absorbance: $A = \log (I_0/I) = \log (1/T) = -\log T$ (A.3)

The absorbance A is proportional to the absorption path length d (sample thickness):

Absorbance (Lambert's law): $A = \alpha \cdot d$ (A.4)

where α is the linear absorption coefficient in [cm^{-1}]. The quantity α depends on the energy of radiation and is specific for a given material. By inserting equation A.4 to equation A.3, we obtain:

$$I = I_0 \cdot 10^{-\alpha d} \quad \text{(A.5)}$$

Equation A.4 can be expanded to describe also the dependence on concentration *c* of the absorbing species:

Beer's law: $\alpha = \varepsilon c$ (A.6)

Absorbance (Lambert-Beer law): $A = \varepsilon c d$ (A.7)

The proportionality constant ε is now called the molar absorption coefficient (if *c* is measured in mol; otherwise, specific absorption coefficient).

In cases when the refractive index is high (e. g. for LiNbO3 crystal $n_o = 2.38$ at $\lambda = 450$ nm) the reflection is not negligible and correction has to be used before the evaluation of the spectra. With this correction the error caused by the multiple reflected light beams can be avoided. The reflection factor (*R*) can be expressed as:

$$R = (\tilde{n} - 1)^2 / (\tilde{n} + 1)^2 \qquad \text{(A.8)}$$

where *ñ* is the complex refractive index of the material. The corrected absorption coefficient can be calculated [38]:

$$\alpha = -\frac{1}{d}\ln\left(-\frac{(1-R)^2}{2R^2T^2} + \sqrt{\left(\frac{(1-R)^2}{2R^2T^2}\right)^2 + \frac{1}{R^2}}\right) \qquad \text{(A.9)}$$

Ultraviolet-visible spectrophotometer

The basic parts of a spectrophotometer are a light source (often an incandescent bulb for the visible wavelengths, or a deuterium arc lamp in the ultraviolet), a holder for the sample, a diffraction grating or monochromator to separate the different wavelengths of light, and a detector. The detector is typically a photodiode or a CCD.

A spectrophotometer can be either single beam or double beam. In a double-beam instrument (Fig. A.10), the light is split into two beams before it reaches the sample. One beam is used as the reference; the other beam passes through the sample. Some double-beam instruments have two detectors (photodiodes), and the sample and reference beam are measured at the same time. In other instruments, the two beams pass through a beam chopper, which blocks one beam at a time. The detector alternates between measuring the sample beam and the reference beam.

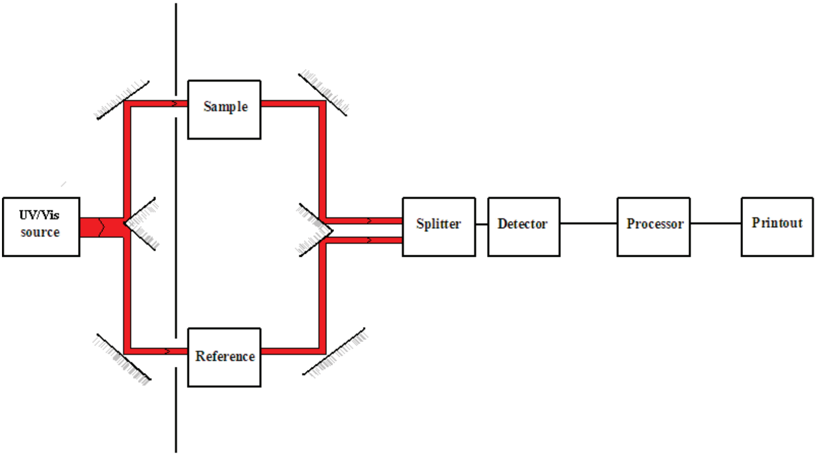

Figure A.10.: Diagram of a double-beam UV/vis spectrophotometer

Infrared spectroscopy

The infrared portion of the electromagnetic spectrum is divided into three regions; the near-, mid- and far infrared, named for their relation to the visible spectrum. The far-infrared, (approx. 400-10 cm^{-1}) lying next to the microwave region, has low energy and may be used for rotational spectroscopy. The mid infrared (approx. 4000-400 cm^{-1}) may be used to study the fundamental vibrations and associated rotational-vibrational structure, whilst the higher energy near IR (14000-4000 cm^{-1}) can excite overtone or harmonic vibrations.

In order to measure a sample, a beam of infrared light is passed through the sample, and the amount of energy absorbed at each wavelength is recorded. This may be done by scanning through the spectrum with a monochromatic beam, as in a UV/VIS spectrophotometer, or by using a Fourier transform instrument which records an interferogram, the Fourier transform of the spectrum. From this, a transmittance or absorbance spectrum may be plotted.

Our IR absorption spectra were recorded by a FTIR spectrometer.

Fourier transform infrared (FTIR) spectroscopy

This is a fast and sensitive method for measuring the absorption spectra. The method is based on a Michelson interferometer (fig. A.11).

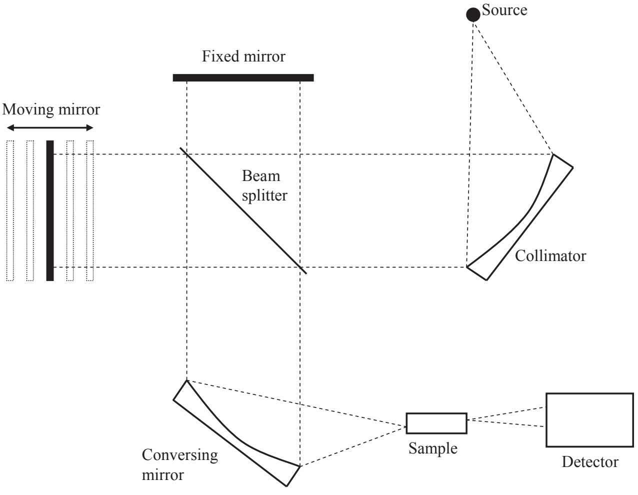

Figure A.11.: Schematic illustration for the mechanism of the Michelson interferometer

Light from a source is collimated and then divided at a beam splitter into two beams. These beams are reflected by two separate mirrors, one fixed and the other movable. Each single beam strikes the beam splitter again, where they are recombined and split again. The two components in the recombined beam interfere with each other and form a spot whose intensity depends upon the different paths traversed by the two beams before recombination.

An interferogram is the intensity at the detector as a function of the position of the moving mirror (the light path difference). From the interferogram, a single-beam spectrum can be calculated by Fourier transformation. The ratio of the single-beam spectrum with and without the sample in the light path gives the transmission spectrum. From here, absorption is determined as in UV spectroscopy.

OH^- ions in the $LiNbO_3$ crystal

OH^- ions are always present in air-grown $LiNbO_3$ crystals. The OH^- ions enter into the lattice at the growing temperature from the humidity of the environment. The OH^- ions substitute for regular O^{2-} in the lattice and the O-H bond is usually oriented to the neighbouring O^{2-} ion.

The stretching vibrational mode of the OH^- ions in $LiNbO_3$ can be measured by infrared spectroscopy at about 3420-3540 cm^{-1}. From the vibrational spectrum the amount of the OH^- ions in the crystal can be estimated of about $10^{17} – 10^{19}$ cm^{-3}.

A.4.4. Raman spectroscopy

The vibrational transitions can not only observed in the infrared, but in the Raman spectra as well. The origin of the Raman spectra is markedly different from that of IR spectra. In Raman spectroscopy, the sample is irradiated by an intense laser beam in the UV-visible region and the scattered light is usually observed in the direction perpendicular to the incident beam.

The scattered light consists of two types: one, called *Rayleigh scattering*, is strong and has the same frequency as the incident beam (ν_0) and the other, called *Raman scattering*, is very weak (10^{-5} of the incident beam) and has frequencies $\nu_0 \pm \nu_m$. The $\nu_0 - \nu_m$ and $\nu_0 + \nu_m$ lines are called the *Stokes* and *anti-Stokes* lines, respectively. Thus, in Raman spectroscopy, we measure the vibrational frequency (ν_m) as a shift from the incident beam frequency (ν_0). In contrast to IR spectra, Raman spectra can be measured in the UV-visible region where the excitation as well as Raman lines appear.

Figure A.12. illustrates Raman scattering in terms of a simple energy level structure. The line thickness is roughly proportional to the signal strength for the different transitions.

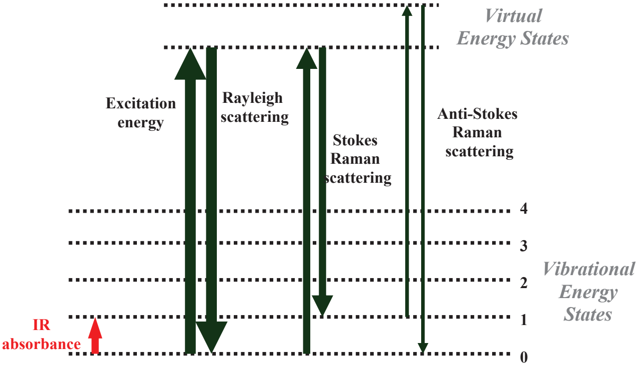

Figure A.12.: Energy level diagram for Raman scattering*

---

* www.medisciencetech.com/append/OpticalBiopsyPill.htm

Raman scattering in lithium niobate

Lithium niobate belongs to the space group $R3c$ and has point group symmetry $3m$ (see chapter 1.1). There are two formula units per unit cell and therefore 30 degrees of vibrational freedom. To a first approximation, vibrations with wave vector near zero may be characterized by group theory as 5 A_1, 5 A_2 and 10 E phonon branches. Of these, one A_1 and one E are the acoustic branches, the five A_2 fundamentals are Raman inactive, and the remaining 4 A_1 and 9 E optical branches are Raman active.

The difference in Raman scattered intensity between transverse (TO) and longitudinal (LO) optic-phonon modes in piezoelectric crystals can be ascribed to an electro-optic effect arising from the electric field associated with the LO phonon.

In this thesis a spectrum was described by four symbols, for example: *z(xy)z* (where *x*, *y* and *z* are the standard set of orthogonal principal axes for trigonal symmetry, see chapter 1.1). The symbols denote, from left to right, the direction of the incident radiation, its polarization, the polarization of the detected Raman (back)scattered radiation, and the direction of its observation, respectively. Vibrations of different symmetry can be detected in different polarization settings.

Table A.2 shows the appearing Raman modes in different polarizations in $LiNbO_3$.

Table A.2.: Raman modes of $LiNbO_3$ for different configurations detected in backscattered geometry (the a(bc)a and a(cb)a configurations are equivalents because of the symmetry of the Raman tensors)

Configuration	Modes in the spectrum
x(yy)x	A_1(TO) + E(TO)
x(yz)x	E(TO)
x(zz)x	A_1(TO)
y(xx)y	A_1(TO) + E(LO)
y(xz)y	E(TO)
y(zz)y	A_1(TO)
z(xx)z	A_1(LO) + E(TO)
z(xy)z	E(TO)
z(yy)z	A_1(LO) +E (TO)

A.5. Residual X-ray diffractograms for chapter 3.1.2.

A.5.1. Samples with 10 mol% Cs_2O content

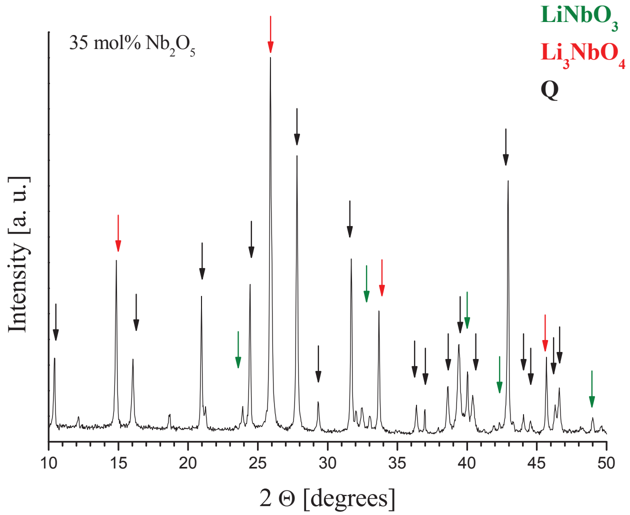

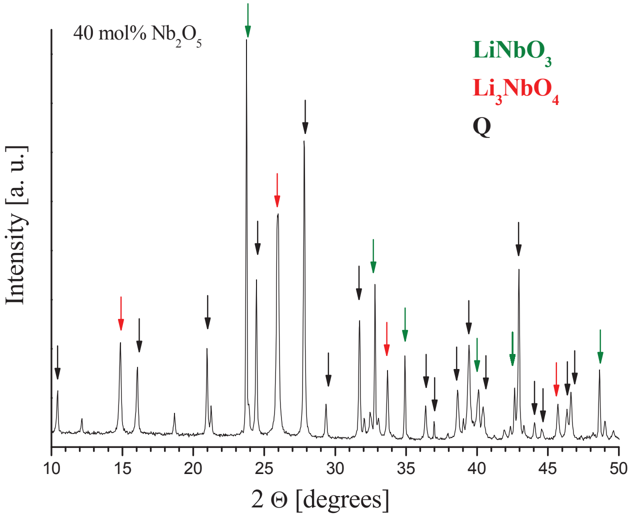

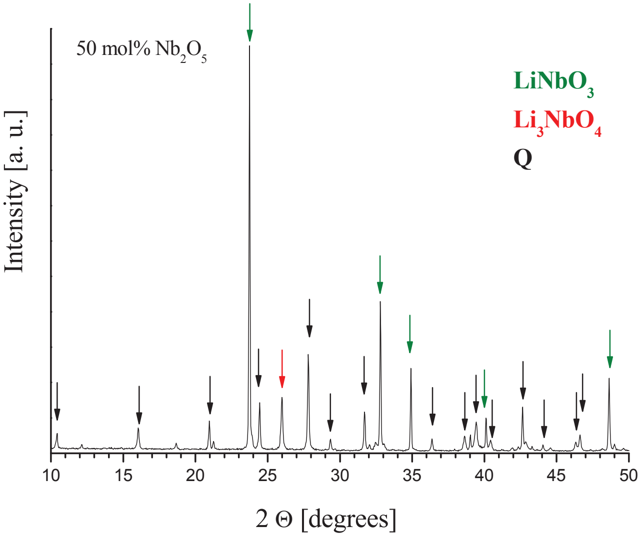
50 mol% Nb_2O_5
$LiNbO_3$
Li_3NbO_4
Q
Intensity [a. u.]
10
15
20
25
30
35
40
45
50
2 Θ [degrees]

A.5.2. Samples with 20 mol% Cs_2O content

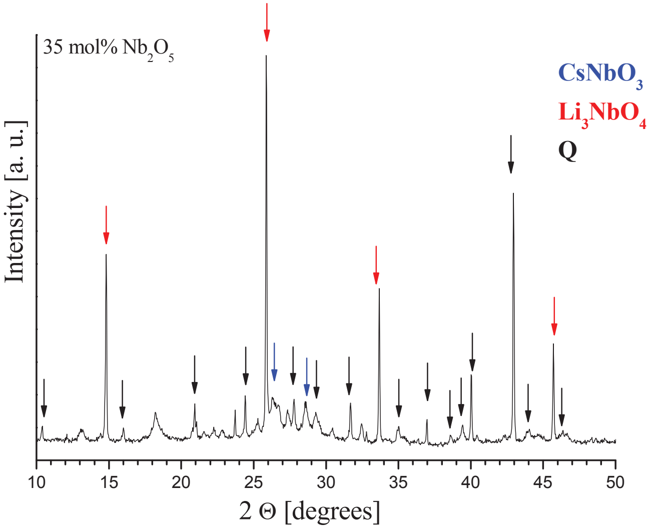

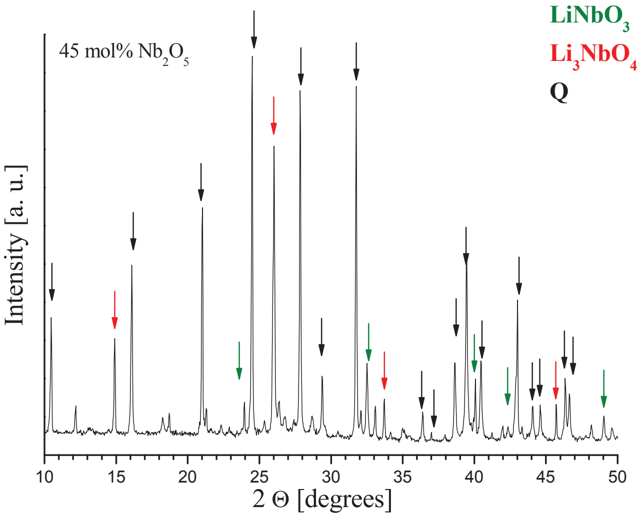

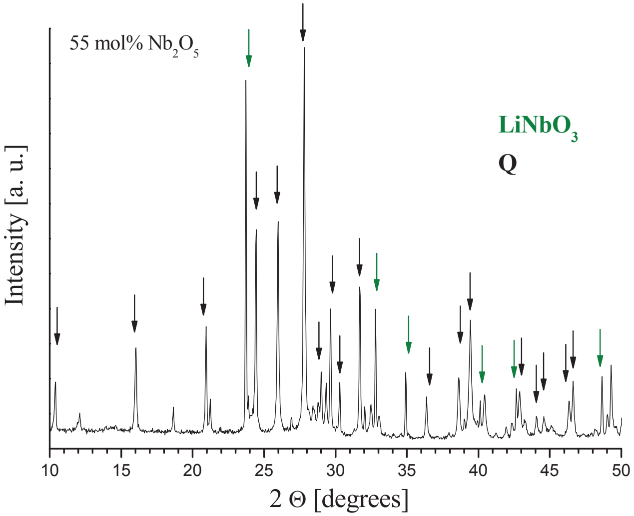
55 mol% Nb_2O_5
$LiNbO_3$
Q
Intensity [a. u.]
10
15
20
25
30
35
40
45
50
2 Θ [degrees]

A.5.3. Samples with Li / Nb = 1 ratio

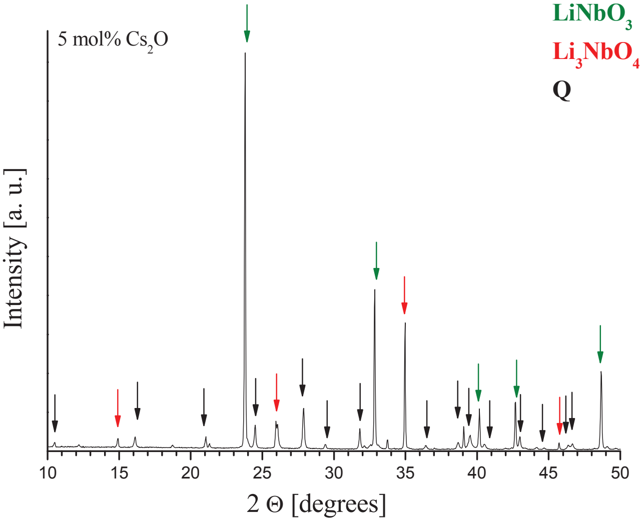

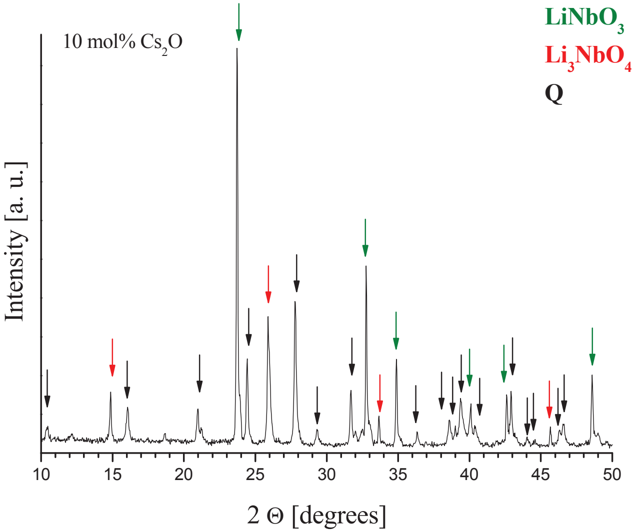

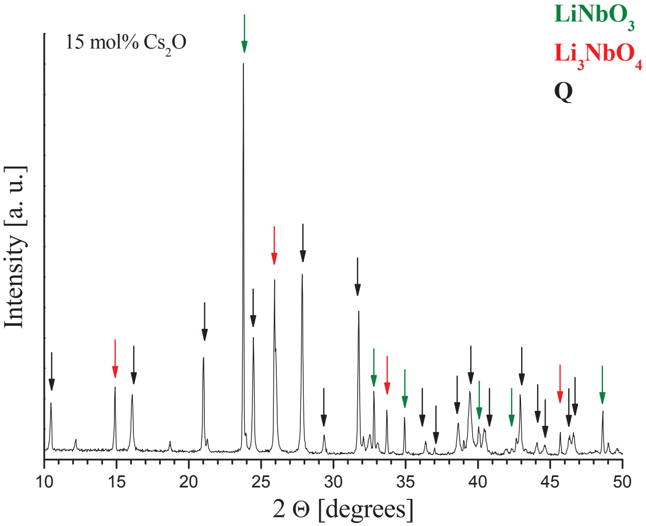
15 mol% Cs_2O
$LiNbO_3$
Li_3NbO_4
Q
Intensity [a. u.]
2 Θ [degrees]
10
15
20
25
30
35
40
45
50

A.5.4. Sample with 30 mol% Cs_2O, 50 mol% Nb_2O_5 and 20 mol% Li_2O content

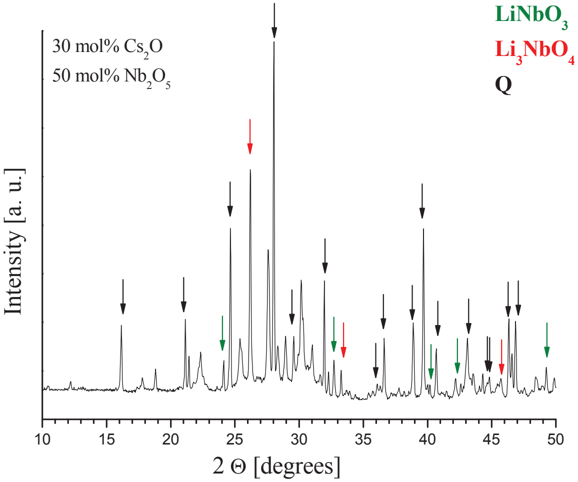

Summary in English and in Hungarian

The versatility of $LiNbO_3$ arises from the unique combination of piezoelectric, pyroelectric, electro-optical and nonlinear optical properties enabling it to be used in a wide range of applications. It is commonly grown from the congruent composition where the liquidus and solidus phases are in equilibrium. For $LiNbO_3$ the congruent composition differs from the stoichiometric ([Li] / [Nb] = 0.945). Using this starting composition in crystal growth, the segregation coefficients for both Li_2O and Nb_2O_5 are equal to 1, single crystals of good quality and uniform composition can be grown (congruent lithium niobate (cLN)). Most requirements of low-power applications can be satisfied by the cLN crystal despite of its high Li-deficiency and the large concentration of intrinsic defects. On the other hand these defects seriously limit high-power applications in electro-optics and non-linear optics. Investigations of the K_2O - Li_2O - Nb_2O_5 ternary system near the existence region of lithium niobate proved that the use of K_2O as a solvent component permits the growth of stoichiometric $LiNbO_3$ with much less intrinsic defects resulting in numerous new possibilities for applications. The presented work extended these investigations by examining the suitability of other alkali oxides (Na_2O, Rb_2O and Cs_2O) instead of K_2O.

Phase relations in the X_2O - Li_2O - Nb_2O_5 (X = Na, Rb or Cs) ternary systems were investigated, corresponding phase diagrams were constructed, new phases were identified, growth experiments were carried out and the crystals were characterized by spectroscopic methods. It was established that crystals with $[Li_2O] / [Nb_2O_5] = 1$ can be grown from all examined ternary systems containing $[X_2O] = 10 - 16$ mol%. A new method was developed for an easy and accurate determination of the Li_2O content of undoped $LiNbO_3$ crystals based on the measurement of the intensity ratio of the two hydroxyl ion vibrational peaks (at 3465 and 3480 cm^{-1}) in the infrared absorption spectra. It was confirmed that the FWHM of the E(TO1) Raman mode changes with the Li_2O content of the $LiNbO_3$ crystal but without correction these measurements cannot be used, as assumed earlier, for a universal composition determination of $LiNbO_3$. Sodium – contrasted with rubidium and cesium – was shown to be incorporated into the $LiNbO_3$ lattice, occupying Li sites.

In the present Ph.D. work it was established that, in addition to K_2O, the use of Rb_2O or Cs_2O as a solvent component also yields stoichiometric $LiNbO_3$ single crystals which satisfy the application requirements.

A $LiNbO_3$ egykristályt – piezoelektromos, piroelektromos, elektro-optikai, valamint nemlineáris optikai tulajdonságainak egyedülállóan jó kombinációjából eredően – széles körben alkalmazzák a technikában. Leggyakrabban kongruens összetételű olvadékból növesztik, melynél az egymással egyensúlyban lévő olvadék és szilárd fázis összetétele azonos. $LiNbO_3$ esetén a kongruens összetétel eltér a sztöchiometrikustól, ([Li] / [Nb] = 0,945). Ebből az arányból kiindulva a komponensek (Li_2O, Nb_2O_5) megoszlási hányadosa a szilárd és folyadék fázis között 1, így jó minőségű, állandó összetételű egykristály (kongruens lítium-niobát (cLN)) növeszthető. A Li hiányos szerkezetű (saját anyagú, intrinszik hibahelyeket tartalmazó) cLN kristály tulajdonságai az alkalmazási követelmények nagy részét kielégítik. A saját anyagú hibahelyek igen magas koncentrációja azonban jelentős mértékben korlátozza elektrooptikai és nemlineáris optikai alkalmazhatóságát. A K_2O - Li_2O - Nb_2O_5 hármas rendszer fázisviszonyainak vizsgálata bizonyította, hogy a K_2O oldószerkomponensként való alkalmazása lehetővé teszi sztöchiometrikus lítium-niobát kristály növesztését, mely nagyságrendekkel kevesebb intrinszik hibát tartalmaz, és számtalan új alkalmazási lehetőséget eredményez. A bemutatásra kerülő dolgozat témája ezen kutatások kiterjesztése a K_2O-on kívül egyéb alkáli oxidok (Na_2O, Rb_2O és Cs_2O) alkalmasságának vizsgálatára.

Tanulmányoztam az X_2O - Li_2O - Nb_2O_5 (X = Na, Rb, vagy Cs) hármas rendszerek fázisviszonyait, megfelelő fázisdiagramokat szerkesztettem, új fázisokat azonosítottam, kristálynövesztési kísérleteket végeztem, a növesztett kristályokat spektroszkópiai módszerekkel minősítettem. Bebizonyítottam, hogy mindhárom vizsgált hármas rendszer esetén a $[Li_2O] / [Nb_2O_5] = 1$ és $[X_2O] = 10 – 16$ mol% összetétel tartományból kiindulva növeszthető $LiNbO_3$ egykristály. Kvantitatívvá tettem az adalékolatlan $LiNbO_3$ Li_2O tartalmának infravörös spektroszkópiai mérésen alapuló egyszerű és pontos meghatározását a hidroxidion rezgési spektrumában megjelenő két csúcs (3465 és 3480 cm^{-1}) intenzitásarány változásának követésével. Az E(TO1) Raman módus félérték-szélessége a $LiNbO_3$ kristály Li_2O tartalmával monoton változik. Igazoltam, hogy – a korábbi feltevésekkel ellentétben – ezek a mérések összetétel meghatározásra kizárólag egy korrekciós faktor figyelembe vételével használhatók. Kimutattam, hogy a nátrium, szemben a rubidiummal és céziummal, beépül a $LiNbO_3$ rácsba, ahol Li helyeket foglal el. Doktori munkám során bizonyítottam, hogy a vizsgált alkáli oxidok közül a Cs_2O és Rb_2O oldószerkomponensek lehetővé teszik az alkalmazás kívánalmainak megfelelő sztöchiometrikus $LiNbO_3$ egykristály növesztését.